2018

Understanding Confined Fluids in Shale Gas Systems

Edward Alan Thomas
University of Rhode Island, edward_thomas@uri.edu

UNDERSTANDING CONFINED FLUIDS IN SHALE GAS SYSTEMS

BY

EDWARD ALAN THOMAS

A DISSERTATION SUBMITTED IN PARTIAL FULFILLMENT OF THE REQUIREMENTS FOR THE DEGREE OF

DOCTOR OF PHILOSOPHY

IN

CHEMICAL ENGINEERING

UNIVERSITY OF RHODE ISLAND

2018

DOCTOR OF PHILOSOPHY DISSERTATION

OF

EDWARD THOMAS

APPROVED:

Dissertation Committee:

Major Professor Angelo Lucia

Michael Greenfield

Joan Peckham

Nasser H. Zawia
DEAN OF THE GRADUATE SCHOOL

UNIVERSITY OF RHODE ISLAND

2018

ABSTRACT

Given the complexity of shale gas at high pressures, researchers aim to characterize the thermodynamic properties of confined fluids using a mixture of experimental, modeling, and simulation techniques. In this work we frequently use the predictive capabilities of simulation to couple the property results to models. The overall results are then compared to experimental data for verification purposes.

We employ a Monte Carlo simulation technique to ensure that a simple linear mixing rule for internal energies of departure holds thereby allowing pure component data to extend to mixtures. The results are coupled to the Gibbs-Helmholtz Constrained equation of state allowing for bulk-scale bubble point reduction predictions. In addition, the sensitivity of the results is determined.

Adsorption of n-alkanes at high pressure conditions are studied as a function of carbon chain length, temperature, and pore throat size (14.2 Å to 19.88 Å) to give an overall picture of shale gas behavior at reservoir conditions. A simple model is shown to provide a reasonable estimate of the isotherms at high pressures up to 500 bar and a temperature range of 300 K to 550 K. Under the assumption of ideal site-site interactions, mixtures are predicted for methane/ethane and methane/ethane/propane systems and compared to work in the literature.

An important aspect of this work is the verification to experimental data; we expand on recent work by characterizing the experimental to simulation data in a robust manner. Quantitative agreement is achieved when estimating the surface area and void volume of the porous material.

ACKNOWLEDGMENTS

I would like to express my sincere gratitude to my advisor Dr. Angelo Lucia for his support throughout the years. Throughout my time working with Dr. Lucia as an Undergraduate and Graduate student, I can firmly state that he has provided me many opportunities to grow personally and professionally. I look forward to applying the skills I have learned from him to future endeavors.

I am also indebted to Dr. Michael Greenfield and Dr. Joan Peckham for all their help and guidance during the committee meetings. They were instrumental in helping me prepare a concise and clear presentation of research related work. Heath Henley who started working with me in the laboratory back in 2010 has been a tremendous help and friend.

My family and friends have always supported me during my time as a graduate student. I will always remember when they supported me regardless of the outcome of life decisions and events.

I would also like to extend a thank you to faculty of Enrollment Services, I am grateful for the opportunities provided.

PREFACE

This thesis is prepared in a manuscript format and is organized by chapters that contain accepted, submitted, or prepared publications.

Chapter 1 presents a brief overview of the literature in context of confined fluids as well as motivation for this work.

Chapter 2 is published within a special issue in the journal *Computers & Chemical Engineering*. This work describes fluid properties of five binary mixtures relevant to shale gas and light tight oil applications. A linear mixing rule is employed to relate pure fluid information to describe the fluid properties of mixtures. In addition, the sensitivity of the energy parameter for the Gibbs-Helmholtz constrained equation of state is described. Overall, the results show that this approach can provide meaningful estimates of reductions in bubble point pressure for light tight oils.

Chapter 3 has been submitted to the Journal of Petroleum Science and Engineering. This article represents an extension of the work prepared in chapter 2. In this paper, the adsorption isotherms of shale and light oil related n-alkanes are presented. The results show that there is an impact of pore throat upon the adsorption isotherms and internal energies of departure. Fitting parameters are applied to the data using a Langmuir adsorption model, which allows the thermodynamics community to easily reproduce the adsorption isotherms for their applications. Finally, an Ideal Adsorbed Solution Theory calculation is provided for a ternary mixture which gives a general description of the gas uptake in the Marcellus and Barnett wells.

Chapter 4 is prepared for submission to the Journal of Petroleum Science and Engineering. Absolute adsorption simulation data is compared to experimental excess

and net adsorption data for various adsorption processes. A conversion technique that uses the Gibbs dividing surface derivation to define the upper and lower limits of adsorption phenomena is used. Results of shale gas adsorption over-prediction are normalized using both excess and net adsorption data. A new direct conversion approach in the Canonical ensemble is proposed by considering the virial pressure of the bulk fluids in equilibrium with the adsorbants inside the nanochannel slit pore at high pressures. Finally, the conversion adsorption results are compared to existing methods and experimental data with exceptional agreement when compared to traditional methods.

Chapter 5 summarizes the conclusions of this work in context to its contributions to the thermodynamic community.

TABLE OF CONTENTS

ABSTRACT ii

ACKNOWLEDGMENTS iii

PREFACE iv

TABLE OF CONTENTS vi

LIST OF TABLES ix

LIST OF FIGURES xi

1 INTRODUCTION 1

1.1 Justification and Significance of the Problem 2

1.2 Brief Adsorption Literature Background 3

1.3 Advancement of Knowledge 7

1.4 References 10

2 EQUATION OF STATE COMPUTATIONS FOR CONFINED FLUIDS 12

2.1 Abstract 13

2.2 Introduction 14

2.3 Literature Survey 16

2.4 Computational Procedure for Internal Energies of Departure 17

2.4.1 The Unconfined NPT Ensemble. 17

2.4.2 The Confined Canonical Ensemble. 20

2.5 Main Computational Results 24

2.6 Sensitivity Analysis 27

2.6.1 Energy Parameter and Molar Density 27

2.6.2 Bubble Point 31

2.7 Conclusions 34

2.8 References 36

2.9 Nomenclature 38

3 UNDERSTANDING PORE-LEVEL PHENOMENA OF N-ALKANES AT HIGH PRESSURES 39
3.1 Abstract 40
3.2 Introduction 40
3.3 Literature Survey 41
3.3.1 Adsorption Models: 42
3.3.2 Equation of states (EOS): 42
3.4 Computational Methodology 45
3.4.1 Benchmark Simulations 48
3.4.2 Langmuir Equation & Ideal Adsorbed Solution Theory 50
3.5 Simulation Results 51
3.5.1 Adsorption of n-Alkanes in Graphite Nano-channel System 51
3.6 The Impact of Confinement 58
3.6.1 Impact of Confinement on U^D 58
3.7 Pore Throat Effects 61
3.8 Conclusion 67
3.9 Acknowledgement 68
3.10 References 68
3.11 Nomenclature 71
4 CONNECTING CANONICAL SHALE GAS SIMULATIONS TO EXPERIMENTAL DATA AT HIGH PRESSURES 73
4.1 Abstract 74
4.2 Introduction 75
4.3 Literature Survey 77
4.3.1 Excess Adsorption: 79
4.3.2 Net Adsorption: 81
4.3.3 Surface Area Comparison: 82
4.4 Overview of proposed work 83
4.4.1 Computational Procedure 83

4.4.2 Adsorption Monte Carlo Simulations 85
4.4.3 Isothermal-Isobaric Ensemble (NPT) 87
4.4.4 Density Computations 88
4.4.5 Free Volume and Surface Area Computations 89
4.5 Results and Discussion 90
4.5.1 Accurate bulk fluid methane densities in the shale gas high pressure regime 91
4.5.2 Comparison of excess and net adsorption to experimental data using conventional approach with NPT computed densities 94
4.5.3 Surface area approach for linking excess and net adsorption curves 96
4.5.4 Impact of pore free volume between methane and helium molecules . 101
4.6 Conclusion 103
4.7 Acknowledgement 106
4.8 References 106
4.9 Nomenclature 108
5 CONCLUSION 111
6 APPENDICES 113
6.1 Appendix for Equation of State Computations for Confined Fluids 113
6.1.1 Pure Component Internal Energy of Departure for Confinement 113
6.1.2 Pure Component Unconfined Internal Energy of Departure with and without Analytical Tail Cutoff Corrections 114
6.1.3 Pure component fluid properties 115
6.1.4 Comparison of U^{D}_{M} Using Linear Mixing Rule for Confined Mixtures without Analytical Tail Cutoff Corrections 115
6.1.5 Comparison of U^{D}_{M} Using Linear Mixing Rule with Direct Monte Carlo Simulation for Unconfined Mixtures without Analytical Tail Cutoff Corrections[a,b] 118
6.1.6 Comparison of U^{D}_{M} Using Linear Mixing Rule with Direct Monte Carlo Simulation for Unconfined Mixtures with Analytical Tail Cutoff Corrections .. 120
6.2 Langmuir Parameters for Various Hydrocarbons 122

LIST OF TABLES

Table 2.1: Comparison of Unconfined NPT U^{D}_{i} Using Towhee and RASPA..... 18

Table 2.2: Comparison of Methane/Octane NPT U^{D}_{M} Using Towhee and RASPA ... 18

Table 2.3: Comparison of Water/Hexane NPT U^{D}_{M} Using Towhee and RASPA..... 19

Table 2.4: Comparisons of U^{D}_{M} the Linear Mixing Rule with Direct Simulation..... 25

Table 2.5: Confined U^{D}_{M} for Methane/Octane at 300 K and 200 bar..... 26

Table 2.6: Unconfined U^{D}_{M} for Methane/Octane at 300 K and 200 bar..... 26

Table 2.7: GHC-Predicted Bubble Point Reduction for Confined CH_4/C_8H_{18} at 300K 33

Table 2.8: GHC-Predicted Bubble Point Reduction for Confined 50 mol % CH_4/50 mol% C_8H_{18} at 300K..... 34

Table 3.1: Nanochannel Framework Specifications 47

Table 3.2: Comparison of GCMC and NVT results for n-Hexane in a 14.2 Å graphite framework 49

Table 3.3: Composition of Marcellus and Barnett Shale Wells..... 63

Table 4.1: Framework Specifications 85

Table 4.2: Forcefield Parameters 86

Table 4.3: Volume of pore space occupied by molecules..... 102

Table 6.1: Force field, NVT Ensemble Average, and Reference Internal Energy..... 113

Table 6.2: Species, Force field, NPT Ensemble Average, and Reference Internal Energy 114

Table 6.3 Pure Component Fluid Properties..... 115

Table 6.4: Comparison for Confined Mixtures of Methane/Octane 115

Table 6.5: Comparison for Confined Mixtures of Water/Hexane..... 116

Table 6.6: Comparison for Confined Mixtures of Methane/Propane 116

Table 6.7: Comparison for Confined Mixtures of CO_2/Hexane 117

Table 6.8: Comparison for Confined Mixtures of CO_2/Propane 117

Table 6.9: Comparison for Unconfined Mixtures of Methane/Octane 118

Table 6.10: Comparison for Unconfined Mixtures of Water/Hexane..... 118

Table 6.11: Comparison for Unconfined Mixtures of Methane/Propane 119

Table 6.12: Comparison for Unconfined Mixtures of CO_2/Hexane 119

Table 6.13: Comparison for Unconfined Mixtures of CO_2/Propane..... 119

Table 6.14: Comparison for Unconfined Mixtures of Methane/Octane 120

Table 6.15: Comparison for Unconfined Mixtures of Water/Hexane..... 120

Table 6.16: Comparison for Unconfined Mixtures of Methane/Propane 121

Table 6.17: Comparison for Unconfined Mixtures of CO_2/Hexane 121

Table 6.18: Comparison for Unconfined Mixtures of CO_2/Propane..... 121

Table 6.19: Methane Langmuir Parameters..... 122

Table 6.20: Ethane Langmuir Parameters..... 123

Table 6.21: Propane Langmuir Parameters..... 124

Table 6.22: Butane Langmuir Parameters..... 125

Table 6.23: Octane Langmuir Parameters..... 126

Table 6.24: Hexadecane Langmuir Parameters 127

LIST OF FIGURES

Figure 1.1: Example of methane and carbon dioxide adsorption data from Heller & Zoback (adsorbed methane (circles) and carbon dioxide (triangles)) [1] 4

Figure 2.1: Flowchart for Computing Mixture U^{D}_{M} 22

Figure 2.2: Snapshot of NVT Mixture of Water/Hexane (75/25) at 290 K 23

Figure 2.3: Sensitivity of a_M to 5% Uncertainty in Confined U^{D}_{M} 28

Figure 2.4: Sensitivity of V_M to 5% Uncertainty in Confined U^{D}_{M} 29

Figure 2.5: Comparison of a_M to 5% Uncertainty in Confined and Unconfined U^{D}_{M} . 29

Figure 2.6: Comparison of V_M to 5% Uncertainty in Confined and Unconfined 30

Figure 3.1: Framework and example snapshot of confined hexadecane NVT simulations 46

Figure 3.2: Flowchart for Computational Procedure 48

Figure 3.3: Adsorption Isotherms of Methane 52

Figure 3.4: Internal Energies of Departure for Methane 52

Figure 3.5: Adsorption Isotherms of Ethane 53

Figure 3.6: Internal Energies of Departure for Ethane 53

Figure 3.7: Adsorption Isotherms of Propane 54

Figure 3.8: Internal Energies of Departure for Propane 54

Figure 3.9: Adsorption Isotherms of Butane 55

Figure 3.10: Internal Energies of Departure for Butane 55

Figure 3.11: Adsorption Isotherms of Octane 56

Figure 3.12: Internal Energies of Departure for Octane 56

Figure 3.13: Adsorption Isotherms of Hexadecane 57

Figure 3.14: Internal Energies of Departure for Hexadecane 57
Figure 3.15: Adsorption Isotherms for increasing n-alkane chain length at 14.2 Å and 450 K 59
Figure 3.16: Normalized End-to-End Distance Histogram for Propane, Butane, and Octane at 300 K & 14.2 Å 60
Figure 3.17: U^D of increasing n-alkanes chain length at 14.2 Å and 450 K 61
Figure 3.18: Comparison of simulated methane adsorption with the experimental data in Heller and Zoback [9] 62
Figure 3.19: IAST results of methane/ethane mixture (A. this work, B. Sharma et al. 2015) 65
Figure 3.20: IAST Uptake for Methane at 313K & 200 bar for 14.2 Å Sheet-Sheet Distance 66
Figure 3.21: IAST Uptake for Ethane at 313K & 200 bar for 14.2 Å Sheet-Sheet Distance 66
Figure 3.22: IAST Uptake for Propane at 313K & 200 bar for 14.2 Å Sheet-Sheet Distance 67
Figure 4.1: Flowchart for Computational Procedure 84
Figure 4.2: Example snapshot of methane in equilibrium with graphite slit pore (2.7 bar, 303.15 K) 87
Figure 4.3: Comparison of indirect methods for methane bulk densities to reported data [17] 91
Figure 4.4: Comparison of direct method for methane bulk densities to NIST 92

Figure 4.5: Excess and Net adsorption isotherms compared to experimental data [15] 95
Figure 4.6: Comparison of excess adsorption isotherms to experimental data with NPT and PR EOS computed methane densities [15]..... 98
Figure 4.7: Comparison of net adsorption isotherms to experimental data with NPT and PR EOS computed methane densities [15]..... 98
Figure 4.8: Direct computation of excess adsorption using virial pressure on methane molecules located outside the slit pore [15]..... 100
Figure 4.9: Direct computation of net adsorption using virial pressure on methane molecules located outside the slit pore [15]..... 101
Figure 4.10: Effect of computed accessible methane and helium volume on NVT adsorption..... 103

1 INTRODUCTION

Shale gas and light tight oils will play an important role in the United States and Global unconventional energy resource portfolios in the future due to their great potential as an abundant energy resource. Shale gases are contained within solids that are a type of porous media with pore spaces in the nanoscale range (i.e., < 50 nanometers) and low permeabilities < 0.1 milliDarcies. Due to the nature and scale of nanoporous materials, obtaining adsorption data at reservoir conditions is challenging and dependent on core samples [1]. In turn, this has spurred a great effort from the simulation and modeling communities to build understanding of shale gas adsorption at high-pressures [1]. The effort contained in this thesis consists of using numerical simulation to understand confinement and characterize shale gas in the high-pressure regime. However, both experimental and simulation results have been stymied by the widely varying physical characteristics of shale reservoirs (e.g. rock, pore throat, chemical composition, size, shape). On the contrary, the majority of current models reported in the literature have been regressed to a limited amount of high pressure data, are correlative, and thus do not have predictive capabilities. One of the objectives of the work in this thesis aims to simulate shale gas adsorption at high pressures and upscale the results to the bulk fluid length scale using the Gibbs-Helmholtz constrained (GHC) equation of state, providing a predictive tool which uses internal energies or adsorption data for modeling adsorption of n-alkanes at high pressures. Finally, it is the author's hope that this research will be used in future studies by the research community as a whole as part of a larger effort to provide forecasting tools

(e.g. equation of state, reservoir simulation, etc.) for the understanding of shale gas and light tight oil production.

1.1 Justification and Significance of the Problem

It is important to reiterate the scope of the role that shale gas will play in the future. In 2008, the World Energy Council estimated that the total world resources of shale oil was 689 gigatons, which could yield 4.8 trillion barrels of oil, with the United States providing around 3.7 trillion barrels [2]. In 2013 the United States Energy Information Administration (EIA) projected that the total unproven technically recoverable shale gas reserves across the globe [3] will play a major role in the world energy portfolio. Some major producers include the U.S. (622.5 trillion ft^3), Canada (572.9 trillion ft^3), Mexico (545.2 trillion ft^3), Australia (429.3 trillion ft^3), Argentina (801.5 trillion ft^3), and Russia (284.5 trillion ft^3). Finally, a staggering 1115.2 trillion ft^3 of shale gas reserves is estimated to exist in China. Though the U.S. Energy Information Administration (EIA) predicts a minor downturn through 2017, once oil prices recover by 2019, shale and light tight oil projections are expected to increase to 1.3 million barrels per day [4]. In this case, Shale gas could play a major role as forecasts predict an increase of 70 billion cubic feet per day from 2015 to 2040. It is important to note that projections from the EIA are just that, projections, and are not definitive statements about what will occur in shale gas markets. Since markets are unpredictable, in the event of a continued oil price downturn throughout 2040, shale gas production will still remain relevant with an annual production of 40 billion cubic feet per day [4]. Depending on the amount extracted, this could lead to 20 - 40 years

of global energy, which could be used to offset the depleting conventional oil resources. Technological increases are leading to a reduction in drilling costs and an increased drilling efficiency in major reservoirs such as the Bakken, Marcellus, and Eagle Ford formations. For example, in China great progress has been achieved with the first commercial horizontal well to recover $16.7x10^4$ m^3/day after 15 stages of fracturing [5]. As a result, shale gas has the potential to remain a top energy resource for the near future as conventional supplies diminish. However, this success has been stymied by the complex nature of adsorbed shale gas not limited to size, shape, surface, chemical characteristics of individual pores. Finally, shale gas production could be limited by regulatory policies that limit of CO_2 emissions.

1.2 Brief Adsorption Literature Background

In order to develop a theoretical model for the amount of gas adsorbed into the shale (adsorption) we must first look at available experimental investigations and theoretical models currently available in the literature (see Fig. 1.1).

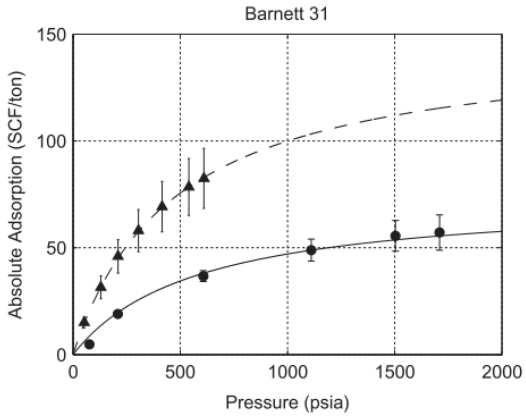

Figure 1.1: Example of methane and carbon dioxide adsorption data from Heller & Zoback (adsorbed methane (circles) and carbon dioxide (triangles)) [1]

Starting with recent experimental findings in Fig 1.1 we observe results from the lower Silurian marine shale of the Longmaxi Formation (Upper Yangtze Platform, China) for methane adsorption up to 109.4 bar [6]. In addition, adsorption profiles for methane and carbon dioxide were experimentally determined for the Barnett 31, Marcellus, Eagle Ford 127, and Montney formations up to approximately 117.2 bar [1]. Additional data can be found for methane, nitrogen, and carbon dioxide for Woodford shale from the Payne, Hancok, and Caney county formations up to 125 bar [7]. At higher pressures than experimentally available, the results have been difficult to obtain due to the complexity of the interactions (pore throat size, chemical composition, fluid-fluid interactions, etc.) of adsorbed gases inside shale rock [8]. To circumvent this, models have been developed to account for these interactions at high pressures. These models are not limited by varying pore throat sizes and shape distribution in the nanometer regime, chemical composition, surface area profile, etc. but they typically rely on empirical methods for adsorption modeling.

Since the adsorption literature is vast, we only highlight methods relevant to this thesis.

1) Traditional Adsorption Models

Traditional adsorption models are used to describe shale gas in the low-pressure regime by fitting the model to available data (less than 1 bar). The following well-known Langmuir equation

$$n_i = M \frac{KP}{1+KP} \quad 1.1$$

can be fit to adsorption data where n_i is the pure component adsorbate isotherm, M represents a unique adsorption site, P is the pressure of the adsorbed molecule, and K is a parameter with units of inverse pressure. Recent work has reviewed traditional models such as the Henry, Freundlich, Langmuir, Dubinin-Radushkevich, Radke-Prausnitz, Toth, Langmuir-Freundlich models applied to shale gas adsorption for methane and carbon dioxide up to 140 bar [9]. While these models provide excellent agreement with experimental data in the low-pressure regime, the authors note that they typically do not predict high-pressure adsorption due to large interactive forces between shale gas molecules, pore-filling geometry, and complex gas-rock interactions. In addition, they are not suited for extrapolation at high pressures if they are not properly fitted or no data is present. These models can be extended to describe mixtures with ideal adsorption solution theory (IAST) [10]. As with all models, there are assumptions and limitations, the adsorbed molecule in IAST is assumed to be well mixed and each molecule has access to the same surface area.

2) Equation of states (EOS)

There are numerous equations of state developed for the description of adsorption phenomena applied to shale gas reservoirs. These equations describe the pressure, temperature, volume, and compositions relationship of fluid mixtures and can be applied at high pressures. For example, a modified Peng Robinson equation was used to describe meso-porous materials MCM-41 and 13X for methane and carbon dioxide up to 1.2 bar by using a 16-constant expression fitted to simulated bulk fluid densities in thermodynamic equilibrium with confined media [11].

Again, most of these equations are regressed to experimental data in order to describe low-pressure adsorption (less than 100 bar). Myers [12] used a rigorous approach involving desorption functions and provides an example for ethylene adsorbed on NaX zeolite up to 1.4 bar. Earlier, more empirical work by Myers was based on the use of solution theory by treating the adsorbent as the solvent and small molecules at low concentrations as the solute [13] for adsorption pressures up to 1000 bar. The Elliott-Suresh-Donohue (ESD) equation has been applied to gas adsorption on activated carbon for a number of components including acetylene, propylene, and ethylene for pressures up to 2 bar by incorporating a simplified local density model gas adsorption [14]. Finally, the Bender EOS also uses empirical relationships to describe adsorption up to 500 bar for nitrogen and methane [15].

3) Molecular simulation

In this thesis, adsorption is studied using molecular simulation [16] in order to estimate thermodynamic properties where experimental data are not available and/or not easily obtained. Simulations have been used to model diffusion processes in porous materials (e.g. water diffusing through graphene-based nanopores) and aid in coarse grained reservoir simulations, which require transport phenomena parameters [17]. For example, recent work has been used to describe the selectivity (i.e., the extent of preferred adsorption onto a framework) of CO_2/CH_4 onto an organic-rich shale framework [18]. Similar recently published work shows the interplay between CO_2 and CH_4 adsorption observed in experimental samples for Barnett 26-Ha, Haynesville GU1-2, and Haynesville TWG3-1 rock [19].

To be fair, traditional numerical adsorption techniques in the literature were developed for zeolite and metal-organic framework applications in the low-pressure regime used for describing gas dehydration, small molecule separation, oxygen generation, etc [20]. However, with the recent interest in shale gas, high-pressures applications of the traditional model geometries of adsorption (e.g. slit pore) have led to a range of results from over-predictions to negative adsorption [21]. In addition, the use of inaccurate density calculations by equations of state have led to overcorrections when attempting to link simulation to experimental results [22]. Another objective of this thesis was to correct these limitations in the literature by using the GHC equation of state framework.

1.3 Advancement of Knowledge

Yet another goal of this thesis is to provide the research community at large with shale gas adsorption data at high pressures over a wide range of temperatures and pore throat diameters. These simulation efforts will focus on areas where experimental data is not available. The main contribution of this thesis is the study of internal energies of departure at the nano-scale and the subsequent up-scaling of this molecular information to the bulk scale using the GHC EOS. This work will, in the author's opinion, be quite useful and focuses specifically on molecular simulation to describe shale gas phenomena coupled with applicable examples from the multi-scale Gibbs-Helmholtz constrained equation of state (GHC).

The GHC EOS is unique in the sense that it is thermodynamically rigorous, avoids the need for empirical correlations, and uses information (internal energies of departure)

directly from Monte Carlo simulation to account for interactions on the molecular scale [23]. The GHC EOS uses a simple linear mixing rule for mixtures which is defined by $U_M^D = \sum_{i=1}^{C} x_i U_i^D$ where x_i denotes the mole fraction of the i^{th} component, U_i^D is the pure component internal energy of departure for component i, C is the number of components in the mixture, and the superscript D denotes departure [23]. This mixing rule has been shown to save computational time and easily allow for property and phase equilibrium computations for mixtures. For example, for a mixture of water and methane, molecular simulation would be used to generate U_i^D information for pure water and for methane, and then the mixture rule would be applied to estimate water/methane mixture U_M^D at any composition.

Therefore, the components of this research are:

1) Validate the linear mixing rule for confined fluids. Pure component internal energy of departure data for methane, carbon dioxide and n-alkanes and mixtures of methane/n-alkane & CO_2/n-alkane in confined spaces are gathered using molecular simulation. The linear mixing rule will be applied and compared to results for mixtures. Corresponding percent errors as well as internal energies of departure sensitivities are reported.

2) In the context of adsorption, molecular information is difficult to compute at high pressures. In this work, isothermal adsorption behavior at high-pressure is simulated for mixtures over a wide range of pressures and temperatures. This work investigates the impact of confinement with varying pore throat diameters and hydrocarbon chain length leading to a discussion on their impact on fluid internal energies of departure.

3) Where available, recent adsorption methods [22] are applied and compared to experimental data. This method uses a probing molecule to estimate the accessible pore volume and surface area in order to normalize simulation data for comparison to experimental data. This aspect of the work provides much needed insight for the thermodynamic community.

1.4 References

[1] R. Heller and M. Zoback, "Adsorption of methane and carbon dioxide on gas shale and pure mineral samples," J. Unconv. Oil Gas Resour., vol. 8, no. C, pp. 14–24, 2014.

[2] Dyni, John R. "Oil Shale." 2010 Survey of Energy Resources, no. 22 (2010).

[3] "World Shale Resource Assessments," U.S. Energy Information Administration, 2015. [Online]. Available: https://www.eia.gov/analysis/studies/worldshalegas/. [Accessed: 01-Jan-2017].

[4] D. Murali and F. Aloulou, "Future U.S. tight oil and shale gas production depends on resources, technology, markets - Today in Energy - U.S. Energy Information Administration (EIA)," U.S. Energy Information Administration, 2016. [Online]. Available: https://www.eia.gov/todayinenergy/detail.php?id=27612. [Accessed: 16-Jun-2017].

[5] W. Yufang, Z. Gangyi, B. A. O. Shujing, R. E. N. Shoumai, G. E. Mingna, and Z. Zhi, "Latest Progress and Trend Forecast of China's Shale Gas Exploration and Development," Acta Geol. Sin. - English Ed., vol. 89, no. September, pp. 211–213, 2015.

[6] P. Li, Z. Jiang, M. Zheng, H. Bi, and L. Chen, "Estimation of shale gas adsorption capacity of the Longmaxi Formation in the Upper Yangtze Platform, China," J. Nat. Gas Sci. Eng., vol. 34, pp. 1034–1043, 2016.

[7] P. Charoensuppanimit, S. A. Mohammad, and K. A. M. Gasem, "Measurements and Modeling of Gas Adsorption on Shales," Energy & Fuels, vol. 30, no. 3, pp. 2309–2319, 2016.

[8] K. E. Gubbins, Y. Long, and M. Śliwinska-Bartkowiak, "Thermodynamics of confined nano-phases," J. Chem. Thermodyn., vol. 74, pp. 169–183, Jul. 2014.

[9] Z. Wang, Y. Li, P. Guo, and W. Meng, "Analyzing the Adaption of Different Adsorption Models for Describing the Shale Gas Adsorption Law," Chem. Eng. Technol., vol. 39, no. 10, pp. 1921–1932, 2016.

[10] A. L. Myers and J. M. Prausnitz, "Thermodynamics of mixed gas adsorption," AIChE J., vol. 11, no. 1, pp. 121–127, 1965.

[11] G. D. Barbosa, L. Travalloni, M. Castier, and F. W. Tavares, "Extending an equation of state to confined fluids with basis on molecular simulations," Chem. Eng. Sci., vol. 153, pp. 212–220, 2016.

[12] A. L. Myers, "Equation of State for Adsorption of Gases and Their Mixtures in

Porous Materials," Adsorption, vol. 9, no. 1, pp. 9–16, 2003.

[13] A. Myers and P. Monson, "Adsorption in porous materials at high pressure: theory and experiment," Langmuir, vol. 18, no. 26, pp. 10261–10273, 2002.

[14] A. D. Soule, C. A. Smith, X. Yang, and C. T. Lira, "Adsorption modeling with the ESD equation of state," Langmuir, vol. 17, no. 10, pp. 2950–2957, 2001.

[15] A. M. Puziy, A. Herbst, O. I. Poddubnaya, J. Germanus, and P. Harting, "Modeling of High-Pressure Adsorption Using the Bender Equation of State," vol. 19, no. 2, pp. 314–320, 2003.

[16] E. Thomas and A. Lucia. "Multi-Scale Equation of State Computations for Confined Fluids." Comput. Chem. Eng. 107 (2017): 16–25. doi:https://doi.org/10.1016/j.compchemeng.2017.05.028.

[17] X. Yang, X. Yang, and S. Liu, "Molecular dynamics simulation of water transport through graphene-based nanopores: Flow behavior and structure characteristics," Chinese J. Chem. Eng., vol. 23, no. 10, pp. 1587–1592, 2015.

[18] H. Zhang, X. Zeng, Z. Zhao, Z. Zhai, and D. Cao, "Adsorption and selectivity of CH4/CO2 in functional group rich organic shales," J. Nat. Gas Sci. Eng., vol. 39, pp. 82–89, 2017.

[19] H. Aljamaan, M. Al Ismail, and A. R. Kovscek, "Experimental investigation and Grand Canonical Monte Carlo simulation of gas shale adsorption from the macro to the nano scale," J. Nat. Gas Sci. Eng., pp. 1–19, 2016.

[20] MacGillivray, Lr. Metal-Organic Frameworks: Design and Application, 2010. doi:10.1002/9780470606858.

[21] O. Talu, "Net Adsorption of Gas/Vapor Mixtures in Microporous Solids," J. Phys. Chem. C, vol. 117, no. 25, pp. 13059–13071, Jun. 2013.

[22] G. Chen et al., "Keys to linking GCMC simulations and shale gas adsorption experiments," Fuel, vol. 199, pp. 14–21, 2017.

[23] A. Lucia, "A MultiScale Gibbs-Helmholtz Constrained Cubic Equation of State," J. Thermodyn., vol. 2010, pp. 1–10, 2010.

2 EQUATION OF STATE COMPUTATIONS FOR CONFINED FLUIDS

The following manuscript is published as a special issue in Computers and Chemical Engineering.

- Thomas, Edward, and Angelo Lucia. “Multi-Scale Equation of State Computations for Confined Fluids.” *Computers & Chemical Engineering*, 2017, 1–10. doi:10.1016/j.compchemeng.2017.05.028.

2.1 Abstract

Fluid properties of five binary mixtures relevant to shale gas and light tight oil in confined nano- channels are studied. Canonical (NVT) Monte Carlo simulations are used to determine internal energies of departure of pure fluids using the RASPA software system Dubbeldam et al. [1]. The linear mixing rule proposed by Lucia et al.. [2], is used to determine internal energies of departure for mixtures, U_M^D, in confined spaces and compared to U_M^D from direct NVT Monte Carlo simulation. The sensitivity of the mixture energy parameter, a_M, for the Gibbs-Helmholtz constrained (GHC) equation, confined fluid molar volume, V_M, and bubble point pressure are studied as a function of uncertainty in U_M^D. Results show that the sensitivity of confined fluid molar volume to 5% uncertainty in U_M^D is less than 1% and that the GHC equation predicts physically meaningful reductions in bubble point pressure for light tight oils.

2.2 Introduction

Shale gases and light tight oils (LTO) are important unconventional resources with enormous potential as clean and abundant energy sources. Shales are 'tight' porous media with pore radii < 50 nanometer and permeability < 0.1 milliDarcies. Recent improvements in shale gas and LTO economics are the result of hydraulic fracturing ('fracking') and horizontal well completion; thus shale gas and LTO production is, and will remain, an important part of the US energy portfolio for years to come.

One of the many open challenges in developing consistent models that couple fluid phase behavior in tight porous media (i.e., confined spaces) with models for multi-phase flow and transport is the accurate description of rigorous phase behavior in tight porous media. The Gibbs-Helmholtz Constrained (GHC) equation is a predictive, multi-scale equation of state (EOS) that up-scales molecular information in the form of internal energies of departure, U_M^D, which is solely determined from Monte Carlo simulations, to the bulk length scale to build estimates of the well known cubic equation energy parameter,a_M. The energy parameter is then used to determine molar volume and, in turn, pressure. Details of the derivation of the GHC equation can be found in Lucia et al. [2]. In a recent paper, Kelly and Lucia [3] have validated the linear mixing

$$U_M^D = \sum_{i=1}^{C} x_i \, U_i^D \qquad 2.1$$

for internal energies of departure for mixtures, U_M^D, in unconfined spaces in the NPT ensemble. In Eq. 2.1 x_i denotes the mole fraction of the i^{th} component, U_i^D is the pure component internal energy of departure for component i, C is the number of components in the mixture, and the superscript D denotes departure. The fact that Eq. 2.1 is valid for mixtures is important because only pure component internal energies, U_i^D, as functions of temperature, T, and pressure, p, are needed to model mixtures. The internal energy of departure, $U^D = U - U^{ig}$, is negative of the residual internal energy (e.g., see p.128 in Walas [4])

This paper focuses on the computation and accuracy of using Eq. 2.1 to model mixture internal energies of departure in confined spaces and the resulting sensitivity of the energy parameter, molar density, and bubble point pressure to uncertainty in U_M^D. The open literature is surveyed in Section 2.3. Section 2.4 describes the methodology used to compute internal energies of departure in confined spaces. Section 2.5 presents the main computation results, which compare U_M^D in confined spaces computed using the linear mixing rule to those from direct Monte Carlo simulation. Sensitivity analyses are presented in Section 2.6 and conclusions are drawn in Section 2.7. Appendices 6.1.1-6.1.5 contain details for the computational results in Section 2.4.

2.3 Literature Survey

Interest in physical properties and phase behavior of shale gas and LTO is relatively recent and the literature on the subject is somewhat sparse. Early studies in reservoir and petroleum engineering from the 1940's to 2000 [5] suggested that capillary effects on phase behavior were negligible. However, all recent studies, which are largely numerical in nature, include interfacial tension between immiscible phases as part of the model. See [6]–[9].

The current approach to modeling fluid properties and phase equilibrium in tight pores in reservoir simulation consists of

1) An equation of state, e.g., [10]–[12]
2) A correlation (e.g., the parachor equation [8] or MacLeod-Sugden correlation [13] to calculate interfacial tension, s.
3) An estimate of capillary pressure, $p^{cap} = \frac{2\sigma}{r}$ (e.g., using the Young-Laplace equation or Leverett J functions) [14].
4) A difference in phase pressures for each immiscible phase given by $p^{cap} = p^V - p^L$.

For example, Tan and Piri [12] use the PC-SAFT and Young-Laplace equations and a surface tension correlation to model light gas/oil phase behavior in nanopores. However, all current methods for fluid properties and phase behavior in confined spaces (1) rely heavily on empirical relationships such as correlations for interfacial phenomena (or capillary pressure) that require accurate phase densities and/or

regression to experimental data and (2), are correlative, not predictive, and (3) can be inaccurate (i.e., give poor estimates of phase properties and equilibrium in pores).

2.4 Computational Procedure for Internal Energies of Departure

The material in this section describes the Monte Carlo simulation methodologies used to model physical properties of unconfined and confined fluids.

2.4.1 The Unconfined NPT Ensemble.

Kelly and Lucia [3] have clearly demonstrated that the linear mixing rule given by Eq. 2.1 can be used to estimate internal energies of departure of mixtures in the unconfined NPT ensemble and that uncertainties in any pure component U_i^D introduce very little error in the resulting computation of fluid density. See Kelly and Lucia [3] for the details used in computing internal energies of departure in the NPT ensemble using the MCCCS Towhee software system, version 7.10 [15].

However, in this work, the more recent RASPA software was used for all Monte Carlo simulations [1]. Therefore, the first issue to be resolved is to show that the same statistical results for unconfined NTP Monte Carlo simulations can be obtained for mixtures studied by Kelly and Lucia [3] using RASPA. Table 2.1 shows a comparison of NPT Monte Carlo simulation using MCCCS Towhee and RASPA for pure components while Tables 2.2 and 2.3 compare mixtures. The numbers in parentheses in Tables 2.1, 2.2 and 2.3 represent standard deviations.

Table 2.1: Comparison of Unconfined NPT U^D_i Using Towhee and RASPA

Species	**Force field**	**N**	**T (K)**	**P (bar)**	U_i^D **(cm³bar/mol)**		**% diff**
					Kelly & Lucia [3]*	This work**	
methane	TraPPE-UA	64	300	200	-2.365×10^4 (1.73×10^2)	-2.300×10^4 (7.2×10^1)	2.79
CO_2	TraPPE	128	273.15	100	-1.1293×10^5 (6.71×10^2)	-1.1563×10^5 (3.26×10^2)	2.36
hexane	TraPPE-UA	32	290	150	-2.8005×10^5 (6.98×10^2)	-2.8103×10^5 (5.13×10^2)	0.35
octane	TraPPE-UA	64	300	200	-3.697×10^5 (7.04×10^2)	-3.695×10^5 (5.85×10^3)	0.054
water	TIP4P-Ew	128	290	150	-4.7000×10^5 (2.99×10^2)	-4.7103×10^5 (7.61×10^2)	0.22

* MCCCS Towhee version 7.10 [15]
** RASPA version 2.0 [1]

Table 2.2: Comparison of Methane/Octane NPT U^D_M Using Towhee and RASPA[a]

x_{CH4}	$\langle U_M^D(T,P)\rangle$	$\langle U_M^D(T,P)\rangle$	**% difference**
	Kelly & Lucia [3]*	This work**	
0.20	-2.9727×10^5	-3.1063×10^5 (3.8×10^3)	4.40
0.50	-1.9512×10^5	-1.9879×10^5 (2.30×10^3)	1.86
0.70	-1.2468×10^5	-1.2433×10^5 (8.90×10^2)	2.81
		ADD	2.18

[a] N = 100, T= 300K, p =200 bar
* MCCCS Towhee version 7.10 [15]
** RASPA version 2.0 [1]

Table 2.3: Comparison of Water/Hexane NPT U^{D}_{M} Using Towhee and RASPA[a]

x_{H2O}	$\langle U_M^D(T,P)\rangle$	$\langle U_M^D(T,P)\rangle$	**% difference**
	Kelly & Lucia [3]*	This work**	
0.25	-3.8646×10^5	-3.8435×10^5 (1.6×10^3)	0.54
0.50	-3.3872×10^5	-3.4261×10^5 (5.20×10^3)	1.14
0.75	-3.0103×10^5	-3.1361×10^5 (3.3×10^2)	4.09
		ADD	1.93

[a] N = 100, T= 290K, p =150 bar
* MCCCS Towhee version 7.10 [15]
** RASPA version 2.0 [1]

For these unconfined NPT simulations, volume, translation, and rotation move frequencies were set to 2.48%, 48.78%, and 48.78% respectively while radial cutoff distances were adjusted to include all interactions in the system. For electrostatic forces, Coulomb interactions were calculated using Ewald summations as defined in Dubbeldam (p. 81, [16]).

For larger alkane molecules, Configurations Bias Monte Carlo (CBMC) summations are needed and the corresponding volume, translation, rotation, and CBMC frequencies were set to 1.23%, 24.69%, 24.69%, and 24.69% respectively. Larger molecules also have torsion and have an ideal gas contribution to the internal energy of departure. For this, additional simulations were performed using a single molecule

in the canonical (NVT) ensemble with CMBC moves. The pressure in the NPT ensemble was measured by computing the negative of the stress tensor as defined in Dubbeldam et al. ([1], [17]) For mixtures, an identity switch move was used with a frequency of 5% to ensure higher mixing probability. Finally, all unconfined simulations were also performed without analytical tail cutoff corrections, and at the same temperature and pressure for the NPT ensemble, for the purpose of comparing confined and unconfined simulation results.

2.4.2 The Confined Canonical Ensemble.

Confined canonical (NVT) ensemble Monte Carlo simulations in this study were performed using the screening study of Dubbeldam [18] and the more recent energy slope method of Poursaeidesfahani et al. [19] using version 2.0 of the RASPA software [1]. These confined simulations used a range of N adsorbate particles, a fixed temperature, and a system volume dictated by a 1 x 1 x 1 rigid unit cell of graphite nano-channels, the latter of which is provided in version 2.0 of the RASPA. Periodic boundary conditions were used in only the longitudinal (x) direction with a cutoff distance of 12 Angstroms (Å). The flexible TraPPE force field model was used for all molecules while the TIP5P force field model was used for water. Translation and rotation moves were used for all molecules with additional CBMC moves for long chain alkanes and Ewald summations for all charged interactions. No analytical tail cutoff corrections were applied in the confined systems since it is assumed that these corrections are not valid when graphite walls are present. In order to compute pressure

in the confined case, a hybrid Monte Carlo move using a Molecular Dynamics move in the micro-canonical (NVE) ensemble was used on every fifth Monte Carlo cycle to compute the negative of the stress tensor, as defined in Dubbeldam et al. ([1], [17]). Moreover, only the configuration of molecules inside the graphite nano-channel was changed when an NVE move was accepted. As in the unconfined case, additional NVT simulations were performed to calculate the ideal gas contribution to quantify torsion effects.

The flowchart shown in Fig. 2.1 gives an overview of the procedure for computing mixture internal energies of departure. For all ensembles, 100,000 equilibration cycles and 100,000 production cycles were used while the number of particles in the system varied with pressure as shown in Appendices 6.1.1 & 6.1.3.

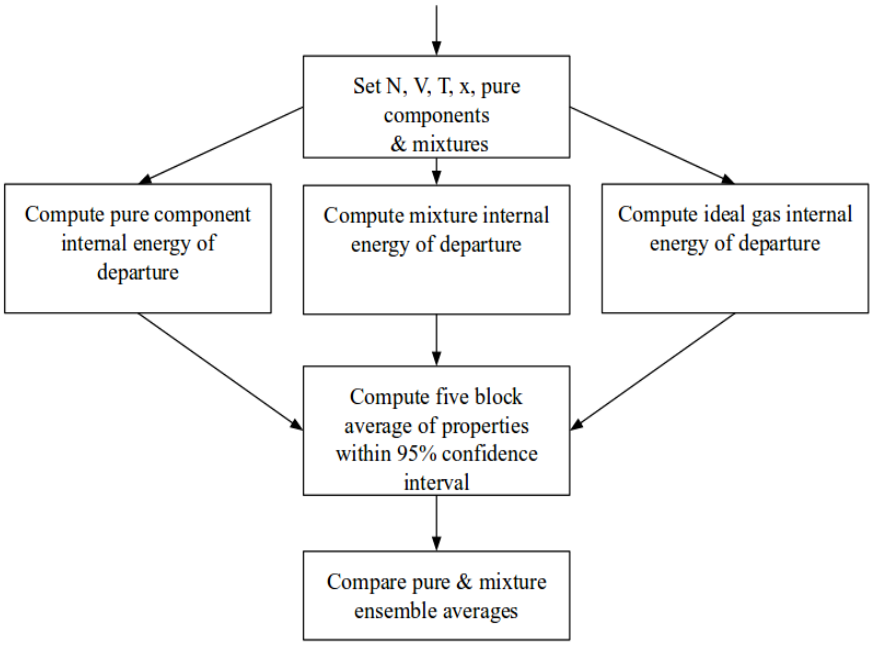

Figure 2.1: Flowchart for Computing Mixture U^{D}_{M}

The system volume was dictated by intersecting graphite sheets to form a graphite nano-channel. Specific values of N, V, and T can be found in Appendices 6.1.1 and 6.1.4. A snapshot of an example is shown in Fig. 2.2.

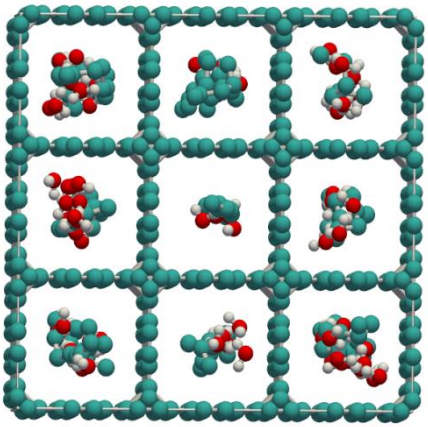

Figure 2.2: Snapshot of NVT Mixture of Water/Hexane (75/25) at 290 K

The framework specifications used in creating a confined nano-channel were as follows:

1. Cell size with a = 39.36 Å, b =25.56 Å , c = 25.56 Å, volume = 25714.42 $Å^3$
2. Framework density = 893.50 kg/m^3.
3. Sheet-sheet distance = 8.52 Å.
4. Free spacing = 5.047 Å.

Framework information can be found in supporting information (S178) of Dubbeldam et al. [18]. Also, while the energies of the graphite walls and inter- and intramolecular energies of the molecules in the nano-channel were computed, the U_i^D and U_M^D results reported for the confined cases only include the energies of the molecules inside the graphite square channels.

2.5 Main Computational Results

Unconfined NPT and confined canonical Monte Carlo simulations were performed for the following five binary mixtures: (1) methane/octane, (2) water/hexane, (3) methane/propane, (4) CO_2/n-hexane, and (5) CO_2/propane. All simulations were run on two custom built computers with AMD 1090T 3.2 GHz and AMD FX8300 processors in double precision arithmetic using the GNU compiler. The main numerical results contained in this section include (1) the determination of confined mixture internal energies of departure and (2) comparisons of confined and unconfined U_M^D from the linear mixing rule with direct Monte Carlo simulation. Details of all pure component U_i^D, pure component critical properties, and additional comparisons of U_M^D from the linear mixing rule with direct Monte Carlo simulation can be found in Appendices 6.1.1-2, Appendix 6.1.3 and Appendices 6.1.4-6 respectively.

Table 2.4 summarizes the comparison of the average absolute deviations (ADD) % errors for U_M^D given by Eq. 2.1 with U_M^D computed from direct Monte Carlo simulations for the confined canonical ensemble as well as unconfined NPT ensemble without analytical tail corrections. Note that the ADD % errors shown in Table 2.4 are smaller for unconfined fluids than confined fluids with the exception of methane/propane. There may be several reasons for this. First, mixing within nano-channels can be problematic due to restricted particle movement and the presence of the nano-channel walls, especially for larger molecules.

Table 2.4: Comparisons of U^D_M the Linear Mixing Rule with Direct Simulation

Mixture	**Confined NVT**	**Unconfined NPT***
methane/octane	4.39	1.33
water/hexane	10.48	3.46
methane/propane	3.08	3.69
CO_2/hexane	10.78	2.7
CO_2/propane	5.48	2.68

* no tail corrections

To help reduce errors associated with mixing in confined spaces an identity switch move was used, which randomly swapped the positions of two different molecules upon acceptance. Second, we did not consider the interaction the molecules of the nano-channel wall in this study.

Tables 2.5 and 2.6, on the other hand, compare confined and unconfined U_M^D for methane/octane at 300 K and 200 bar with direct Monte Carlo simulation.

Note that the linear mixing rule (Eq. 2.1) gives a reasonably good match to direct Monte Carlo simulation in both the confined and unconfined cases with somewhat higher errors for the confined simulations. However, note that the linear mixing rule does capture the correct physics since the values of U_M^D for the confined simulations are more negative than those for the unconfined simulations.

Table 2.5: Confined U^D_M for Methane/Octane at 300 K and 200 bar

	U_M^D $(cm^3 bar/mol)$		
x_{CH4}	**Direct Simulation**	**Linear Mixing Rule**	**% Error**
0.20	-2.3160×10^5 (1.89×10^2)	-2.2510×10^5	2.81
0.50	-1.5856×10^5 (5.09×10^2)	-1.5102×10^5	4.75
0.70	-1.0770×10^4 (3.01×10^2)	-1.0164×10^4	5.62
		ADD%	4.39

Table 2.6: Unconfined U^D_M for Methane/Octane at 300 K and 200 bar

	U_M^D $(cm^3 bar/mol)$		
x_{CH4}	**Direct Simulation**	**Linear Mixing Rule**	**% Error**
0.20	-1.4105×10^5 (4.06×10^3)	-1.3944×10^5	1.1543
0.50	-9.0564×10^4 (2.14×10^3)	-9.1730×10^4	1.2704
0.70	-6.0867×10^4 (6.68×10^2)	-5.9921×10^4	1.5782
		ADD%	1.33

* no tail corrections

More specifically, for methane-octane at 300 K and 200 bar, confined values of U_M^D are approximately 48-56% more negative than unconfined U_M^D at the same temperature and pressure. This is an important fact because more negative values of U_M^D result in higher light gas solubility in oil, which has been observed in light tight oils.

2.6 Sensitivity Analysis

In this section, we study the sensitivity of the energy parameter, a_M, and molar volume, V_M, for the GHC equation of state with respect to uncertainties in pure component internal energies of departure. A sensitivity analysis of bubble point pressure to changes in U_M^D due to confinement is also presented and shows that confinement results in a reduction in gas-oil bubble point pressure. All pure component fluid properties used in these sensitivity analyses can be found in Appendix 6.1.3.

2.6.1 Energy Parameter and Molar Density

Kelly and Lucia ([2]) give the following equations for the sensitivity of a_M with respect to U_M^D in the GHC equation of state

$$\left(\frac{\partial a_M}{\partial U_M^D}\right) = \left[\frac{T}{T_{cM}} - 1\right]\left(\frac{b_M}{ln2}\right) \tag{2.2}$$

$$\Delta a_M = \left[\frac{T}{T_{cM}} - 1\right]\left(\frac{b_M}{ln2}\right)\Delta U_M^D = \left[\frac{T}{T_{cM}} - 1\right]\left(\frac{b_M}{ln2}\right)\sum_{i=1}^{C} x_i \Delta U_i^D \tag{2.3}$$

The sensitivity of molar volume to changes in U_i^Dmust be computed by directly solving the equation of state for its volume or density roots. In Kelly and Lucia [3], the corresponding relative sensitivities of a_M and molar volume (or density) to 5% uncertainty in U_M^D were less than 4% and 1.5% respectively for unconfined fluids with tail corrections. Figure 2.3 summarizes the sensitivity of a_M in the GHC equation to 5% uncertainties in U_M^D for the confined case.

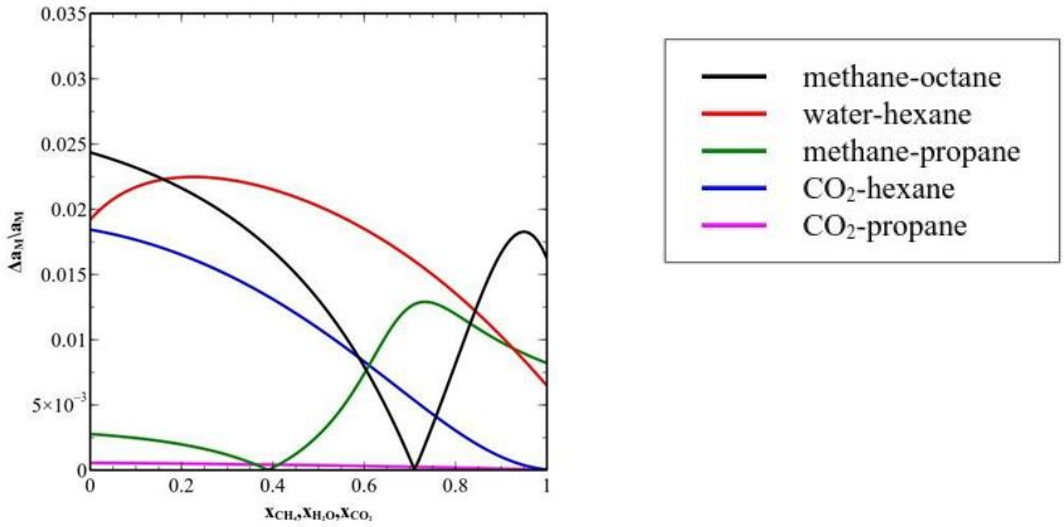

Figure 2.3: Sensitivity of a_M to 5% Uncertainty in Confined U^D_M

Figure 2.4, on the other hand, shows the sensitivity of V_M in the GHC equation to 5% uncertainty in U_M^D for the confined case is less than 1% for all five mixtures studied.

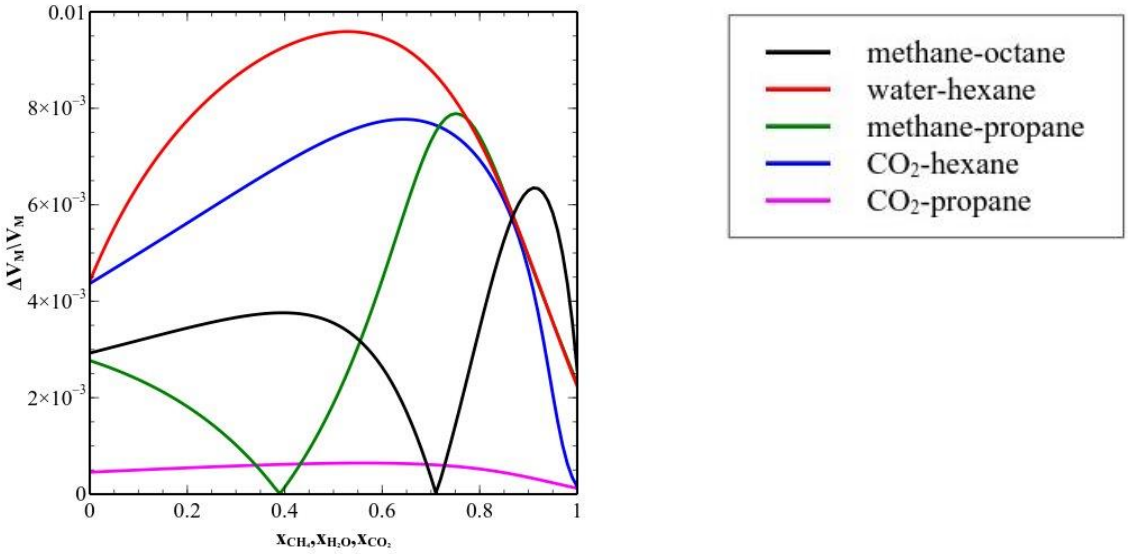

Figure 2.4: Sensitivity of V_M to 5% Uncertainty in Confined U^D_M

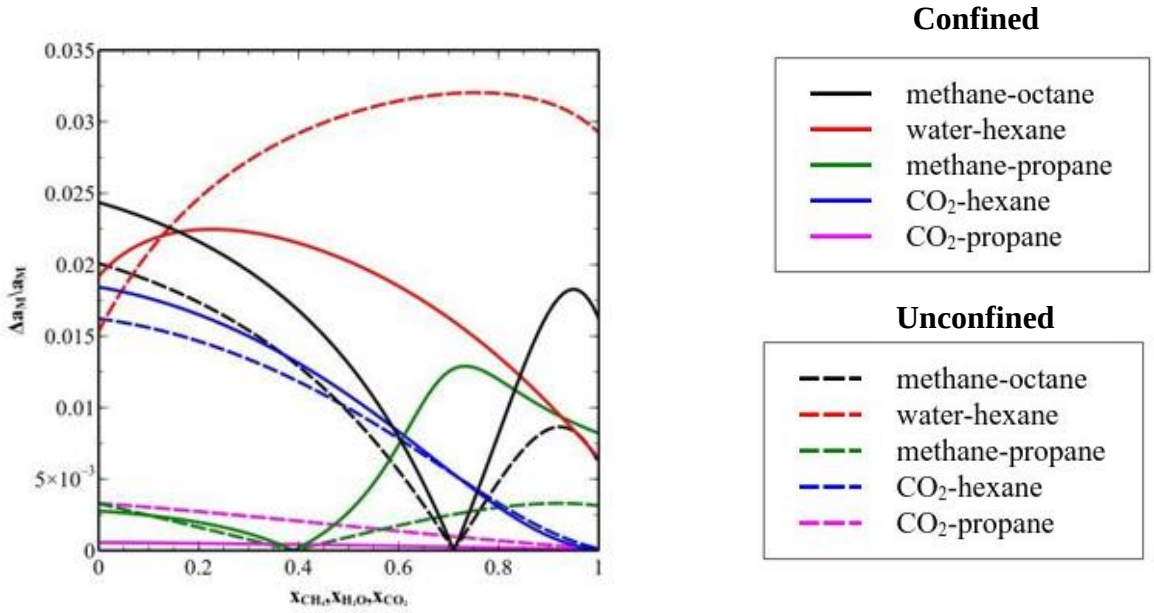

Figure 2.5: Comparison of a_M to 5% Uncertainty in Confined and Unconfined U^D_M

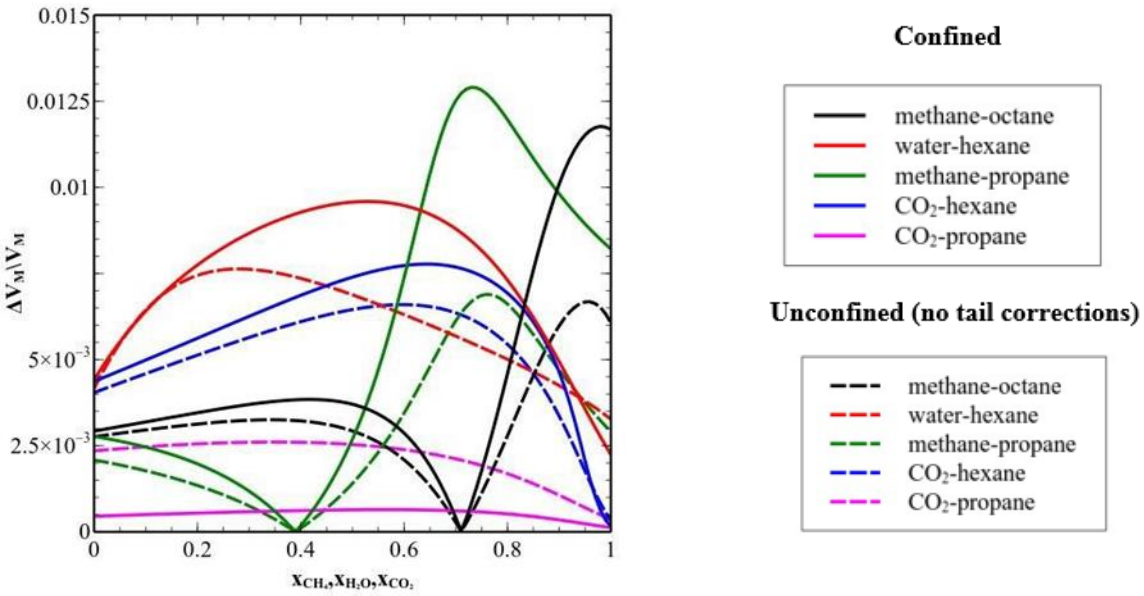

Figure 2.6: Comparison of V_M to 5% Uncertainty in Confined and Unconfined

Note that the maximum sensitivity of a_M to 5% uncertainty in U_M^D does not exceed 3.2% for both the unconfined and confined cases. With the exception of the water-hexane mixture, the sensitivity in a_M in the unconfined and confined cases is less than 0.5%. For water/n-hexane in unconfined and confined space the sensitivity of a_M is approximately 2.5% and 3.2% respectively.

Figure 2.6 shows that the relative sensitivity of V_M for confined fluids is generally higher than that for the unconfined fluids with no tail corrections. Here the exception

is the CO_2-propane mixture, where the trend is reversed and the confined and unconfined fluid sensitivities of fluid molar volume are 0.06% and 0.3% respectively. In addition, the mixture water-hexane exhibits the greatest difference in relative sensitivity (~ 0.4%) while all relative sensitivities of V_M to a 5% uncertainty in U_M^D for both the confined and unconfined mixtures is less than 1%.

2.6.2 Bubble Point

It is straightforward to estimate the sensitivity of bubble point pressure to changes in U_M^D and illustrate that confinement results in a decrease in bubble point pressure.

Let p be any bubble point pressure at fixed x and T. The pressure expression for the GHC equation is

$$p = \frac{RT}{V_M - b_M} - \frac{a_M}{V_M(V_M + b_M)} \tag{2.4}$$

We assume that V_M is insensitive to U_M^D for liquids since previous numerical experiments clearly show it is less than 1%. See also Lucia et al. (Fig. 7, p. 85,[2]). Therefore the partial derivative of pressure with respect to a_M is given by

$$\left(\frac{\partial p}{\partial a_M}\right) = \frac{-1}{V_M(V_M + b_M)} \tag{2.5}$$

Using the chain rule we have that

$$\left(\frac{\partial p}{\partial U_M^D}\right) = \left(\frac{\partial p}{\partial a_M}\right)\left(\frac{\partial a_M}{\partial U_M^D}\right) = -\left[\frac{1}{V_M(V_M + b_M)}\right]\left[\frac{T}{T_{cM}} - 1\right]\left(\frac{b_M}{ln2}\right) \tag{2.6}$$

Note that for the existence of a bubble point requires that $T < T_{cM}$ and therefore the quantity $\left[\frac{T}{T_{cM}} - 1\right] < 1$. Moreover, $(\frac{b_M}{ln2}) > 0$ and $\left[\frac{1}{V_M(V_M+b_M)}\right] > 0$. These facts taken together show that

$$\left(\frac{\partial p}{\partial U_M^D}\right) > 0 \tag{2.7}$$

Therefore the change in bubble point pressure due to confinement is given by

$$\Delta p = \left(\frac{\partial p}{\partial U_M^D}\right) \Delta U_M^D = \left[\frac{1}{V_M(V_M+b_M)}\right]\left[1 - \frac{T}{T_{cM}}\right](\frac{b_M}{ln2})\Delta U_M^D \tag{2.8}$$

where ΔU_M^D represents the change in internal energy of departure of a fluid mixture in confined space minus that in unconfined space at the same x and T. That is, ΔU_M^D in Eq. 2.8 is defined as

$$\Delta U_M^D = \sum_{i=1}^{C} x_i[U_i^{D,c} - U_i^{D,u}] \tag{2.9}$$

Where $U_i^{D,c}$ and $U_i^{D,u}$ are the confined and unconfined pure component internal energies of departure respectively. Substituting Eq. 2.9 into Eq. 2.8 gives.

$$\Delta p = \left[\frac{1}{V_M(V_M+b_M)}\right]\left[1 - \frac{T}{T_{cM}}\right](\frac{b_M}{ln2})\left(\sum_{i=1}^{C} x_i[U_i^{D,c} - U_i^{D,u}]\right) \tag{2.10}$$

Equation 2.10 clearly shows that bubble point reduction is a complex function of composition, temperature, and pore radius because all pure component $U_i^{D,c}$ are functions of temperature and pore radius.

All of the confined U^D data presented in this article thus far corresponds to a pore radius of 0.25 nm which, while valid, is quite small. However, in order to provide bubble point reduction estimates that are more representative of pore sizes encountered in practice, confined NVT simulations were run for a number of pore radii. Table 2.7 shows that the GHC-predicted reduction in bubble point for mixtures of methane and octane confined in pores with a radius of 10 nm, where confined U_{CH4}^D and U_{C8H18}^D at 300 K have values of -2.6180×10^4 and -1.94674×10^5 cm^{3}bar/mol respectively.

Note that the bubble point reductions predicted by the GHC equation are quite reasonable and show the correct composition dependence because confinement generally has a smaller impact on smaller molecules than larger ones. Thus as the methane concentration in the fluid increases, the impact due to confinement decreases, as shown in Table 2.7.

Table 2.7: GHC-Predicted Bubble Point Reduction for Confined CH_4/C_8H_{18} at 300K

x_{CH4}	$(V_M)^*$	$(b_M)^*$	$T_{cM}(K)$	(U_M^D)	(U_M^D)	$\Delta p\ (bar)^c$
0.2	143.734	124.4388	493.146	-1.6907×10^5	-1.3994×10^5	-90.454
0.5	124.543	96.3795	379.665	-1.10427×10^5	-9.1730×10^4	-45.651
0.7	123.552	77.6733	304.011	-7.6728×10^4	-5.9921×10^4	-2.301

[a] Confined U_M^D from linear mixing rule for 10 nm pore radius in units of cm^{3}bar/mol
[b] Unconfined U_M^D from Table 6.1.5; c from Eq. 2.10.; * units of cm^{3}bar/mol

As pore radius increases, confined mixture internal energies of departure should increase and approach the unconfined U_M^D in the limit. Table 2.8 shows this effect of pore radius on the reduction in bubble point pressure for a 50-50 mol% mixture of methane and octane at 300 K.

Table 2.8: GHC-Predicted Bubble Point Reduction for Confined 50 mol % CH_4/50 mol% C_8H_{18} at 300K

pore radius (nm)	U_M^D *confined**	U_M^D *unconfined**	$T_{cM}(K)$
10	-1.10427×10^5	-9.1730×10^4	-45.651
20	-1.07576×10^5	-9.1730×10^4	-38.690
40	-1.04405×10^5	-9.1730×10^4	-30.948

[a] From Eq. 2.10.; * units of cm^3bar/mol

The results in Table 2.8 are qualitatively similar to those reported in Tables 2.5 and 2.6 in Wang et al. (2012) for Bakken oil with 36.7 mol% methane at 240 ^{0}F using a Leverret J function. In that paper, the change in bubble point pressure for pore radii of 10, 20, and 40 nm are 81.63, 43.74, and 22.99 bar respectively. The primary difference is that the GHC equation framework predicts bubble point reduction without the need for data regression or empirical correlations.

2.7 Conclusions

Monte Carlo simulations in unconfined and confined NVT cases were used to compare computed U_M^D by the linear mixing rule compared to direct simulation. The overall ADD % errors found in Table 2.4 clearly show that the linear mixing rule is in agreement with U_M^D computed by direct simulations. Sensitivity analysis were

performed for the mixture energy parameter, molar volume, and bubble point as a function of U_M^D. The results from this analysis show that the uncertainty in U_M^D estimated by the linear mixing rule has a small impact on a_M^D and fluid molar volume v_m for the GHC EOS in both unconfined and confined cases and that the GHC equation correctly predicts physically meaningful bubble point reductions for gas-oil mixtures as a function of composition and/or pore radius.

2.8 References

[1] D. Dubbeldam, S. Calero, D. E. Ellis, and R. Q. Snurr, "RASPA: molecular simulation software for adsorption and diffusion in flexible nanoporous materials," *Mol. Simul.*, vol. 42, no. 2, pp. 81–101, 2016.

[2] A. Lucia, B. M. Bonk, R. R. Waterman, and A. Roy, "A multi-scale framework for multi-phase equilibrium flash," *Comput. Chem. Eng.*, vol. 36, no. 1, pp. 79–98, 2012.

[3] R. B. Kelly and A. Lucia, "On the linear approximation of mixture internal energies of departure," *Comput. Chem. Eng.*, vol. 85, pp. 72–75, 2016.

[4] S. M. Walas, *Phase equilibria in chemical engineering*. Butterworth-Heinemann, 2013.

[5] Y. Wang, B. Yan, J. Killough, and others, "Compositional modeling of tight oil using dynamic nanopore properties," in *SPE Annual Technical Conference and Exhibition*, 2013.

[6] L. Du and L. Chu, "Understanding Anomalous Phase Behavior in Unconventional Oil Reservoirs," in *SPE 161830*, 2012.

[7] B. Nojabaei, R. T. Johns, and L. Chu, "Effect of Capillary Pressure on Fluid Density and Phase Behavior in Tight Rocks and Shales," in *SPE 159258*, 2012.

[8] M. M. Honarpour, N. R. Nagarajan, A. Orangi, F. Arasteh, and Z. Yao, "Characterization of Critical Fluid PVT, Rock, and Rock-Fluid Properties - Impact on Reservoir Performance of Liquid Rich Shales," in *SPE 158042*, 2012.

[9] J. Pang, J. Y. Zuo, D. Zhang, and L. Du, "Impact of Porous Media on Saturation Pressures of Gas and Oil in Tight Reservoirs," in *SPE 161143*, 2012.

[10] D.-Y. Peng and D. B. Robinson, "A New Two-Constant Equation of State," *Ind. Eng. Chem. Fundam.*, vol. 15, no. 1, pp. 59–64, 1976.

[11] L. Travalloni, M. Castier, and F. W. Tavares, "Phase equilibrium of fluids confined in porous media from an extended Peng–Robinson equation of state," *Fluid Phase Equilib.*, vol. 362, pp. 335–341, 2014.

[12] S. P. Tan and M. Piri, "Equation-of-state modeling of confined-fluid phase equilibria in nanopores," *Fluid Phase Equilib.*, vol. 393, pp. 48–63, May 2015.

[13] S. Sugden, "VI.-The variation of surface tension with temperature and some related functions," *J. Chem. Soc.{,} Trans.*, vol. 125, no. 0, pp. 32–41, 1924.

[14] Y. Xiong, P. Winterfeld, C. Wang, Z. Huang, and Y.-S. Wu, “Effect of Large Capillary Pressure on Fluid Flow and Transport in Stress-sensitive Tight Oil Reservoirs,” in *SPE 159258*, 2012.

[15] M. G. Martin, “MCCCS Towhee: a tool for Monte Carlo molecular simulation,” *Mol. Simulat*, vol. 39, pp. 1212–1222, 2013.

[16] D. Dubbeldam, “RASPA 1 . 9 . 15 : Molecular Software Package for Adsorption and Diffusion in (Flexible) Nanoporous Materials,” pp. 1–145, 2014.

[17] D. Dubbeldam, A. Torres-Knoop, and K. S. Walton, “On the inner workings of Monte Carlo codes,” *Mol. Simul.*, vol. 39, no. 14–15, pp. 1253–1292, 2013.

[18] D. Dubbeldam, R. Krishna, S. Calero, and A. Ö. Yazaydın, “Computer-Assisted Screening of Ordered Crystalline Nanoporous Adsorbents for Separation of Alkane Isomers,” *Angew. Chemie - Int. Ed.*, vol. 51, no. 47, pp. 11867–11871, 2012.

[19] A. Poursaeidesfahani, A. Torres-Knoop, M. Rigutto, N. Nair, D. Dubbeldam, and T. J. H. Vlugt, “Computation of the Heat and Entropy of Adsorption in Proximity of Inflection Points,” *J. Phys. Chem. C*, vol. 120, no. 3, pp. 1727–1738, 2016.

2.9 Nomenclature

a, a_M	pure component liquid energy parameter, mixture liquid energy parameter
b, b_M	pure component molecular co-volume, mixture molecular co-volume
C	component
E	total energy in system
L	liquid
N	number of molecules
P	pressure
R	gas constant, radius
T, T_M, T_{cM}	absolute temperature, critical temperature, mixture critical temperature
U_i^D, U_M^D	pure component internal energy of departure, mixture internal energy of departure
V, V_i, V_M	volume, pure component molar volume, mixture molar volume
x	mole fraction
Greek symbols	
σ	interfacial tension
Subscripts/superscripts	
D	departure function
M	mixture

3 UNDERSTANDING PORE-LEVEL PHENOMENA OF N-ALKANES AT HIGH PRESSURES

The following manuscript is submitted to the Journal of Petroleum Science and Engineering.

- Thomas, E. & Lucia. A. (2017). "Understanding Pore-Level Phenomena of N-Alkanes at High Pressures", Submitted to the Journal of Petroleum Science and Engineering.

3.1 Abstract

Adsorption of shale related n-alkane fluids in graphite nano-channels is studied. Pure component canonical (NVT) ensemble simulations are performed over a range of isotherms and pore widths. Results for n-hexane are used to validate our approach by comparing them with experimental data in the open literature. The impact of pore throat diameter on adsorption and internal energies of departure is also reported and further demonstrate that there is a carbon chain length dependence on adsorption. All pure component results reported in this work are fit to a Langmuir adsorption model, which provides easy re-use in future studies. Numerical adsorption results for pure component methane adsorption are compared to experimental reservoir conditions. Finally, Ideal Adsorbed Solution Theory (IAST) is applied to the resulting Langmuir isotherms in order to provide some insight into the phase equilibria for applicable shale gas mixtures.

3.2 Introduction

Fluids in confinement generally have different properties than traditional bulk fluid properties [1]. These unique properties include (1) highly structured geometry [2], (2) decreased mobility in confined directions, which strongly effects sampling pressures [3], and (3) order-disorder transformations in slit-like pores [4]. Applying computational modeling to characterize n-alkanes in confinement has the potential to build fundamental understanding of Light Tight Oil (LTO) and Shale system [5] properties and phase behavior.

3.3 Literature Survey

The recent boom in shale gas technology has led to an increase in global production efforts [6]. In 2013 the United States Energy Information Administration (EIA) estimated the total unproven technically recoverable shale gas reserves across the globe [7] and clearly show that shale gas will play a major role in the world energy portfolio. Some major producers include the U.S. (622.5 trillion ft^3), Canada (572.9 trillion ft^3), Mexico (545.2 trillion ft^3), Australia (429.3 trillion ft^3), Argentina (801.5 trillion ft^3), and Russia (284.5 trillion ft^3). Finally, a staggering 1115.2 trillion ft^3 of shale gas reserves is estimated to exist in China, where great progress has been achieved with the first commercial horizontal well to recover $16.7x10^4$ m^3/day after 15 stages of fracturing [8].

There are also a number of experimental investigations across the globe. Here we review methods and data applicable to the work in this paper. Recent findings in the lower Silurian marine shale of the Longmaxi Formation (Upper Yangtze Platform, China) has yielded data for methane adsorption up to 109.4 bar [6]. In addition, adsorption profiles for methane and carbon dioxide were experimentally determined for the Barnett 31, Marcellus, Eagle Ford 127, and Montney formations up to approximately 117.2 bar [9]. Additional data can be found for methane, nitrogen, and carbon dioxide on Woodford shale from the Payne, Hancok, and Caney county formations up to 125 bar [10]. At higher pressures, the results have been difficult to obtain due to the complexity of the interactions of adsorbed gases inside confined pores such as nanoporous (< 50 nm) shale rock [3]. To circumvent this, models have

been developed to account for these interactions at high pressures. These models are not limited by varying pore throat sizes and shape distribution in the nanometer regime, chemical composition, surface area profile, etc. and typically rely on empirical methods for adsorption modeling. In this work, we propose a methodology for predicting adsorption isotherms of shale gas molecules at high pressures using a slit pore model. Finally, since the adsorption literature is vast, we only highlight methods relevant to our study.

3.3.1 Adsorption Models:

Recent work has reviewed the Henry, Freundlich, Langmuir, Dubinin-Radushkevich, Radke-Prausnitz, Toth, Langmuir-Freundlich models applied to shale gas adsorption for methane and carbon dioxide up to 140 bar [11]. While these models provide excellent agreement with experimental data in the low-pressure regime, the authors note that they typically do not predict high-pressure adsorption due to large interactive forces between adsorbates, pore-filling geometry, and complex adsorbate- wall interactions. Pure component adsorption results have been extended to multi-component systems [e.g. Ideal Adsorption Solution Theory (IAST)] using fitting models [12], [13]. Well-fitted pure component models are essential for predicting multi-component adsorption.

3.3.2 Equation of states (EOS):

There are numerous equations of state derived for the description of adsorption onto a carbon framework that may be used for shale gases. However, most of these equations are regressed to experimental data in order to describe low-pressure adsorption (less

than 100 bar). Myers [14] used a rigorous approach involving desorption functions to derived explicit expressions for G(T,P), in which the author gives an example for ethylene adsorbed on NaX zeolite up to 1.4 bar. Earlier, more empirical work by Myers was based on the use of solution theory by treating the adsorbent as the solvent and small molecules at low concentrations as the solute [15] for adsorption pressures up to 1000 bar. The Elliott-Suresh-Donohue (ESD) equation has been applied to gas adsorption on activated carbon for a number of components including acetylene, propylene, and ethylene for pressures up to 2 bar by incorporating a simplified local density model gas adsorption [16]. A modified Peng-Robinson EOS was used to describe meso-porous materials MCM-41 and 13X for methane and carbon dioxide up to 1.2 bar by using a 16-constant expression [17] fitted to simulated bulk fluid densities in thermodynamic equilibrium with confined media. Finally, the Bender EOS also uses empirical relationships to describe adsorption. In this work, high-pressure adsorption up to 500 bar experimental data is described for nitrogen and methane [18].

Molecular simulation:

Adsorption can be modeled by molecular simulation (Monte Carlo or molecular dynamics) and used to estimate thermodynamic and transport properties where experimental data is not available. Molecular dynamic simulations have been used to obtain diffusion processes in porous materials (e.g. water diffusing through graphene-based nanopores) and aid in coarse grain reservoir simulators which require transport phenomena parameters [19]. Adsorption processes can also be described using Monte Carlo simulations in the grand canonical ensemble. For example, recent work has been used to describe the selectivity (i.e., the extent of preferred adsorption onto the

framework) of CO_2/CH_4 onto an organic-rich shale framework [20]. Similar recently published work shows the interplay between CO_2 and CH_4 adsorption observed in experimental samples for Barnett 26-Ha, Haynesville GU1-2, and Haynesville TWG3-1 rock [21].

There are clearly a limited number of adsorption models applicable to shale gas at high pressures over a wide range of temperatures and pore throat diameters. One novel aspect of this work is the development of a framework based on the Canonical (NVT) Ensemble to compute gas adsorption in regions of high pressures for n-alkanes ranging from methane to hexadecane. The primary goal of this study is to provide a library of adsorption and internal energy of departure data for n-alkanes typically found in the shale gases and light tight oils. In our opinion, this data would be very useful for all research communities that employ multi-adsorption models such as revised multi-component Langmuir models, IAST, and EOS. Furthermore, other recent work from our group has used results for internal energies of departure in confined spaces and a simple EOS linear mixing rule for mixture internal energies of departure to predict bubble point reduction using the Gibbs-Helmholtz constrained (GHC) equation [22]. The proposed work is quite useful for reservoir simulators that desire a predictive and multi-scale thermodynamic approach for the description of shale gas phenomena.

In this work the choice of ensemble is the Canonical approach. It widely known that high-pressure adsorption in the Grand Canonical Monte Carlo (GCMC) ensemble is challenging [23]–[25] and often leads to inaccurate estimates of pore pressure. Difficulties arise when the system becomes denser and, as a result, the acceptance of

insertion moves diminishes, which in turn effects convergence. Low acceptance rates can be computational challenging to resolve, requiring grid interpolation techniques in the GCMC ensemble [12]. In contrast, in the NVT ensemble the pressure can be estimated using the negative of the stress tensor and general fluctuation expressions [26], both of which are implemented in the RASPA software system [27] for both Monte Carlo and Molecular Dynamics applications. However, it is important to note that computing pressure in this manner often requires that the adsorbed fluid be in full contact with the framework [28], which essentially means that there cannot be any void space inaccessible to the fluid. In this work, this requirement is satisfied by choosing a graphite nano-channel where there are no void spaces (see, Fig. 2.2). The main focus of this paper is to define and quantify the impact of confinement on the properties of n-alkanes, specifically adsorption profiles and internal energies of departure (U^D), in spaces that have a range of pore throat diameter. Previous work focused on validating a U^D mixing rule and prediction of bubble point reduction in a confined 50 % molar mixture of methane/octane for the multi-scale Gibbs-Helmholtz (GHC) EOS [22]. As a result, a subsequent goal of this work is to determine the impact of adsorption on computed U^D in confinement within the GHC EOS framework [22], [29].

3.4 Computational Methodology

In this work the nano-channel framework shown in Fig. 3.1 and computational methods developed by Dubbeldam [30] and Poursaeidesfahani et al. [25] were used [i.e., version 2.0 of the RASPA software [27]. All simulations were performed in the

canonical ensemble, where the number of particles, N, was varied for a fixed framework of volume, V, and temperature, T. Periodic boundary conditions were used with a fixed cut off distance of 12 Angstroms and no tail cut off corrections were applied because they are invalid in confinement. Default parameters for the flexible TraPPE force field were used for all molecules with Configurational-Bias Monte Carlo (CBMC) moves for long chain n-alkanes (i.e., carbon number ≥ 4). Hybrid NVE molecular dynamic simulation was also used every 25 moves to adjust the adsorbate configuration and aid in internal mixing. Equilibration and production cycles ranged from 100,000-200,000, each depending on the rate of acceptance of CBMC moves.

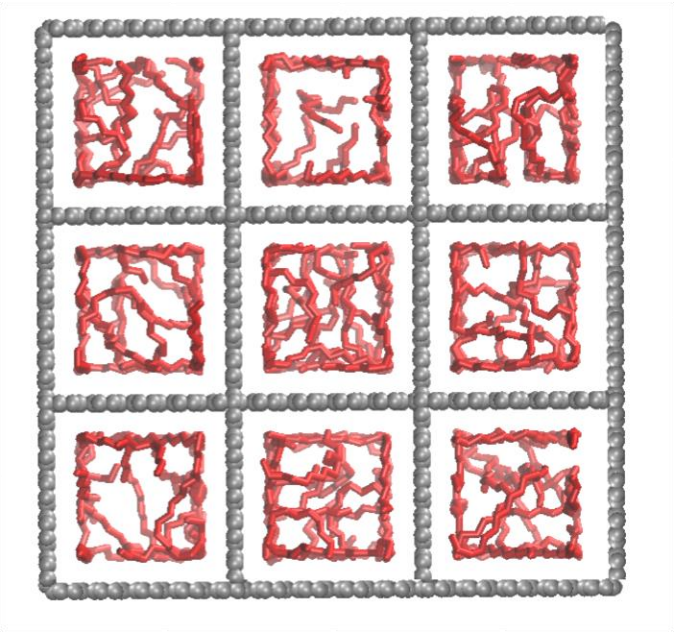

Figure 3.1: Framework and example snapshot of confined hexadecane NVT simulations

The frequencies translation and rotation moves without CBMC moves were set at 50% each. For longer n-alkane chains, starting with butane, the corresponding frequencies for translation, rotation, and CBMC moves were 33.33% each. Reported averages are

the result of using a 5-block average during the production phase of the simulations. Simulations were run on three custom built computers with AMD 1090T 3.2 GHz and AMD FX8300 processors in double precision arithmetic using the GNU compiler. An example snapshot of the simulation is shown in Fig. 3.1 for n-hexadecane. Additional nano-channel framework specifications can be found in the supporting information of Dubbeldam et al. [30], in the nano-channel framework section, and have been reproduced here for convenience. Also, while the energies between the graphite walls and adsorbates were included, U^D results only include energies between adsorbates.

Table 3.1: Nanochannel Framework Specifications

Pore Throat (Å)	**Free Dimension (Å)**	**Sheet-sheet distance (Å)**	**Volume (Å^3)**
2.523	5.047	8.52	25,714.42
5.363	10.727	14.2	71,428.95
8.203	16.407	19.88	140,000.75

*specifications taken from the supporting information of Dubbeldam et al. [30] in nano-channel specifications

An overview of the steps needed to compute adsorption isotherms is given in Fig. 3.2. The general procedure consists of performing a set of simulations in the Cannoical (NVT) ensemble by varying the number of particles, N, at constant V and T. Corresponding energies are computed for each simulation by reporting the block average for a confidence interval of 95%. Pressures are estimated, as noted earlier, by using the negative of the stress tensor and general fluctuation expressions [26]. The stress tensor is only placed upon the molecules in equilibrium on the outside of the slit pore representing a bulk fluid. Adsorption isotherms are then fit to a Langmuir

adsorption model. Ideal Adsorption Solution Theory (IAST) calculations are performed by using the pure component Langmuir adsorption model parameters to predict adsorption for ternary mixtures [13]. The computational procedure is repeated in confined space for a range of pore throat diameters for each n-alkane.

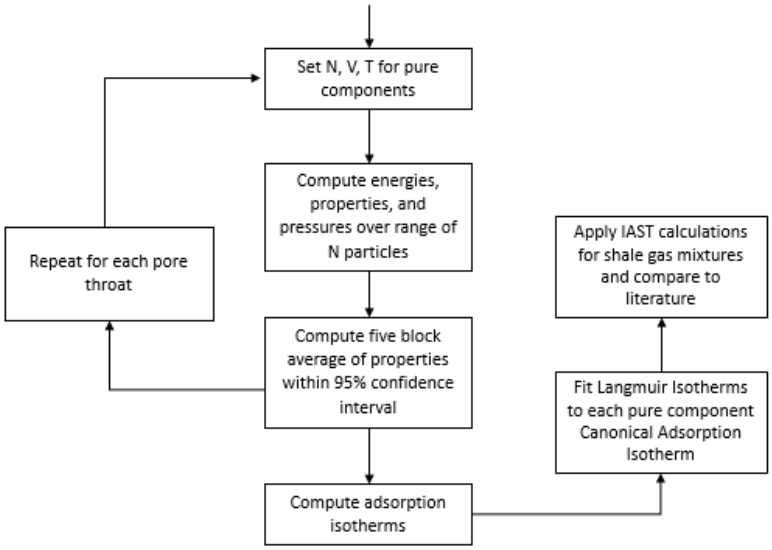

Figure 3.2: Flowchart for Computational Procedure

3.4.1 Benchmark Simulations

Benchmark simulations were used to establish a comparison between the methodology proposed in Fig. 3.2 and the procedure in Dubbeldam et al. [30]. Results of this comparison for U^D are given in Table 3.2 for the NVT and GCMC ensembles. The corresponding pressures for each ensemble can be found in columns 2 and 3 with the standard deviation for the NVT ensemble computed pressures shown in parentheses. It is important to note that the same graphite nano-channel framework (i.e., in supporting information of Dubbeldam et al. [30]) was used for both ensembles. Also, the

computation of U^D is a required component for determining $\Delta H_{i,ads}$, which is described in Dubbeldam et al. [30].

From Table 3.2, it is clear that the results are in very good agreement with a percent error ranging from 1.15 to 3.51%. With the exception of 25 bar, the standard deviations are higher for Dubbeldam et al. [30] than in this work.

Table 3.2: Comparison of GCMC and NVT results for n-Hexane in a 14.2 Å graphite framework

T (K)	**GCMC P (bar)**	**NVT P (bar)****	U_i^D**(cm³bar/mol)****		**% error**
			*GCMC**	*This work*	
433	5	5 (1.91)	-3.291E+05 (8.51E+03)	-3.176E+05 (1.56E+03)	3.51
433	10	10 (3.16)	-3.266E+05 (1.06E+04)	-3.178E+05 (6.00E+03)	2.69
433	15	15 (2.15)	-3.236E+05 (9.13E+03)	-3.181E+05 (7.29E+03)	1.70
433	20	20 (4.69)	-3.257E+05 (9.77E+03)	-3.184E+05 (8.99E+03)	2.23
433	25	25 (5.15)	-3.250E+05 (1.08E+03)	-3.187E+05 (9.18E+03)	1.93
433	30	30 (3.94)	-3.246E+05 (7.79E+3)	-3.190E+05 (1.06E+03)	1.72
433	35	35 (4.59)	-3.230E+05 (8.06E+03)	-3.193E+05 (1.69E+03)	1.15

* supporting information of Dubbeldam et al. [30] for 14.2 Å nano-channel system
** standard deviations in parentheses

In our opinion, the higher standard deviations in the GCMC ensemble are most likely due to the difficulty of performing effective CBMC insertion moves in confined space. Furthermore, Poursaeidesfahani et al. [25] have shown in great detail that computed

properties using the GCMC ensemble are generally higher than those for NVT Monte Carlo simulations in confined spaces.

3.4.2 Langmuir Equation & Ideal Adsorbed Solution Theory

In this portion of the work, the python package, pyIAST, was used to perform Ideal Adsorbed Solution Theory (IAST) calculations for applicable shale gas mixtures [13]. As with all models, there are assumptions and limitations. In this case, a ridged uniform framework was used in the Canonical ensemble, which is valid for IAST. However, a rigid framework implies that thermodynamic properties are independent of volume during sampling because volume is constant [13]. Finally, shale gas in the pore is assumed to be well mixed and each adsorbate has access to the same surface area. Given these assumptions, the following well-known Langmuir equation was used to fit the pure component absolute adsorption data reported in this study

$$n_i = M \frac{KP}{1 + KP} \tag{3.1}$$

where n_i is the pure component adsorbate isotherm, M represents a unique adsorption site, P is the pressure of the adsorbed molecule, and K is a parameter with units of inverse pressure. IAST computations require pure component Langmuir adsorption isotherm parameters to predict mixture compositions of adsorbed molecules in a nano-porous material. A thorough review and validation study of the RASPA package can be found in Section 3.4.1 and in the supplemental materials of Simon et al. [13].

3.5 Simulation Results

Adsorption results for methane, ethane, propane, butane, octane, and hexadecane over wide ranges of temperature, pressure, and pore throat diameter are given in Figs. 3.3-3.14. Results are reported as adsorption isotherms and values of U^D.

3.5.1 Adsorption of n-Alkanes in Graphite Nano-channel System

Fitted Langmuir adsorption isotherms for methane, ethane, propane, butane, octane, and hexadecane are presented in Figs. 3.3-3.14 for the pore throat diameters specified in Table 3.2. These figures plot n-alkane adsorption in moles of adsorbate/kg framework as a function of pore throat diameter ranging from 14.2 to 19.88 Å, temperatures from 300 to 550 K, and pressure up to 550 bar. The dashed lines shown in all adsorption plots represent fits of Monte Carlo simulation data, which are shown as filled symbols, regressed to Eq. 3.1. The results shown in Figs. 3.3-3.14 are discussed in Section 3.5.1 along with key metrics related to confinement. The resulting Langmuir parameters, K and M, can be found in Tables 6.19-24 in Appendix 6.2.

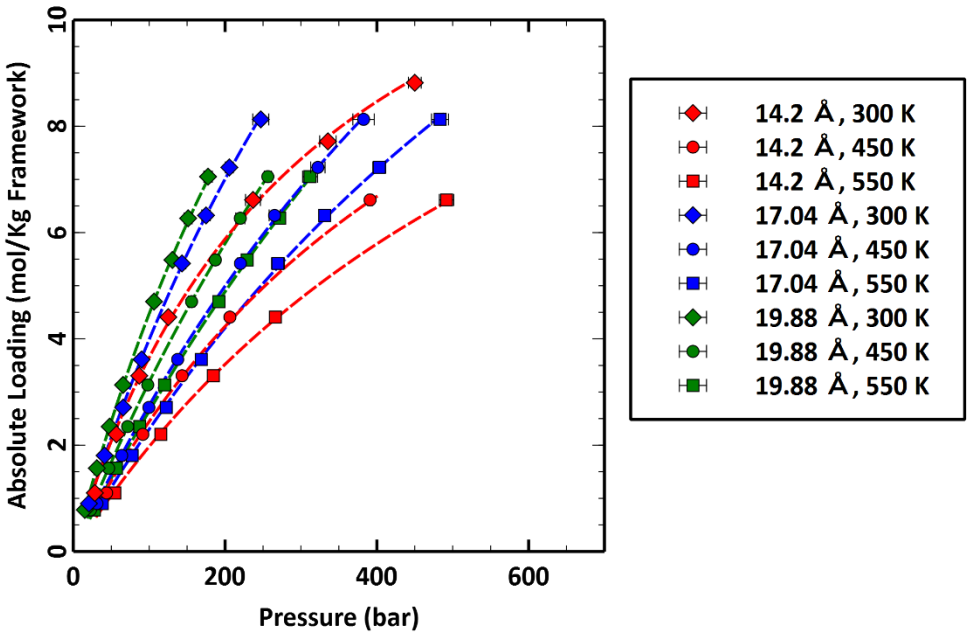

Figure 3.3: Adsorption Isotherms of Methane

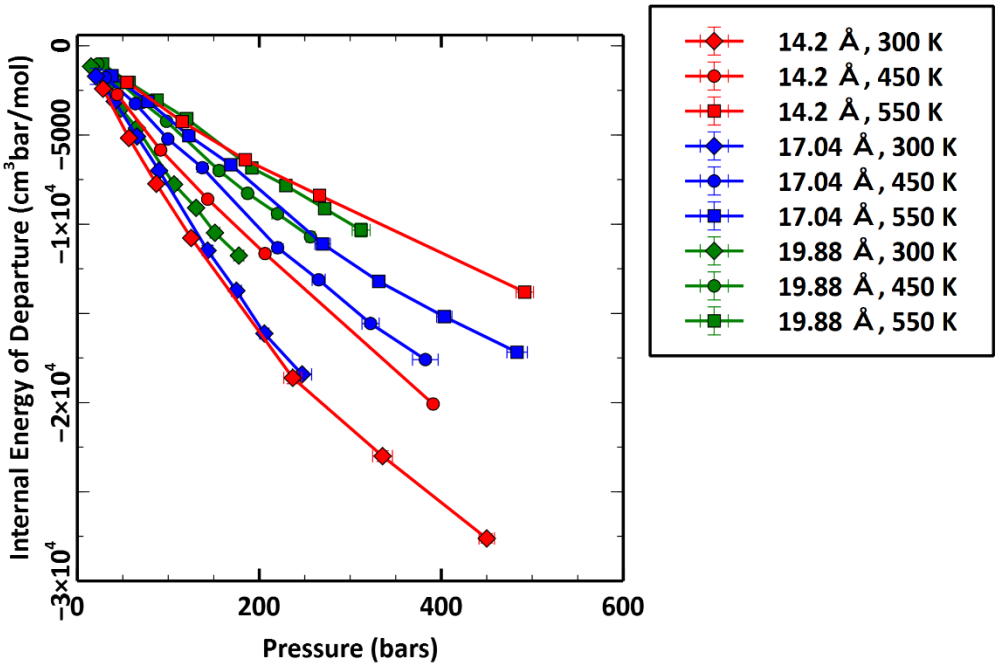

Figure 3.4: Internal Energies of Departure for Methane

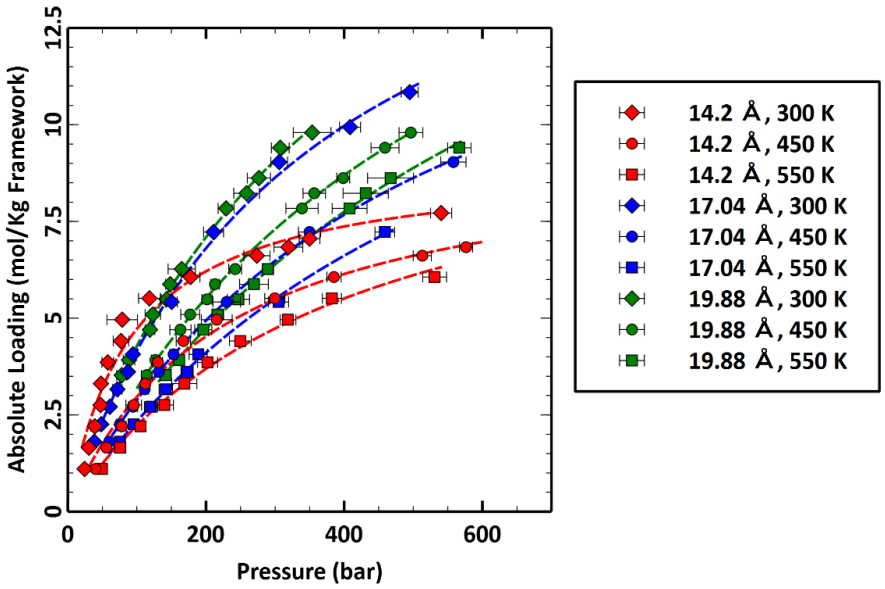

Figure 3.5: Adsorption Isotherms of Ethane

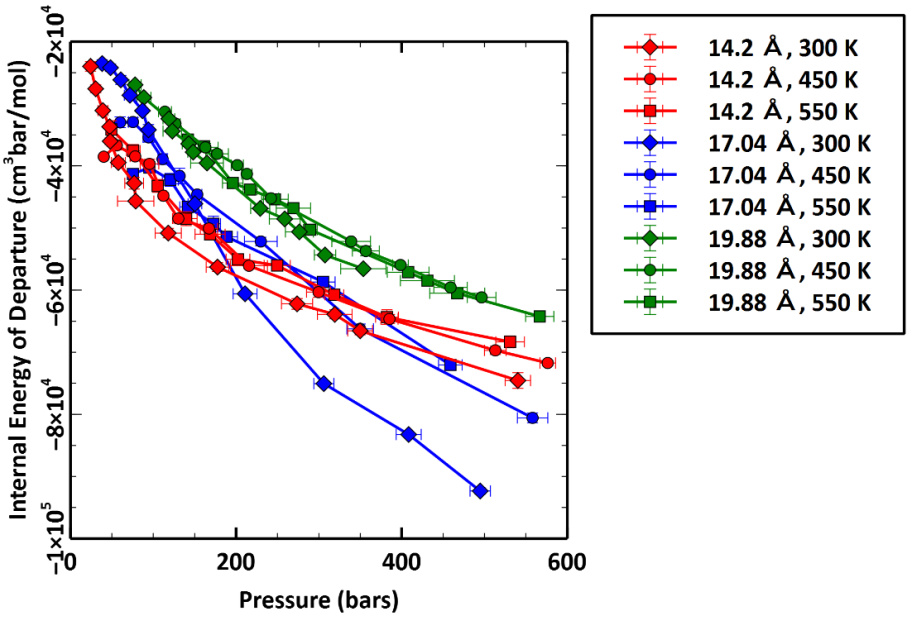

Figure 3.6: Internal Energies of Departure for Ethane

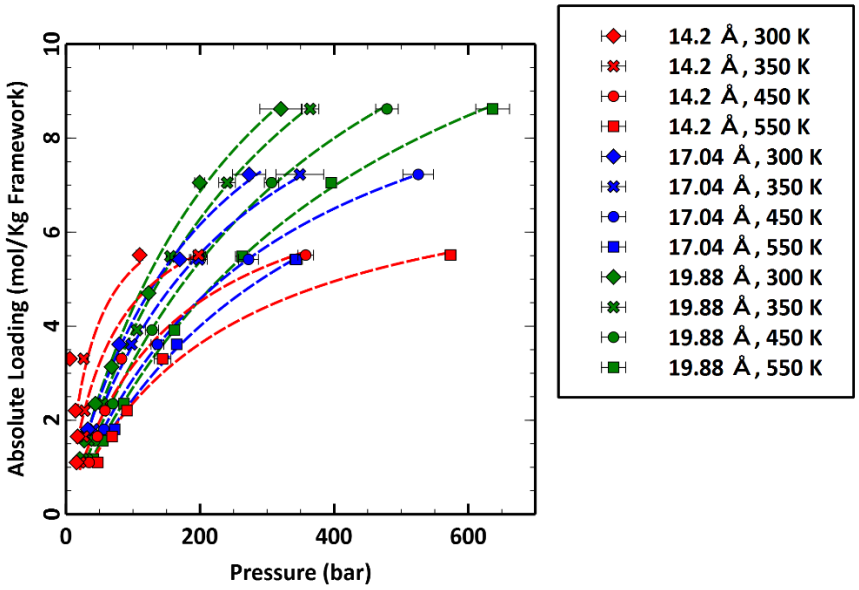

Figure 3.7: Adsorption Isotherms of Propane

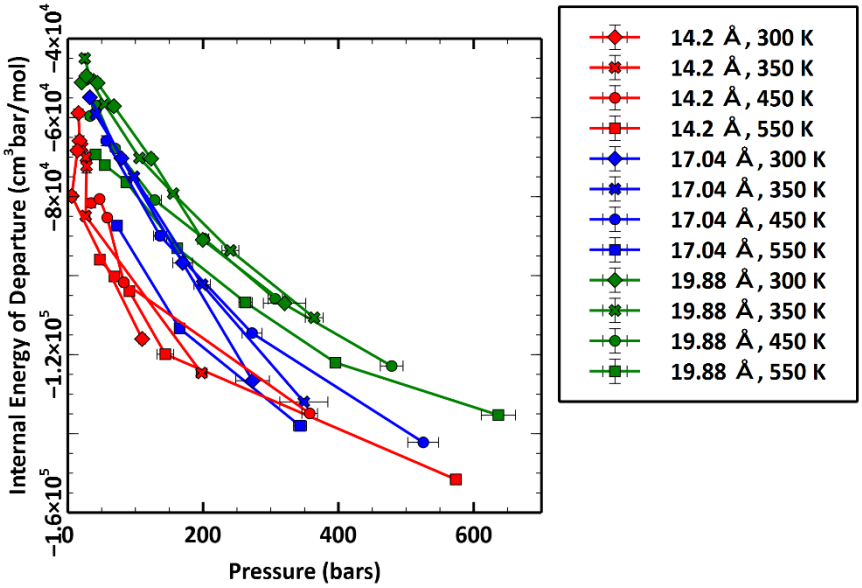

Figure 3.8: Internal Energies of Departure for Propane

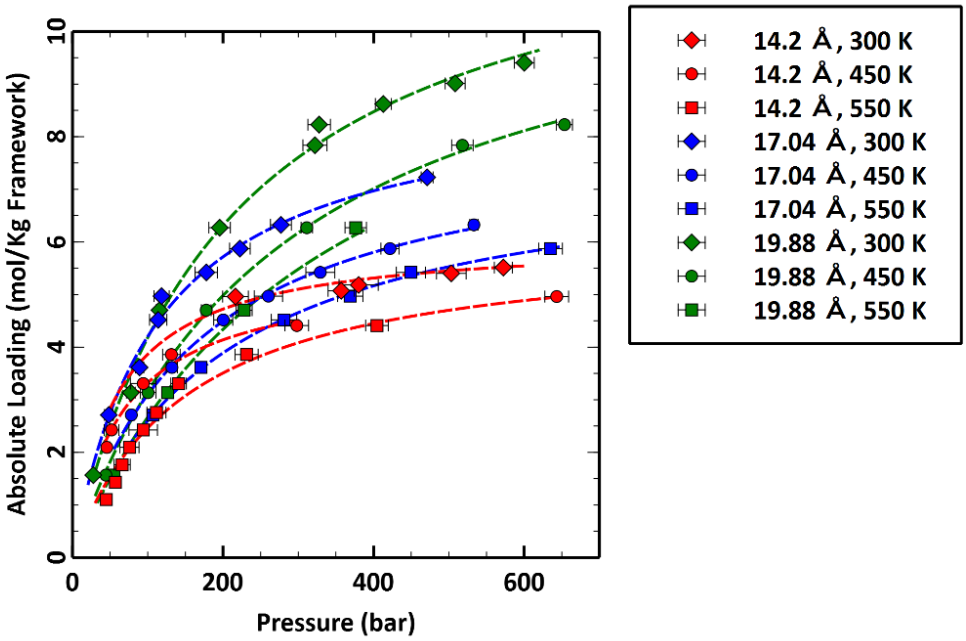

Figure 3.9: Adsorption Isotherms of Butane

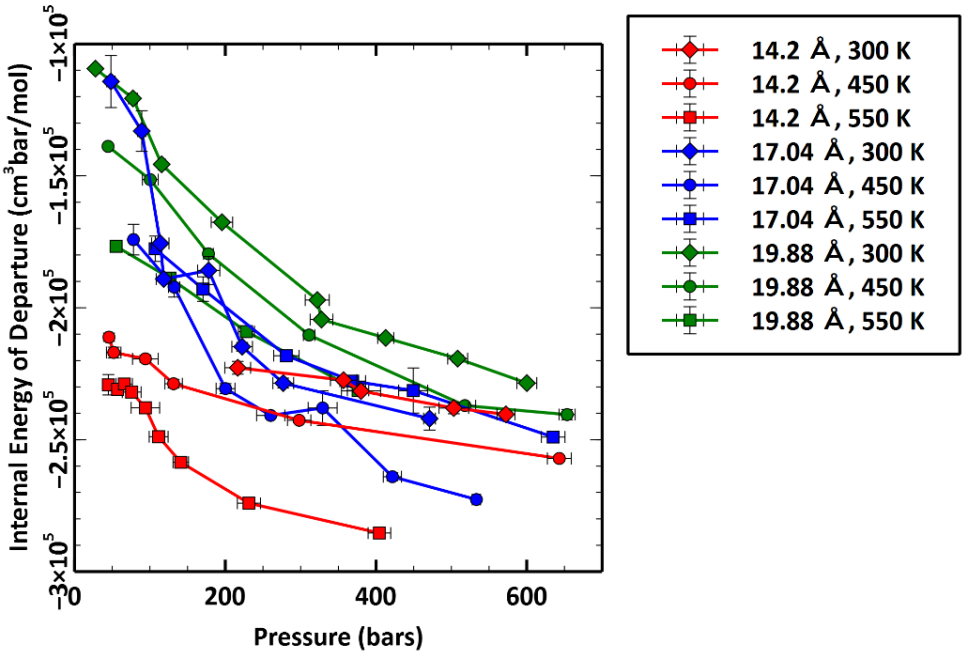

Figure 3.10: Internal Energies of Departure for Butane

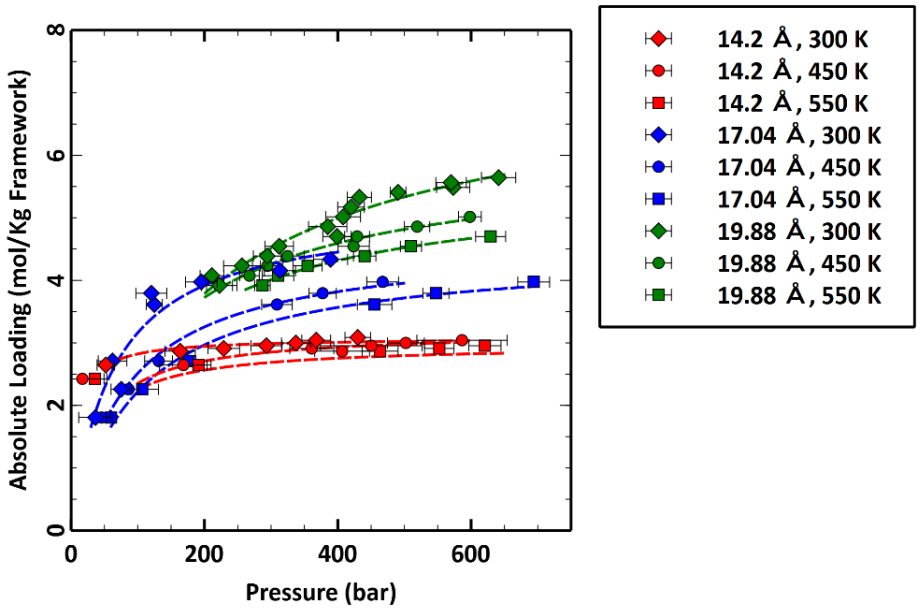

Figure 3.11: Adsorption Isotherms of Octane

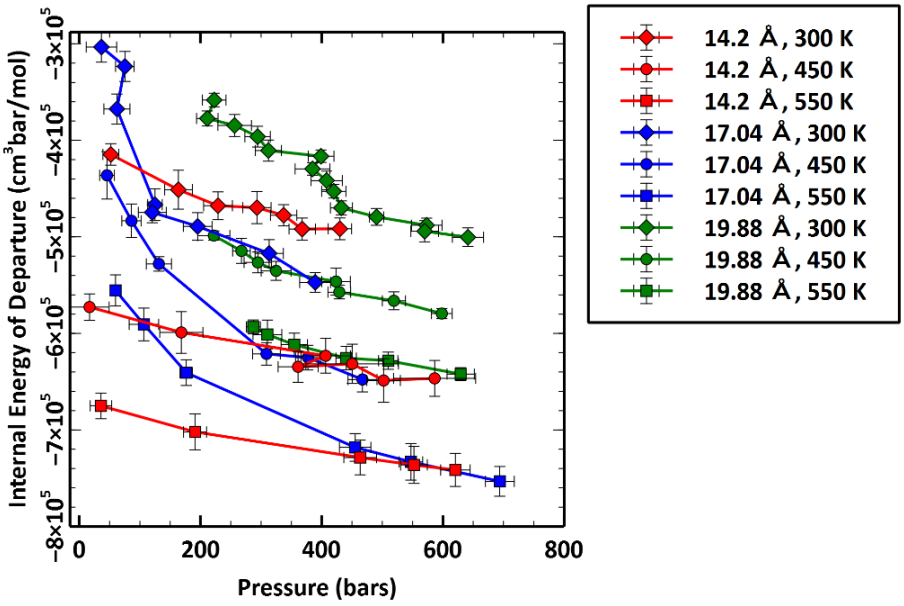

Figure 3.12: Internal Energies of Departure for Octane

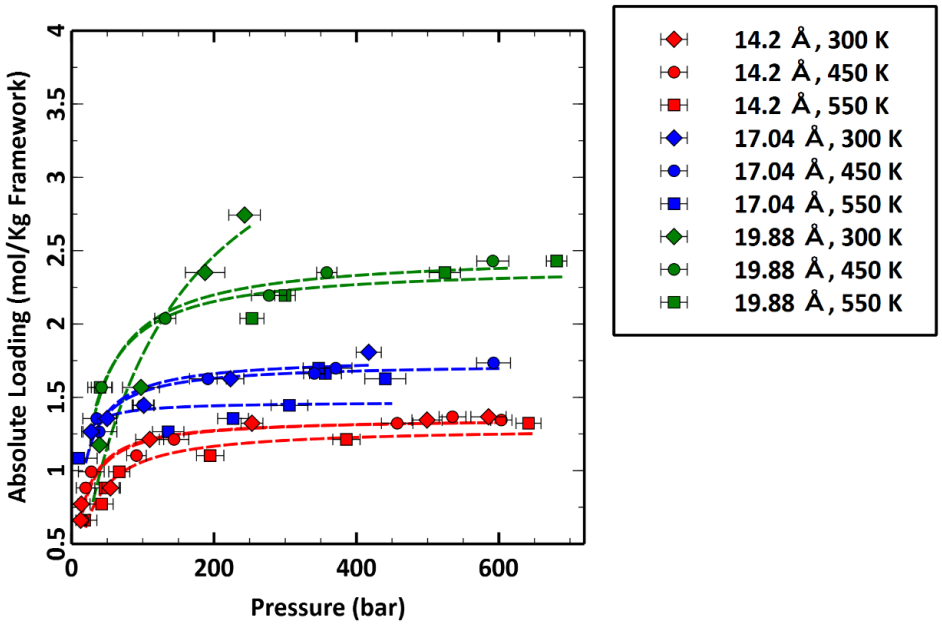

Figure 3.13: Adsorption Isotherms of Hexadecane

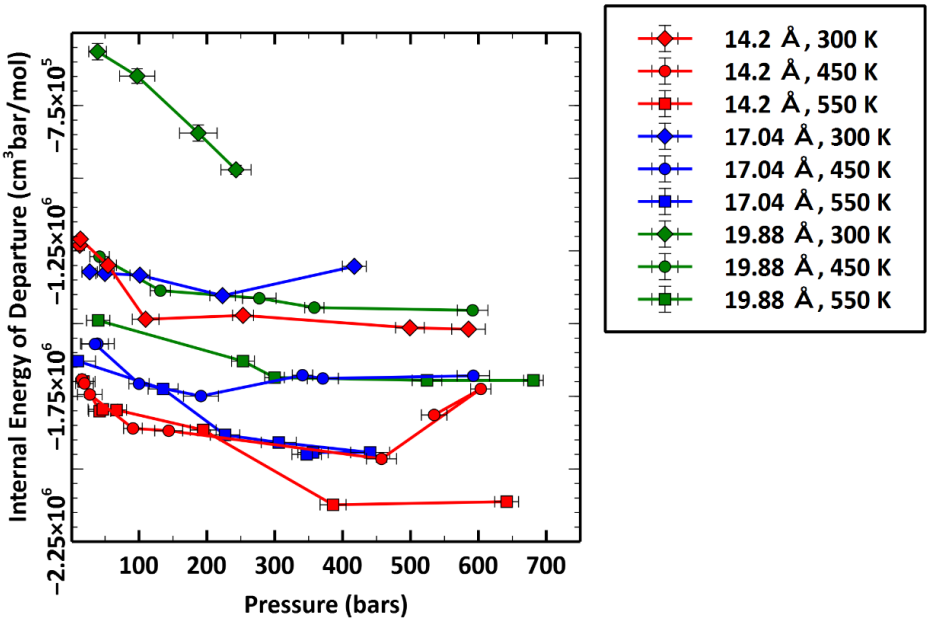

Figure 3.14: Internal Energies of Departure for Hexadecane

3.6 The Impact of Confinement

In this section, the impact of (1) pore throat diameter and (2) chain length (or carbon number) on the internal energy of departure is presented.

3.6.1 Impact of Confinement on U^D

Understanding the impact of confinement on U^D and the adsorption isotherms shown in Figs. 3.3 – 3.14 can be challenging. Summaries of n-alkane fluid behavior induced by confinement are shown in Figs. 3.15 – 3.17. For example, the rate of loading appears to be dependent on carbon number in Fig. 3.15. In general, the smaller alkanes, up to butane, have a greater potential to occupy more pore volume; larger molecules like octane and hexadecane molecules rapidly achieve near maximum loading. However, things are not that simple. Carbon number functionality does not completely describe adsorption phenomenon. Note the difference in the shapes of the curves for methane, ethane, propane and butane compare to those for absolute loading of the larger alkanes octane and hexadecane. The pressure functionality of absolute loading for the smaller n-alkanes has an exponential shape while those for octane and hexadecane are flatter and quickly reach near maximum occupancy between 100 - 200 bar.

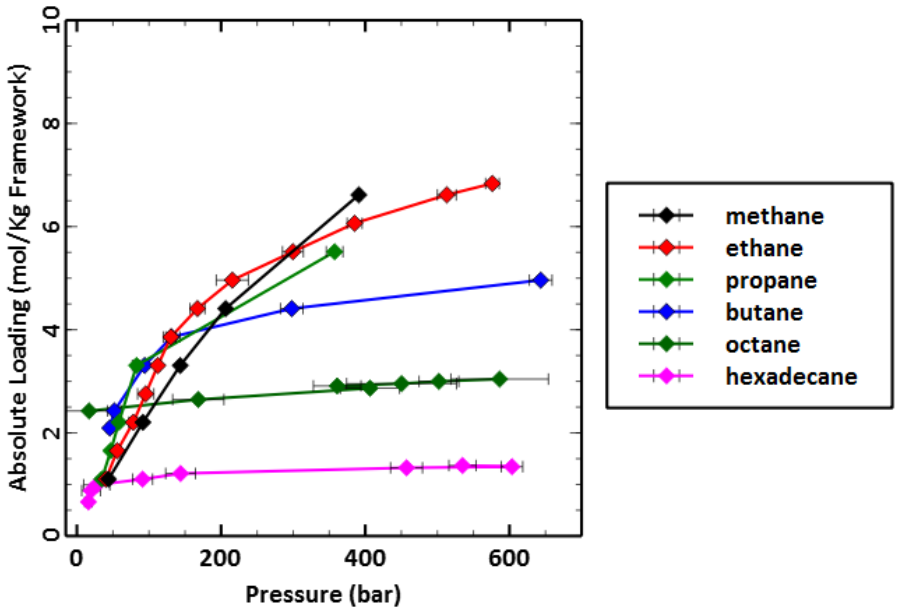

Figure 3.15: Adsorption Isotherms for increasing n-alkane chain length at 14.2 Å and 450 K

This is because the transition to near maximum loading depends, in part, on the interaction between the adsorbate and the nano-channel material. To illustrate absorbate-wall interactions, consider the absorbate-wall interactions for propane, butane, and octane at 300 K for 14.2 Å, which are plotted in the form of a histogram in Fig. 3.16. Note the transition of peaks from left to right in Fig. 3.16 with increasing carbon number. Initially, propane has one peak at 2.5 Å which is expected since it is the center of only three united atom carbon units. However, for butane there are two distinct peaks. The first peak has a lower probability of 0.83 at approximately 3 Å and the second one at 4 Å has a higher probability of 1.0. Finally, there are also two peaks for octane, the first near 8 Å with a 0.55 probability and the second peak at 9 Å with a probability of 1.0. It is clear from Fig. 3.16 that as the number of n-alkane carbons

increases, the molecules tend to favor being 'spread out' along the wall. This well known phenomena, where a layer of adsorbates forms (or condenses) on the walls is a complex function of adsorbate geometry and adsorbate-wall interactions, all of which are influenced by temperature, pressure and pore throat size (see [2], [31],[32]). Moreover, the extent of ordering generally depends on the specific adsorbate and adsorption material under consideration.

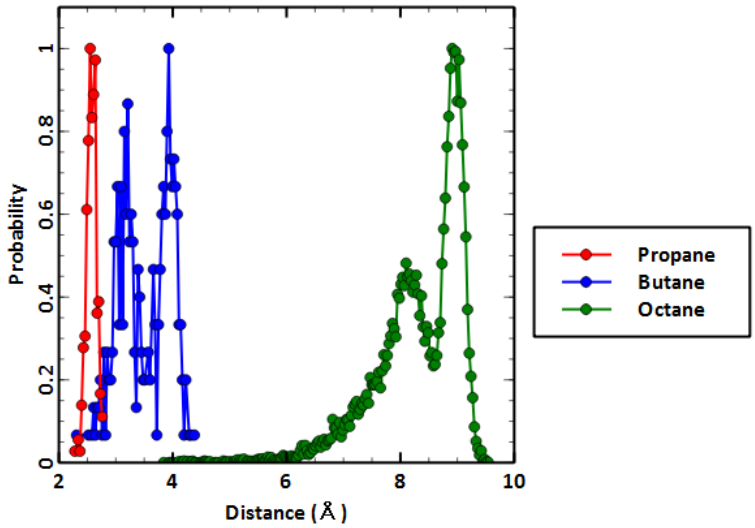

Figure 3.16: Normalized End-to-End Distance Histogram for Propane, Butane, and Octane at 300 K & 14.2 Å

Fig. 3.17 shows that U^D becomes more negative with increasing carbon chain length, which is an indication of stronger non-ideal behavior. With the exception of hexadecane, there is a very weak dependence of U^D with respect to pressure. This, in turn, implies that U^D is a weak function of adsorption and something that could perhaps be exploited when up-scaling confined U^D to the bulk fluid length scale (e.g., for use in an equation of state).

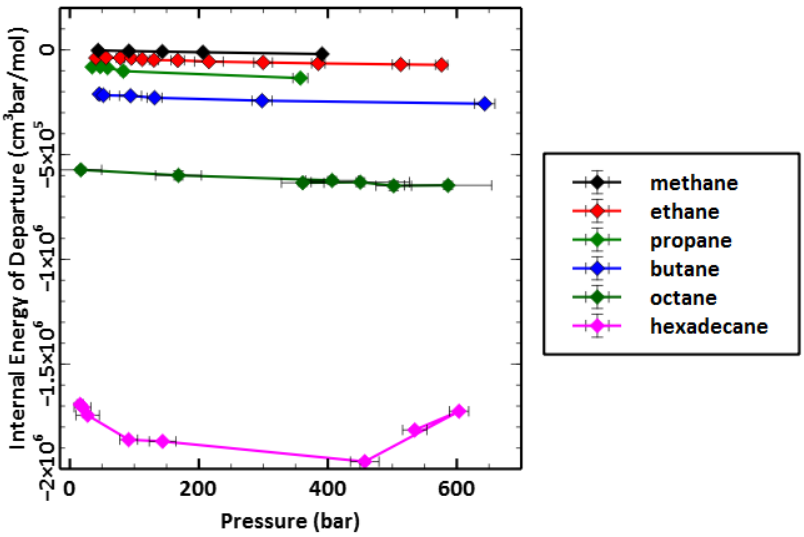

Figure 3.17: U^D of increasing n-alkanes chain length at 14.2 Å and 450 K

3.7 Pore Throat Effects

As noted in section 3.4, an open source python package was recently made available to the thermodynamic community [13] and the IAST portion of this open source code was used to produce the adsorption results in section 3.7.

Case 1: Comparison of simulated methane adsorption as a function of pore throat to experimental data from Heller and Zoback [9].

Experimental data used for comparison is taken from Heller and Zoback [9] who report methane and carbon dioxide adsorption on shale gas samples taken from the Barnett 31, Marcellus, Eagle Ford 127, and Montney shale reservoirs and is shown in Fig. 3.18. Comparisons of the simulated adsorption results presented in Fig. 3.3 from 300 to 450 K for pore throat sizes 14.2 – 19.88 Å to this experimental data were performed by interpolating the simulated results to experimental conditions at 313 K

using the isotherm interpolation technique outlined in [14]. Note that the experimental results compared in this work are for methane at relatively low pressure and extend up to approximately 120 bars while simulation results go up to 450 bar. Also note the proposed simulation methodology provides results that are in qualitative agreement with the experimental data. Again, it is important to stress that our simulation methodology is predictive and not fitted to any adsorption data whatsoever.

The results in Fig. 3.18 clearly demonstrate that a simple slit pore model may be used to predict shale gas adsorption.

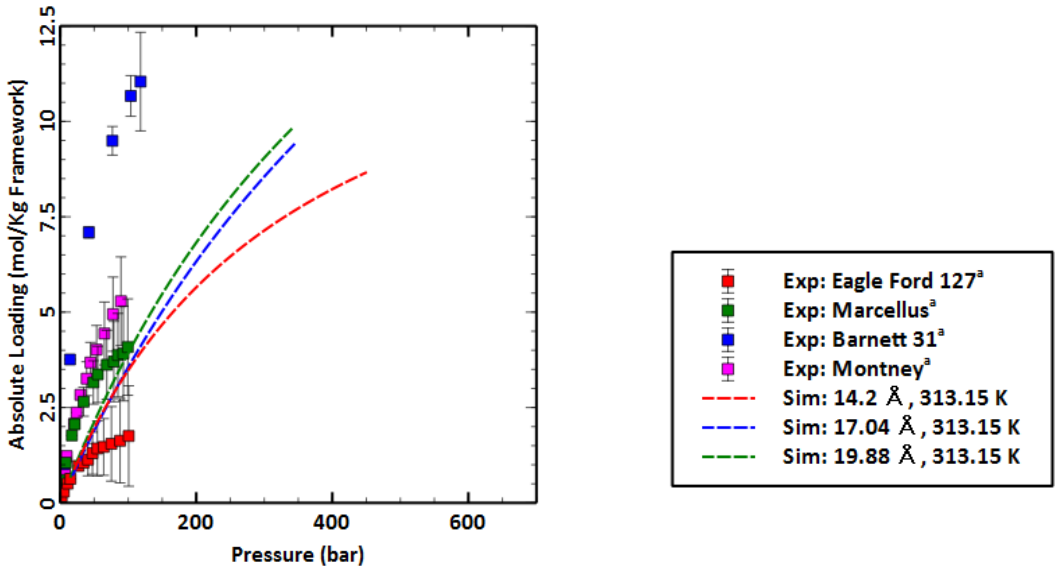

Figure 3.18: Comparison of simulated methane adsorption with the experimental data in Heller and Zoback [9]

Case 2: A recent study [33] used GCMC simulations with the TraPPE force fields for methane and ethane in montmorillonite (MMT) to describe the experimental reservoir composition data shown in Table 3.3.

Table 3.3: Composition of Marcellus and Barnett Shale Wells

Components	**Marcellus well (%)**	**Barnett well (%)**
Methane	79.4	81.2
Ethane	16.1	11.8
Propane	4.0	5.2
Carbon dioxide	0.1	0.3
Nitrogen	0.4	1.5

*data taken from page 2 Table 1 in [33]

In that work, the authors obtained the data by fixing the temperature at 298.15K and varying pressure up to 60 bar. The data in Table 3.3 does not include the temperature or pressure range of the Marcellus and Barnett Shale wells. Unfortunately Sharma et al. [33] chose temperature and pressure conditions not consistent with average shale reservoir conditions. Therefore we have made conservative comparisons by showing IAST results for the experimental temperature of 313 K and a higher reported experimental pressure at 200 bar described in case 1 [9]. Since Fig. 3.18 in Case 1 demonstrated that a slit pore model has the potential to predict shale gas adsorption, the next step is to fit Langmuir isotherms to all adsorption data in this work (found in Appendix 6.2). IAST calculations can then extend our simulation work to mixtures by using the Langmuir parameters as an input.

IAST calculations were generated to describe the Marcellus and Barnett Shale data in Table 3.3 for the binary mixture 80/20 mol% methane/ethane respectively. The results plotted in Fig. 3.19 show uptake of methane and ethane for pore throat diameters of 14.2 - 19.88 Å up to 70 bar. Since confinement data is dependent on the adsorbate,

nano-porous material, and pore throat diameter, it is difficult to make a direct comparison with the results in Sharma et al. [33] and thus we only provide those results as a reference point. Note that our results and those of Sharma et al. [33] seem to be inconsistent. Our results show higher adsorption of methane than ethane for pore throat diameters of 10 and 20 Å while those of Sharma et al. [33] show the reverse trend (i.e., a higher uptake of ethane than methane). However, the results in Sharma et al. [33] are due to the MMT nano-porous material used to describe the shale framework. In their work, ethane had a higher affinity for MMT than methane, which decreases with increasing pressure and pore size.

A.

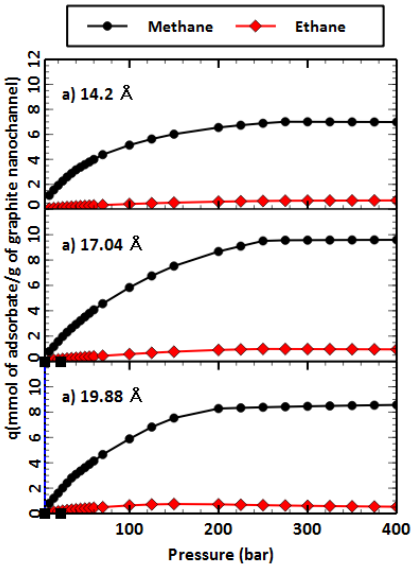

B.

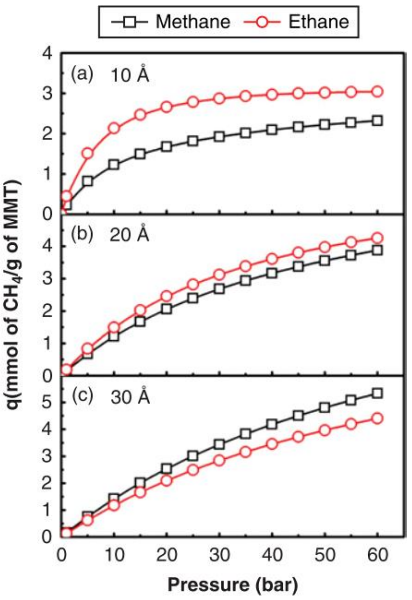

Figure 3.19: IAST results of methane/ethane mixture (A. this work, B. Sharma et al. 2015)

Finally, we used a rigid framework for the nanoporous material (see section 3.4). This makes it possible to use IAST calculations to study the behavior of any multi-component mixtures using the pure component n-alkane Langmuir parameters given in Appendix 6.2, provided we invoke the assumptions given in Simon et al. [13]. Sharma et al. [33] assumed that the 4-5 mol% propane given in Table 3.3 was negligible. Here we extend their approach by adding propane to the methane/ethane mixture and generating IAST calculations for a 79/16/5 mol% mixture of methane/ethane/propane at 313K and 200 bar. The results of uptake for each gas are shown in Figs. 3.20-3.22.

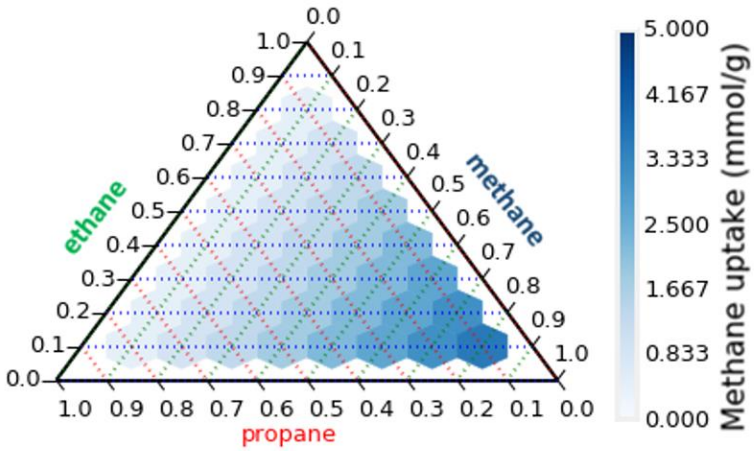

Figure 3.20: IAST Uptake for Methane at 313K & 200 bar for 14.2 Å Sheet-Sheet Distance

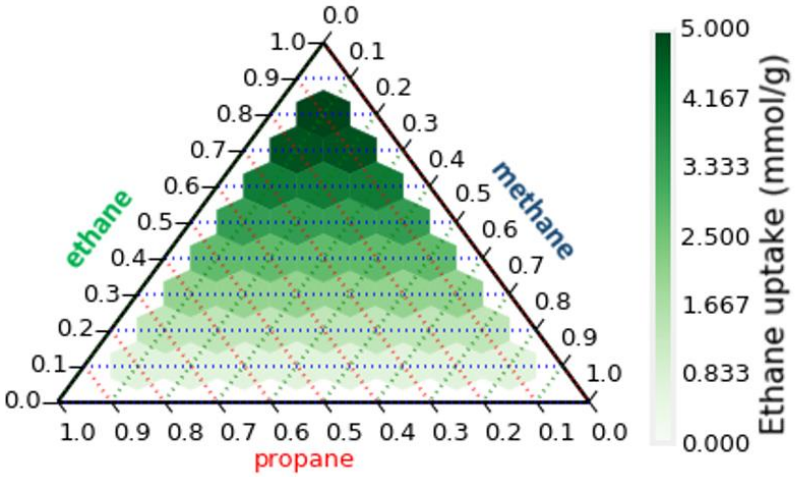

Figure 3.21: IAST Uptake for Ethane at 313K & 200 bar for 14.2 Å Sheet-Sheet Distance

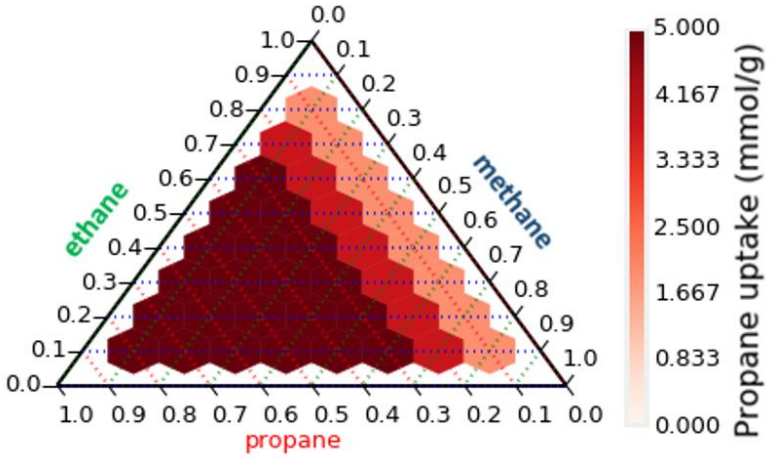

Figure 3.22: IAST Uptake for Propane at 313K & 200 bar for 14.2 Å Sheet-Sheet Distance

A comparison of the ternary mixture in Fig. 3.22 to the binary mixture given in Fig. 3.19 A clearly shows that there is a relatively large amount of propane uptake of approximately 1.6 mmol/g for the given methane/ethane/propane mixture at 313K and 200 bar. What is important to emphasize here is that our adsorption isotherms can be used to provide quick mixture estimations in cases where the composition of propane cannot be neglected. On a broader note, the use of IAST coupled with the Langmuir parameters given in Appendix 6.2 provides a means of quantifying mixing effects of n-alkanes up to hexadecane, which in turn, allows for estimations and references of adsorption conditions.

3.8 Conclusion

In this work adsorption isotherms and UD of n-alkanes in a graphite nano-channel were studied over a range of pressures in the high adsorption regime. Results clearly showed that differences in n-alkane adsorption isotherms decrease overall as the

carbon chain length increases at any given pore throat diameter. This behavior was attributed to occupancy limitations for larger n-alkanes. In addition, adsorption data was fit to Langmuir isotherms and corresponding parameters were determined. Pure component simulation results exhibit similar trends to experimental data (Heller and Zoback [9]) for methane adsorption on shale gas samples taken from the Barnett 31, Marcellus, Eagle Ford 127, and Montney shale reservoirs. The Langmuir parameters for n-alkanes determined in this work can be used within the IAST framework, enabling the larger thermodynamic community to estimate mixture adsorption properties at desired high-pressure conditions. Finally, IAST calculations were used to predict the uptake of n-alkanes at reservoir conditions for the Marcellus and Barnett formations. Results for these studies showed that the affinity of methane decreased for an 80/20 mol% mixture of methane/ethane with an increase in pore throat diameter. The opposite trend was true for ethane in the mixture, which showed a higher affinity with an increase in pore throat diameter. The use of IAST was extended to a ternary mixture of methane/ethane/propane over the entire composition range.

3.9 Acknowledgement

This research did not receive any specific grant from funding agencies in the public, commercial, or not-for-profit sectors.

3.10 References

[1] A. Huerta, O. Pizio, P. Bryk, and S. Sokolowski, “Application of the density functional method to study phase transitions in an associating Lennard-Jones fluid adsorbed in energetically heterogeneous slit-like pores,” Mol. Phys., vol. 98, no. 22, pp. 1859–1869, 2000.

[2] H. Abtahinia and F. Ebrahimi, “Monte Carlo study of structural ordering of Lennard-Jones fluids confined in nanochannels,” J. Chem. Phys., vol. 133, no. 6, 2010.

[3] K. E. Gubbins, Y. Long, and M. Śliwinska-Bartkowiak, “Thermodynamics of confined nano-phases,” J. Chem. Thermodyn., vol. 74, pp. 169–183, Jul. 2014.

[4] L. Salamacha, A. Patrykiejew, S. Sokolowski, and K. Binder, “Lennard-Jones fluids confined in nanoscopic slits: evidence for reentrant filling transitions,” Eur Phys J E Soft Matter, vol. 13, no. 3, pp. 261–265, 2004.

[5] C. L. Cipolla, E. P. Lolon, J. C. Erdle, and B. Rubin, “Reservoir Modeling in Shale-Gas Reservoirs,” Soc. Pet. Eng., vol. 13, no. 4, 2010.

[6] P. Li, Z. Jiang, M. Zheng, H. Bi, and L. Chen, “Estimation of shale gas adsorption capacity of the Longmaxi Formation in the Upper Yangtze Platform, China,” J. Nat. Gas Sci. Eng., vol. 34, pp. 1034–1043, 2016.

[7] “World Shale Resource Assessments,” U.S. Energy Information Administration, 2015. [Online]. Available: https://www.eia.gov/analysis/studies/worldshalegas/. [Accessed: 01-Jan-2017].

[8] W. Yufang, Z. Gangyi, B. A. O. Shujing, R. E. N. Shoumai, G. E. Mingna, and Z. Zhi, “Latest Progress and Trend Forecast of China’s Shale Gas Exploration and Development,” Acta Geol. Sin. - English Ed., vol. 89, no. September, pp. 211–213, 2015.

[9] R. Heller and M. Zoback, “Adsorption of methane and carbon dioxide on gas shale and pure mineral samples,” J. Unconv. Oil Gas Resour., vol. 8, no. C, pp. 14–24, 2014.

[10] P. Charoensuppanimit, S. A. Mohammad, and K. A. M. Gasem, “Measurements and Modeling of Gas Adsorption on Shales,” Energy & Fuels, vol. 30, no. 3, pp. 2309–2319, 2016.

[11] Z. Wang, Y. Li, P. Guo, and W. Meng, “Analyzing the Adaption of Different Adsorption Models for Describing the Shale Gas Adsorption Law,” Chem. Eng. Technol., vol. 39, no. 10, pp. 1921–1932, 2016.

[12] D. Nicholson and N. Quirke, Adsorption and Transport at the Nanoscale. New York: Taylor & Francis, 2005.

[13] C. M. Simon, B. Smit, and M. Haranczyk, “PyIAST: Ideal adsorbed solution theory (IAST) Python package,” Comput. Phys. Commun., vol. 200, pp. 364–380, 2016.

[14] A. L. Myers, “Equation of State for Adsorption of Gases and Their Mixtures in Porous Materials,” Adsorption, vol. 9, no. 1, pp. 9–16, 2003.

[15] A. Myers and P. Monson, “Adsorption in porous materials at high pressure: theory and experiment,” Langmuir, vol. 18, no. 26, pp. 10261–10273, 2002.

[16] A. D. Soule, C. A. Smith, X. Yang, and C. T. Lira, “Adsorption modeling with the ESD equation of state,” Langmuir, vol. 17, no. 10, pp. 2950–2957, 2001.

[17] G. D. Barbosa, L. Travalloni, M. Castier, and F. W. Tavares, “Extending an equation of state to confined fluids with basis on molecular simulations,” Chem. Eng. Sci., vol. 153, pp. 212–220, 2016.

[18] A. M. Puziy, A. Herbst, O. I. Poddubnaya, J. Germanus, and P. Harting, “Modeling of High-Pressure Adsorption Using the Bender Equation of State” vol. 19, no. 2, pp. 314–320, 2003.

[19] X. Yang, X. Yang, and S. Liu, “Molecular dynamics simulation of water transport through graphene-based nanopores: Flow behavior and structure characteristics,” Chinese J. Chem. Eng., vol. 23, no. 10, pp. 1587–1592, 2015.

[20] H. Zhang, X. Zeng, Z. Zhao, Z. Zhai, and D. Cao, “Adsorption and selectivity of CH4/CO2 in functional group rich organic shales,” J. Nat. Gas Sci. Eng., vol. 39, pp. 82–89, 2017.

[21] H. Aljamaan, M. Al Ismail, and A. R. Kovscek, “Experimental investigation and Grand Canonical Monte Carlo simulation of gas shale adsorption from the macro to the nano scale,” J. Nat. Gas Sci. Eng., pp. 1–19, 2016.

[22] E. Thomas and A. Lucia, “Multi-scale equation of state computations for confined fluids,” Comput. Chem. Eng., pp. 1–10, 2017.

[23] D. Khashimova, F. J. Keil, and K. Kholmatov, “Alkanes in Zeolites - Molecular Simulations , Empirical Isotherms, Mixtures,” J. Univ. Chem. Technol. Metall., vol. 43, no. 3, pp. 335–344, 2008.

[24] P. Kowalczyk, H. Tanaka, K. Kaneko, A. P. Terzyk, and D. D. Do, “Grand canonical Monte Carlo simulation study of methane adsorption at an open graphite surface and in slitlike carbon pores at 273 K,” Langmuir, vol. 21, no. 12, pp. 5639–5646, 2005.

[25] A. Poursaeidesfahani, A. Torres-Knoop, M. Rigutto, N. Nair, D. Dubbeldam, and T. J. H. Vlugt, “Computation of the Heat and Entropy of Adsorption in Proximity of Inflection Points,” J. Phys. Chem. C, vol. 120, no. 3, pp. 1727–1738, 2016.

[26] Z. Zhou and B. Joóss, “Fluctuation formulas for the elastic constants of an arbitrary system,” Phys. Rev. B - Condens. Matter Mater. Phys., vol. 66, no. 5, pp. 541011–541017, 2002.

[27] D. Dubbeldam, “RASPA 1 . 9 . 15 : Molecular Software Package for

Adsorption and Diffusion in (Flexible) Nanoporous Materials," pp. 1–145, 2014.

[28] P. Orea and Y. Duda, "Adsorption of hard sphere fluid in porous material : A Monte Carlo simulation approach for pressure," Condens. Matter Phys., vol. 6, no. 4, pp. 573–582, 2003.

[29] A. Lucia, "A MultiScale Gibbs-Helmholtz Constrained Cubic Equation of State," J. Thermodyn., vol. 2010, pp. 1–10, 2010.

[30] D. Dubbeldam, R. Krishna, S. Calero, and A. Ö. Yazaydın, "Computer-Assisted Screening of Ordered Crystalline Nanoporous Adsorbents for Separation of Alkane Isomers," Angew. Chemie - Int. Ed., vol. 51, no. 47, pp. 11867–11871, 2012.

[31] M. Miyahara and K. E. Gubbins, "Freezing/melting phenomena for Lennard-Jones methane in slit pores: A Monte Carlo study," J. Chem. Phys., vol. 106, no. 7, p. 2865, 1997.

[32] M. B. Sweatman and N. Quirke, Modelling gas adsorption in slit-pores using Monte Carlo simulation, vol. 27, no. 5–6. 2001.

[33] A. Sharma, S. Namsani, and J. K. Singh, "Molecular simulation of shale gas adsorption and diffusion in inorganic nanopores," Mol. Simul., vol. 41, no. 5–6, pp. 414–422, 2015.

3.11 Nomenclature

H	Enthalpy
K	Langmuir parameter with units of pressure^{-1}
M	unique adsorption site in Langmuir model
n	pure component adsorbate isotherm
N	number of particles
P	Pressure
T	temperature
U	internal energy

V	volume

Subscripts/Superscripts

s	
abs	denotes an adsorption function
D	denotes a departure function
i	i^{th} component

4 CONNECTING CANONICAL SHALE GAS SIMULATIONS TO EXPERIMENTAL DATA AT HIGH PRESSURES

The following manuscript is prepared for submission to The Journal of Petroleum Science and Engineering.

- Thomas, E. & Lucia. A. (2017). “Connecting Canonical Shale Gas Simulations to Experimental Data at High Pressure”, Prepared for submission to the Journal of Petroleum Science and Engineering.

4.1 Abstract

In order to compare absolute adsorption simulation data to experimental excess and net adsorption data for various adsorption processes, a conversion technique that uses the Gibbs dividing surface derivation to define the upper and lower limits of adsorption phenomena is used [1]. In the context of shale gas adsorption over prediction, a more recent conversion technique has been suggested to normalize both excess and net adsorption data by using the framework surface area to volume ratio [2], which when combined with the Gibbs dividing surface has been shown to be effective when linking simulation to experimental data [2]. The surface area to volume ratio framework has only been employed in the Grand Canonical (GCMC) ensemble. Thus, a new direct conversion approach in the Canonical ensemble is proposed by considering the virial pressure of the bulk fluids in equilibrium with the adsorbants inside the nanochannel slit pore at high pressures. The proposed approach is validated indirectly by Monte Carlo isothermal-isobaric (NPT) simulations and equation of state (EOS) calculations. This validation step defines the accuracy of the bulk fluid properties in the absence of experimental data by establishing a benchmark conversion in the super-critical region. It is shown that using the specific adsorbate molecule for probing the slit pore free volume has a minimal impact on excess and net adsorption. Finally, the conversion adsorption results are compared to existing methods and experimental data with exceptional agreement when compared to traditional methods.

4.2 Introduction

Production of non-conventional hydrocarbon resources is expected to increase throughout 2050 in order to compensate for diminishing conventional reservoir supplies [3]. This has led to an increase in interest in non-conventional reservoirs such as shale gas and light tight oil (LTO) worldwide. Coupled with this effort is the reduction in costs due to technological advances like fracking for major reservoir locations such as the Bakken, Marcellus, and Eagle Ford reservoirs.

The United States remains the world's top producer of natural gas and is in a position to continue to grow the shale gas market [3]. Outside of the United States, production of shale gas in China and Canada are expected to grow from 0.5 to 22 billion and 5 to 8 billion cubic feet per day respectively [3]. It is important to recognize that the growth of shale gas will depend on the market conditions for natural gas that, in turn, are dependent on many other economic factors such as the price of oil. Short term forecasting by the U.S. Energy Information Administration (EIA) predicts oil prices will recover around 2019. However, shale and LTO projections are predicted to increase 1.3 million barrels per day. In the event of a continued oil price downturn, shale gas production will still increase by 35 billion cubic feet per day from 2015 to 2017 [4]. In the long term, shale gas will play a major role in the world energy portfolio and is predicted to increase 70 billion cubic feet per day from 2015 to 2040 [4]. This it is clear that regardless of market conditions, Shale gas will remain a top energy resource in the near future as conventional supplies diminish.

To maximize the efficiency of shale gas production, a comprehensive understanding of the multi-scale problem ranging from the nano-scale to bulk scale is needed. In this work, the focus is on understanding the impact of the nano-scale since it has been demonstrated that the potential maximum efficiency has been hindered by the complex nature of fluid-pore interactions involving pore size, shape, chemical, and surface area distribution of individual pore frameworks [5].

In the nano-scale shale media (< 50 nm), the pore is occupied by a heterogeneous mixture of hydrocarbons and usually the main component is methane ranging in composition from 60 to 80% [6]. The general approach to understanding fluid behavior in nano-porous shale rock is to study the amount of molecules adsorbed, which is intended to provide an estimate of the amount of potentially recoverable gas inside the rock. Since there is a clear absence of experimentally verified mechanisms of adsorption at this scale, the community has used numerical simulations to understand the interactions between the molecules and model porous materials resembling shale rock. These interactions are then up-scaled to the micro- and bulk fluid length scales (e.g., natural gas reservoir simulation). To increase the robustness of the larger scale simulations, a pure component adsorption isotherm database and mixing rules for describing the behavior of multi-component adsorption mixtures. However, it is unclear whether existing numerical simulation results provide accurate estimates of pure component isotherms since many of the studies involve zeolite and metal-organic framework applications in the low-pressure regime used (e.g., gas dehydration, small molecule separation, oxygen generation, etc.). See ([7], [8]). The key problem stems from the fact that modeling of pure component adsorption

isotherms over predict the adsorption by as much as an order of magnitude when compared with experimental data [2].

Therefore the focus of this paper is to construct a robust methodology for linking numerical simulations of adsorption to experimental data in the Canonical ensemble (NVT). Accordingly, the remainder of this article is organized in the following way. A survey of the literature describing community established conversion methods is described in section 4.3. The proposed procedure for adsorption in the NVT ensemble and NPT bulk fluid computations are given in section 4.4. Results are presented in section 4.5 and conclusions of the work are discussed in section 4.6.

4.3 Literature Survey

It is important to emphasize that there are many different computational approaches to studying adsorption using Monte Carlo methods. It is also equally important to highlight that these techniques all have their own advantages and disadvantages. Since the adsorption literature is vast and encompasses many different computational approaches, only a brief overview of pitfalls of Monte Carlo ensemble techniques will be provided in this manuscript.

The classic approach using Monte Carlo to model adsorption is to employ either the Grand Canonical (GCMC) or the Isobaric-Isothermal Gibbs ensemble (NPT GEMC). The choice of the GCMC is convenient because the chemical potential is constant and adsorption is studied over a range of chemical potentials requiring multiple simulations. The bulk pressure from a GCMC ensemble can be obtained by relating chemical potential to an equation of state such as the Peng-Robinson equation [9].

However, adsorption at high pressure conditions in the GCMC ensemble is challenging when the fluid densities is high ([10], [11]. If an EOS is used to relate chemical potential to bulk pressure, there can also be inaccurate estimates of the bulk pressures and densities due to the accuracy of the EOS. Finally, low acceptance rates are reported at high pressures in the GCMC ensemble due to limited particle transfer moves in dense regions ([7]).

Isobaric-isothermal Gibbs ensemble Monte Carlo (NPT GEMC) simulations, on the other hand, are computationally prohibitive because it is difficult to particle transfer moves at constant temperature and pressure. While these simulations are able to provide direct estimates of VLE phenomena and while there is no need to relate the adsorbed chemical potential to the bulk pressure since EOS pressure is explicit in most cases, the Gibbs ensemble transfer moves still impose computational difficulties at high pressures for long chain molecules. Moreover the Gibbs ensemble requires many molecules since there are multiple simulation boxes.

Therefore, following recent work of Thomas and Lucia [12] the canonical ensemble will be used in this work since high-pressure adsorption does not rely on particle transfer moves. The overall approach is described in Thomas and Lucia [12]; here only a brief overview is given in section 6.1.

Once adsorption is obtained through a given Monte Carlo ensemble, the results must be compared to experimental data. This work focuses on relating NVT simulation results to experimental data. In the next sub-section three different methods used for converting absolute adsorption results to excess, net, and surface area adsorption are discussed and compared. Subsequently, these conversion methods are combined and

applied to a canonical (NVT) system and then compared to experimental data for a high-pressure shale gas system.

4.3.1 Excess Adsorption:

Excess adsorption is described by Eq. 4.1 where n_{ex} represents excess adsorption, N is the absolute adsorption from simulation, N_a is Avogadro's number, ρ_g is the bulk fluid density, V_p is the free volume accessible by the adsorbate molecules, and m_s is the mass of the framework. Although the expression for n_{ex} is a simple equation for comparing absolute adsorption to experimental results, there is still great debate in the adsorption literature over the values of V_p and ρ_g at high pressures for shale gas applications [7].

$$n_{ex} = \frac{1}{m_s}\left(\frac{\langle N \rangle}{N_a} - V_p \rho_g\right) \tag{4.1}$$

The determination of ρ_g for high pressure shale gas adsorption must be carefully considered when using an equation of state [13] since recent work has clearly shown that the Peng-Robinson (PR) equation of state (EOS) over predicts ρ_g at high pressures. This, in turn, can lead to negative n_{ex} (see Fig. 5 of Chen et al. [2]. Because n_{ex} is sensitive to values of ρ_g NPT simulations are used to determine gas density at high pressure. In the case of methane there have been many studies that use the PR EOS to convert absolute to excess adsorptions but none of these studies discusses the impact of the accuracy of PR at high pressures [9] on adsorption.

Additional simulations are required to calculate V_p (cm^3/mol), which is typically referred to as the helium void (or dead space) volume as described in Myers and Monson [14]. In this context, helium simulation acts as the reference state for V_p when determining the pore space that is <u>not</u> occupied by the framework. Gumma and Talu [1] demonstrate that this reference volume can be calculated in simulation by use of a configurational integral for helium where ϕ is the collision diameter describing the helium-solid interactions, m_s is the mass of the framework, and Boltzmann constant k.

$$V_p = \frac{1}{m_s}\int_{V_{box}} e^{-\phi/kT} dV \qquad 4.2$$

There remains debate in the adsorption community over the correct values of ϕ for helium as any perturbation in ϕ will result in a different value of V_p thereby affecting the n_{ex}. In fact, some recent work has suggested that the adsorbing molecule be used as the reference molecule [2]. This approach showed a small change in accessible pore volume found in Table 1 of [2] for a Na-Montmorillonite (Na-MMT) simulation cell probed by methane and helium yielding a volume of 40.80 nm^3 and 40.94 nm^3 respectively. Nonetheless, even this small difference in accessible pore volume can lead to noticeable differences in excess adsorption as shown in Fig. 4 of Chen et al. [2]. However, this difference can be attributed to geometric interactions between the framework and the probing molecules because helium is a smaller molecule, than methane and tends to occupy spaces between the surface molecules [2]. An illustrative diagram of the geometric considerations of probing molecules is given in Fig. 6 of Chen et al. [2].

In section 4.5.4, the method of using the adsorbing molecule as the reference molecule for a graphite-nanochannel system is explored further and the effects of helium and methane probing molecules for the determination of V_p are studied. More specifically, for shale gas applications of interest in this work, methane is used as the probing molecule because methane only occupies space on top of the adsorbent surface and not interstitially, thereby occupying less space.

4.3.2 Net Adsorption:

Although the adsorption community typically uses n_{ex} Eq. 4.1 to convert n_{abs} for comparisons with experimental results, there are other methods such as the net adsorption approach. Net adsorption (n_{net}) results have shown promise for high pressure applications [1]. Equation 4.3 provides an expression for n_{net}, where the major difference from Eq. 4.1 is that the V_{box} represents the volume of the simulation box or adsorption reservoir instead of free volume. Thus, with this method, there is no need to use probing molecules to determine V_p. For a rigorous derivation of Eq. 4.3 the reader is referred to Gumma and Talu [1].

$$n_{net} = \frac{1}{m_s}\left(\frac{\langle N \rangle}{N_a} - V_{box}\rho_g\right) \tag{4.3}$$

n_{net} is better suited for framework materials that have an explicit volume such as slit pores and is not suitable for flat surfaces without an explicitly defined volume. Previous applications of the net adsorption approach involve more complex structures such as the metal-organic framework HKUST-1 [1]. As mentioned earlier, great care must be taken for the determination of ρ_g with an EOS.

In Fig. 5 of Gumma and Talu [1] the absolute, excess, and net adsorption isotherms are given for methane on Norit R1 extra at 298 K. At high pressures, negative values of adsorption are predicted by Eq. (4.3) from approximately 220 to 500 bar. Also, inspection of Figs. 5 and 6 in Gumma and Talu [1] clearly show that Eq. 4.3 yields a lower amount of adsobant, most likely because of the higher value of V_{box}. Moreover, over prediction of ρ_g can exacerbate this, especially in comparison to experimental data. In the next section, the effects of ρ_g on Eq. 4.3 using density computations through the PR EOS and NPT simulations are studied.

4.3.3 Surface Area Comparison:

Key findings by Chen et al. [2] attempt to link results of GCMC simulations to experimental data by converting absolute to excess adsorption isotherms. In this work, the authors showed that while bulk fluid densities (ρ_b) and accessible pore volume (V_{free}) are important variables that influence adsorption conversion, the specific surface area (SSA) of the framework is key and demonstrated this for a Na-Montmorillonite system and qualitatively matched experimental results. However, one potential drawback of this method is that it is strongly dependent on the availability of experimental framework SSA data. Furthermore, the SSA approach is also heavily dependent on the type and location of the reservoir. For example, Ji et al. [5] performed an analysis with a Beckman Coulter SA3100 SSA analyzer from a number of shale gas reservoirs. They reported SSAs for monmorillonite (76.4 m^2/g), I-S mixed layer clay (30.8 m^2/g), kaolinite (15.3 m^2/g), chlorite (11.7 m^2/g), and illite (7.1 m^2/g). Fan et al. [15] studied the adsorption of a highly matured sample in Longmaxi (China)

of shale gas system and cited a SSA of 15.10 m^2/g. In this work the surface area of Silurian Longmaxi Formation shales is used, which have areas that range from 17.83 to 29.49 m^2/g [16].

4.4 Overview of proposed work

In this work, NVT simulations are performed for multiple isotherms corresponding to existing experimental data in the open literature [15]. Building on the work of Fan et al., the impact of calculated bulk fluid densities using the conversion of absolute to excess adsorption are compared to results in Setzmann and Wagner [17] as well as isothermal-isobaric (NPT) Monte Carlo, and the Peng-Robinson (PR) equation of state (EOS). Also the impact of V_{free} by probing the framework with helium and methane molecules is studied for use in converting excess adsorption. Applications of these adsorption conversion methods in the NVT and NPT ensembles demonstrate their utility for a model graphite nano-channel systems for shale gas.

4.4.1 Computational Procedure

Figure 4.1 gives a summary of the computational procedure used to determine absolute adsorption isotherms using NVT Monte Carlo simulation and the subsequent conversion of absolute adsorption isotherms to net/excess adsorption curves by a variety of different methods. Simulation temperatures are set to the experimental oil bath temperature in the sample holder given in Fan et al. [15].

The objective of the proposed numerical procedure is to compare simulation results to the experimental results reported by Chen et al. [2]. The proposed computational

methodology addresses the current limitations in the literature that lead to large differences between computationally determined and experimental adsorption profiles. It is important to emphasize that this limitation has been resolved for the grand canonical ensemble but not for the canonical ensemble [2]. Here adsorption in the Canonical ensemble is addressed and direct (virial pressure) and indirect (NPT & EOS) methods are used to compute bulk pressure, as described in section 4.5. Bulk pressure combined with the excess adsorption (Eq. 4.1), net adsorption (Eq. 4.3), and

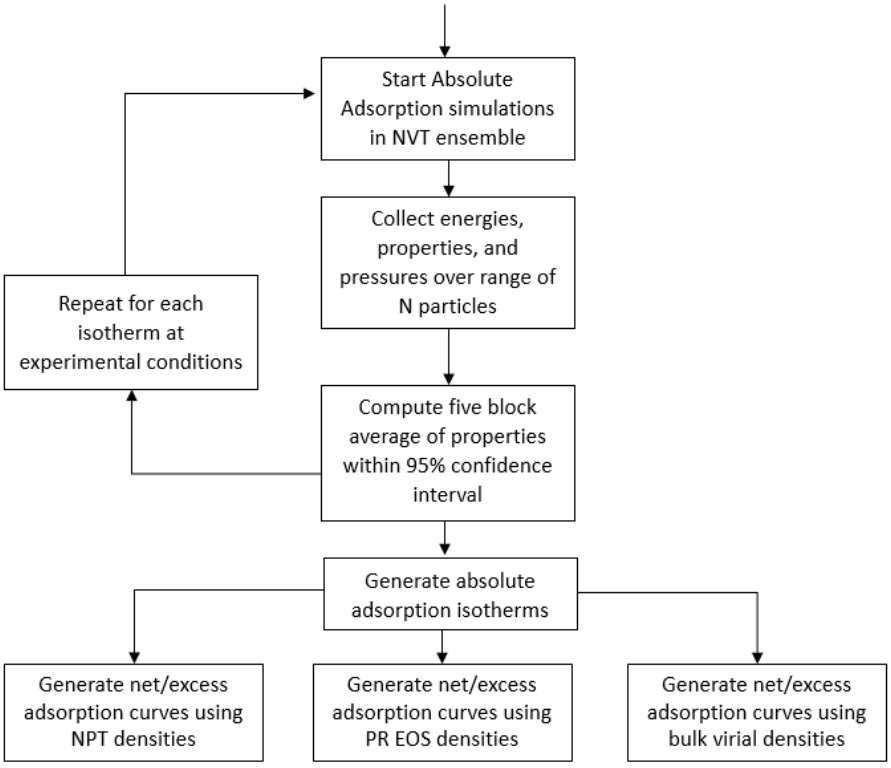

Figure 4.1: Flowchart for Computational Procedure

the surface area conversion ([2]) provide the key link to connect results from simulation to experimental data in the canonical ensemble for shale gas adsorption at high pressures.

4.4.2 Adsorption Monte Carlo Simulations

Confined NVT simulations using version 2 of the Monte Carlo and Molecular Dynamics software (RASPA) by Dubbeldam et al. [9] were used to determine absolute adsorption curves at the same temperatures (i.e., 35.4, 50.4, 60.0, and 65.4 ˚C) reported in the experimental work of Fan et al. [15] at increasing pressures. All Monte Carlo computations were performed on three custom-built computers with AMD 1090T 3.2 GHz and AMD FX8300 processors in double precision arithmetic using the GNU compiler. Periodic boundary conditions were employed with a cut off radius of 12 Å.

The framework used for the NVT simulations is shown in Fig. 4.2 and is a graphite nanochannel used to represent the adsorbent material consisting of 3776 atoms. Specifications for the absorbent can be found in Table 4.1 [18].

Table 4.1: Framework Specifications

Pore Throat (Å)	**Free Dimension (Å)**	**Sheet-sheet distance (Å)**	**Volume ($Å^3$)**
5.363	10.727	14.2	71,428.95

*specifications taken from the supporting information of Dubbeldam et al. [18]

The United Atom TraPPE force field was used for methane. The Lennard-Jones United Atom TraPPE force field was used to model methane [19]. Helium reference state simulations Lennard-Jones parameters from Bolboli Nojini et al. [20]. Parameters for the adsorbates are given in Table 4.2. Framework parameters can be found in Dubbeldam et al. [18].

Table 4.2: Forcefield Parameters

#	type	ε/k_B [K]	σ [Å]
1	CH_4	148.0	3.730
2	He	19.38	2.67

Tail cut off corrections are generally used to estimate molecular interactions at very large distances with no walls; however they are not applicable for confinement. Simulations were started with two unit cells: one containing an empty framework and the other containing a number of methane molecules on the outside of the slit pore on the outside of the pore throat. Since the United Atom TraPPE force field was used for methane, there was no need for rotation moves. Instead, a short Monte Carlo pre-equilibration step was run for 10,000 steps with 100 % translation frequency and a Molecular Dynamics step every 10 steps was employed to promote equilibration (see [21]). Only Monte Carlo translation moves were performed for 400,000 equilibration and production Monte Carlo cycles. The reported number of particles (N) was determined using a five block average thereby giving a 95% confidence interval. Once equilibrium (and adsorption) was achieved between the outer methane particles and those in the slit pore space, the bulk pressure was determined by using the standard virial pressure applied only to the bulk methane particles outside the framework [22], [23].

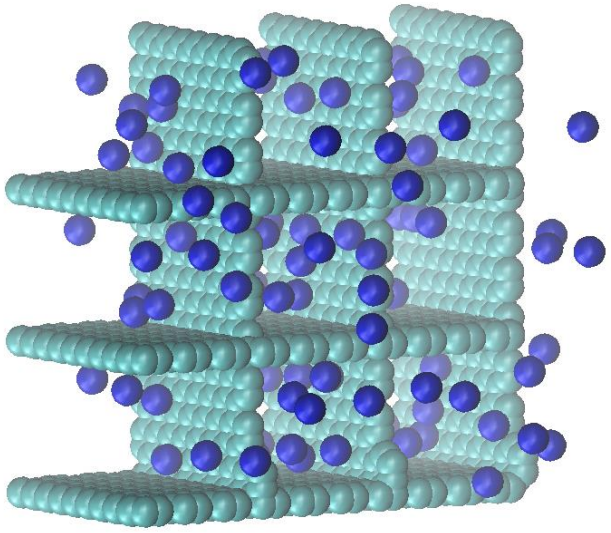

Figure 4.2: Example snapshot of methane in equilibrium with graphite slit pore (2.7 bar, 303.15 K)

Thermodynamic equilibrium in the NVT ensemble was satisfied by using periodic boundary conditions in the directions of the pore throat and by placing additional atoms on the outside of the framework to provide equilibrium between the particle in the bulk and in the confined space. Since flexibility is not a strict requirement for thermodynamic equilibrium [24], a rigid framework was used to simulate small nano-pores representing conditions in a shale gas reservoir.

4.4.3 Isothermal-Isobaric Ensemble (NPT)

In order to compute the bulk density of methane, NPT simulations were performed with 500 methane particles and runs were set to 400,000 equilibration and production Monte Carlo cycles. A radial cut off distance of 12 Å was used with tail cut off corrections applied. The frequencies for translation and volume moves were each set to 50%. Further simulation details can be found in Allen and Tildesley [23] and

previously applied for different systems (e.g. water, hexane, CO_2) [25]. Forcefield information can be found in Table 4.2.

4.4.4 Density Computations

Since the conversion of absolute to excess adsorption in Eq. 4.1 requires accurate bulk fluid densities (ρ_b), a very brief background of the Peng Robinson equation of state is warranted for readers' not familiar with equations of states [13]. Furthermore, in this work, PR EOS predicted methane densities are compared to the Setzmann & Wagner [17], NVT, and NPT bulk densities that help define a benchmark for bulk methane densities at high pressures. The PR EOS is a semi empirical EOS that expresses pressure as the summation of a repulsion ($P_R = \frac{RT}{v-b}$) and attraction ($P_A = -\frac{a(T)}{g(v)}$) term where g(v) is function of a molar volume (v), b is the molecular co-volume representing the closest packed structure, and a(T) is a measurement of the intermolecular attraction forces. The PR expression for $P = P_R + P_A$ can be found in Eq. 4.4.

$$P = \frac{RT}{v-b} - \frac{\alpha a(T)}{v(v+b)+b(v-b)} \tag{4.4}$$

$$Z^3 - (1-B)Z^2 + (A - 3B^2 - 2B)Z - (AB - B^2 - B^3) = 0 \tag{4.5}$$

Eq. 4.4 can be rewritten in terms of the compressibility factor $Z = PV/(RT)$ with Eqns. 4.6-4.8:

$$A = \frac{aP}{R^2T^2} \tag{4.6}$$

$$B = \frac{bP}{RT} \tag{4.7}$$

$$Z = \frac{Pv}{RT} \tag{4.8}$$

Eqns. 4.9 and 4.10 can then be obtained by applying Eqn. 4.4 at the critical point.

$$a = \frac{0.45724R^2T_C^2}{p_c} \tag{4.9}$$

$$b = \frac{0.07780RT_c}{p_C} \tag{4.10}$$

The remaining Eqns. 4.11-4.13 are used at temperatures other than the critical temperature for the desired molecule.

$$\alpha = \left(1 + \kappa(1 - T_r^{0.5})\right)^2 \tag{4.11}$$

$$\kappa = 0.37464 + 1.54226\omega - 0.26992\omega^2 \tag{4.12}$$

$$T_r = \frac{T}{T_c} \tag{4.13}$$

A complete derivation that includes fugacity, mixture expressions, and enthalpy departure functions can be found in Peng and Robinson [13]. The methane parameters used in this work are ω = 0.0115, T_c= 191.15 K, $P_c = 4.641$ MPa. Finally, PR EOS predicted methane densities were compared to the empirical EOS by Setzmann & Wagner [17] reported in the NIST Chemistry Web Book, densities corresponding to the virial pressure, and NPT bulk densities.

4.4.5 Free Volume and Surface Area Computations

The free volume of the graphite nano-channel was determined using Eq. 4.2 which requires only particle insertion moves with the desired probing molecule to estimate the second virial coefficient [1]. Since the free volume is dependent on the geometry

of the pore structure, it is not a function of pressure. However, the procedure must be performed at experimental temperature conditions to maintain a consistent reference point. Free volumes for methane and helium at a reference temperature of 298 K were determined. The void fraction of the slit pore (i.e., the empty space divided by the total volume) was estimated by particle insertions [21].

Surface area was computed using an auxiliary method provided by Dubbeldam [21]. The surface area computation consisted of rolling a probing molecules (e.g. nitrogen, helium, argon, etc) over the desired framework. Each framework atom location was assigned atom points that generate a sphere around individual framework atoms where the amount of overlap is computed. The probing atom was then rolled onto the surface of the framework atoms and the corresponding overlap was computed for the framework – probing molecule interactions. Finally, the fraction of overlap was multiplied by the area of the sphere resulting in the geometric surface area. Since the focus of this paper is on current methods for comparing simulation adsorption results to experimental data, the reader is referred to Connolly [26] for a rigorous description of this method for determining surface area.

4.5 Results and Discussion

In this section, the presented results demonstrate the estimations of bulk methane densities in 4.6. Use of a bulk fluid reference is described in section 4.6.1. An over estimation is shown when only considering the volume of the adsorbent in section 4.6.2. This result can be normalized leading to a more reasonable comparison when compared to experimental data as shown in section 4.6.3. Lastly, the impact of pore

free volume dependent on probing molecules is presented in section 4.6.4. Part of the discussion will address potential pitfalls and tradeoffs when using conventional techniques as well as methods that are more modern. Finally, we discuss the implications of using a new direct approach in the in the NVT ensemble which can be used with similar success upon comparison to experimental data.

4.5.1 Accurate bulk fluid methane densities in the shale gas high pressure regime

In order to compute adsorption at high-pressures, excess (Eq. 4.1) and net (Eq. 4.3) adsorption are used to convert simulation to experimental data requiring accurate bulk fluid densities (ρ_b). The excess and net adsorption in the proposed NVT ensemble in section 4.5 requires accurate methane densities that can be computed by ***indirect computations*** (1) NPT simulations, (2) Peng-Robinson EOS or ***direct computation*** (1) using the virial pressure places on the molecules outside of the slit pore as shown in this work.

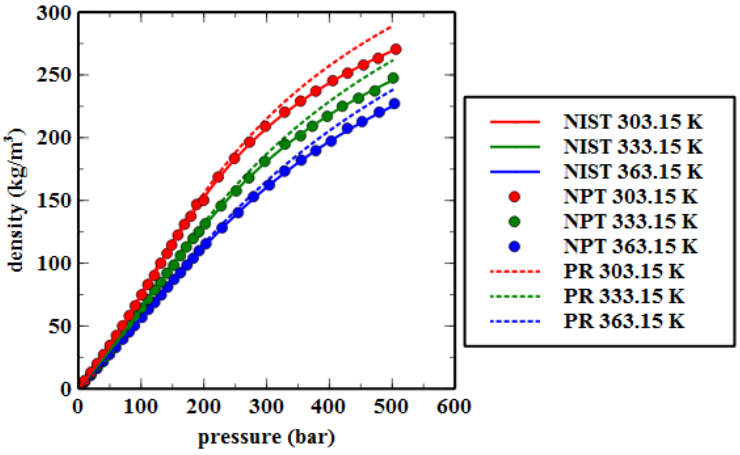

Figure 4.3: Comparison of indirect methods for methane bulk densities to reported data [17]

In Fig. 4.3, we can see that there is an excellent match for the NPT Monte Carlo simulations when compared to data from Setzmann and Wagner [17] for three adsorption isotherms (303.15, 333.15, 363.15 K) found at experimental conditions of Fan et al. [15]. The bulk NIST methane densities data are considered the benchmark results in this study with uncertainties of 0.03% below 12 MPa and up to 0.07 % for pressures less than 50 MPa [17] Again, accurate bulk fluid methane densities are crucial for Eq. 4.1 and 4.3 when converting to the respective excess and net adsorption thermodynamic frameworks.

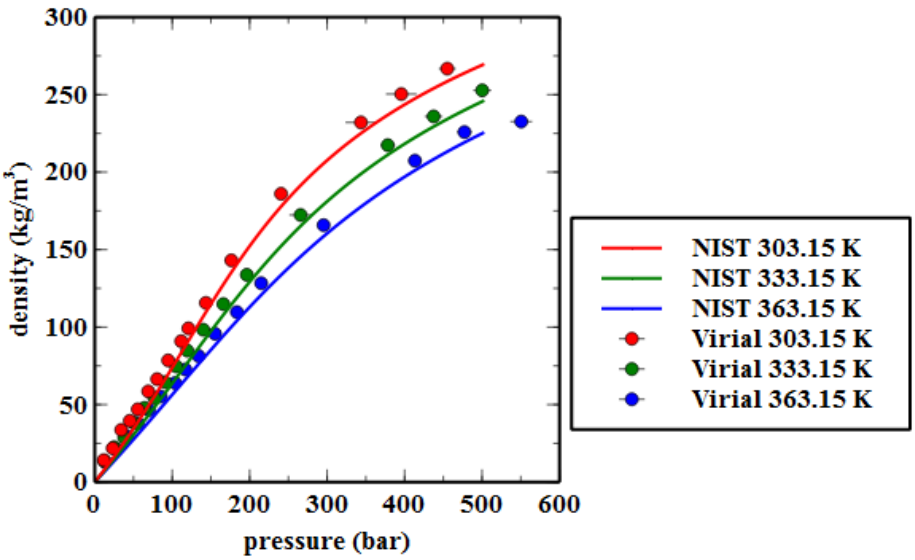

Figure 4.4: Comparison of direct method for methane bulk densities to NIST

The remaining EOS density computations results were run over the same isotherms and pressure range (1 – 500 bar). It is clear from Fig. 4.3. that the computed NPT methane densities have an excellent agreement with NIST densities with overall standard deviations of less than 0.5 %. Not surprisingly, the PR EOS over predicts ρ_g at high pressures with an average percent error of 3.31, 3.11, and 3.57 % for isotherms

at 303.15, 333.15, 363.15 K, respectively. While an indirect PR approach is computational faster, care must be taken to ensure the results are accurate at high pressures.

We have demonstrated the ability to indirectly compute the bulk fluid densities using a Monte Carlo and EOS approach as seen in Fig. 4.3. If a direct approach is desired in order to avoid the need for additional simulations, the virial pressure approach can be used on molecules in equilibrium with the slit pore. The results of the direct approach are demonstrated in Fig. 4.4. The takeaway from this section is that this density coupled the bulk viral pressure can be used as a means of direct measurement of bulk density for Eqns. 4.1 & 4.3. To the author's knowledge, this method of direct computation is sparsely reported in the literature [27]. Now as with all techniques, there are advantages and disadvantages. The advantage is that the density can be directly estimated which saves computational time, this approach can be quite useful as geometric complexity of the framework is increased. However, the drawback is that the virial pressure that corresponds to the bulk pressure has error associated with it. Fortunately, our previous work shows that if a multi-scale approach is desired, we can use the Gibbs-Helmholtz constrained EOS in this case. Specifically, if bubble point reduction estimations are desired, a sensitivity to a 5% uncertainty of confined fluid molar volume is less than 1% [12]. Since this drawback has been previous investigated and quantified, we focus on the adsorption aspect of confined fluids. In this work, we focus on the direct and indirect methods to compute bulk densities in the NVT ensemble and compare their impact on excess and net adsorption to experimental data (e.g. PR EOS, NPT ensemble, etc).

4.5.2 Comparison of excess and net adsorption to experimental data using conventional approach with NPT computed densities

Since simulation work employs smaller pore wall thickness than experimental conditions there will most likely be a larger specific surface area up to a few orders of magnitude at high pressures ([2], [28]). The same key concept holds true for this work and provides an explanation for the large differences between the simulation and experimental conditions found in Fig. 4.5. The excess and net NPT adsorption curves in Fig. 4.5 are the benchmark for comparison purposes due to the accuracy of the NPT Monte Carlo methane densities as observed in Fig 4.3. Also, it should be noted that the net adsorption should be markedly lower than excess adsorption because the entire volume of the system is subtracted from the absolution adsorption contribution (see Eq. 4.3). On the contrast, the excess adsorption is typically higher than net adsorption at very high pressures in the supercritical region for light gases [14]. This is due to the lower amount of slit pore volume that is considered for excess adsorption (see Eq. 4.1). The reference pore volumes for the net and excess conversions can be found in Table 4.3.

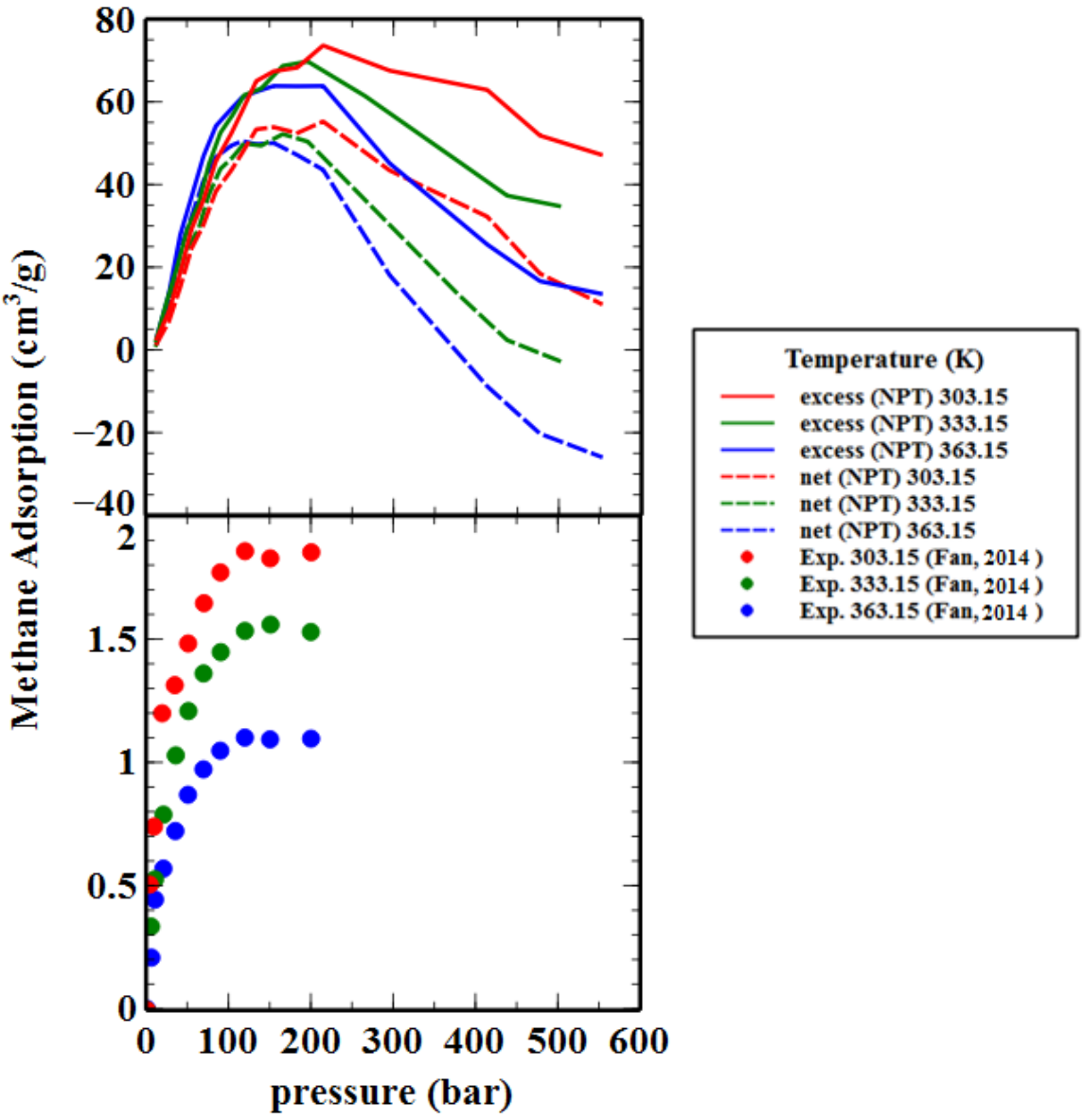

Figure 4.5: Excess and Net adsorption isotherms compared to experimental data [15]

There is also debate in the literature concerning the negative adsorption for net adsorption conversion. As made clear in the literature the net adsorption terminology in the adsorption conversion literature lead to considerable confusion on the subject [1]. They further state that several thermodynamic properties such as departure

functions are negative and still considered rigorous. Therefore, the assertion that the net adsorption should never be negative is incorrect [1]. An example of a negative net adsorption can be seen in Fig. 5 of Gumma and Talu [1] which compares absolute, excess, and net adsorption for methane on Norit R1 Extra at 298 K.

4.5.3 Surface area approach for linking excess and net adsorption curves

The intent here is to consider the surface area of both the simulation unit cell and experimental sample. Coupling the surface area information provides the thermodynamic community a link between the two methods in the NVT ensemble. Fig. 4.5 demonstrates that there is a mismatch between current simulation techniques and experimental data. Here in this section, we demonstrate that by normalizing the data of Fan et al. [15] using the SSA technique proposed by Chen et al. [2] for the Grand Canonical ensemble a more reasonable comparison can be drawn. We reiterate that this technique has already been employed in the literature for a GCMC ensemble in a similar manner. To the author's knowledge, it has not been performed for the NVT ensemble or for a slit pore model. Once the SSA is taken into account, the simulation and experimental data can then be compared. The direct and indirect approaches in Figs. 4.6 & 4.7 show variability between the application adsorption due to the viral pressure, NPT, and PR estimated densities. While the SSA method greatly helps when comparing the results, a disadvantage is the lack of SSA data provided by the experimentalist and the inability to characterize the SSA uniformity throughout the reservoir. In the case of Fan et al. [15], the SSA is not explicitly provided which is troublesome as now experimental SSA values must be obtained elsewhere. To further

complicate the issue, if Fig. 5d is inspected in Tian et al. [29] it should be apparent that there is a distribution of SSA for a given sample and it depends where the pore throats are located. As such we reference Cao et al. [16] who state that the surface area of Silurian Longmaxi Formation shales is in the range of 17.83-29.49 m^2/g. This range for the experimental data is reflected in Figs. 4.6 -4.10 with a minimum and maximum range for the excess and net adsorption isotherms. The simulation results for Figs. 4.6 & 4.7 are given up to 550 bar far beyond the maximum reported pressure given by Fan et al. [15] reported up to 200 bar. The simulation results show a qualitative agreement corresponding to the maximum Longmaxi SSA and are more acceptable than results reported in Fig. 4.5 that only consider the pore volume. Since there is a non-uniform SSA distribution for field conditions, the agreement with simulation results can be found in the upper and lower SSA range for the 363.15 K adsorption curves [15]. From inspection, there is better agreement with NPT excess adsorption curves with experimental data [15]. On the contrary, the PR EOS over predicts bulk methane densities at high pressures a further decrease in adsorption as expected. Furthermore, the excess adsorption curves capture a reasonable trend beyond the experimental pressure range.

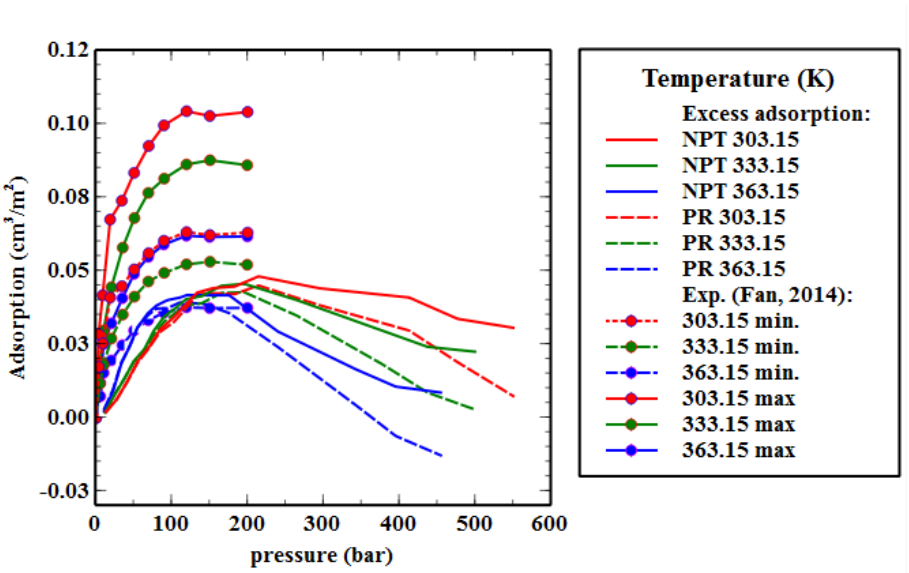

Figure 4.6: Comparison of excess adsorption isotherms to experimental data with NPT and PR EOS computed methane densities [15]

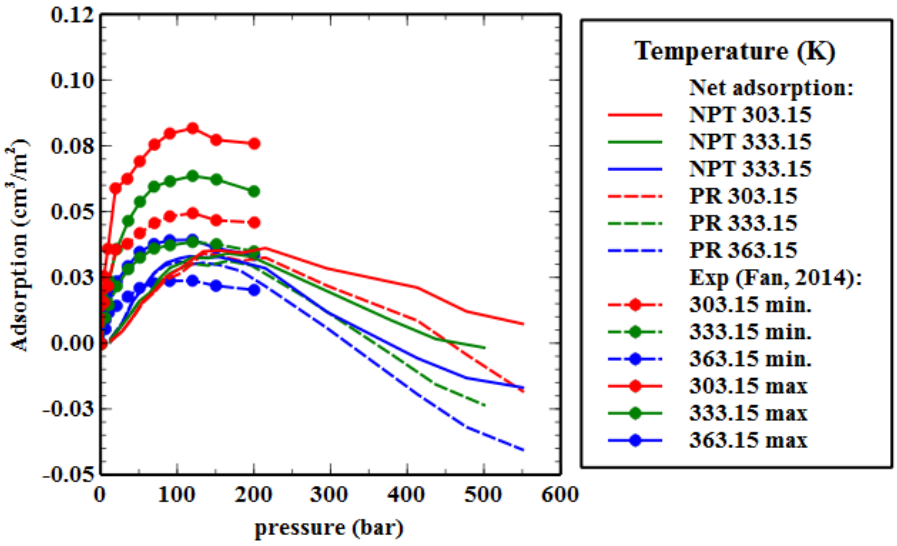

Figure 4.7: Comparison of net adsorption isotherms to experimental data with NPT and PR EOS computed methane densities [15]

The net adsorption NPT results in Fig. 4.7 are in better agreement with the experimental data than excess results in Fig. 4.6 since adsorbed methane is in the

supercritical regime. This is of course due to the reference state in Eq. 4.3 that subtracts off the entire system volume. While negative net adsorption results at high pressures are valid experimental results do not appear to become negative when extrapolated. The experimental adsorption curves can be converted by utilizing the entire volume of the sample crucible when occupied by helium. In this work the volume of the crucible for the Gravimetric Sorption Analyzer (ISOSORP – GAS SC) identical to the instrument used in Fan et al. [15] is referenced.

It is interesting to observe that the simulation estimates tend to favor the upper range of SSA for Silurian Longmaxi type shales. This may be due to the maturity of the shale sample, extent of kerogen content, or the composition of clay minerals such as quartz, pyrite, dolomite, feldspar, etc. Another possibility is the inability for simulation to capture defects found at field conditions since periodic boundary conditions ensure a repeated unit cell granular defects.

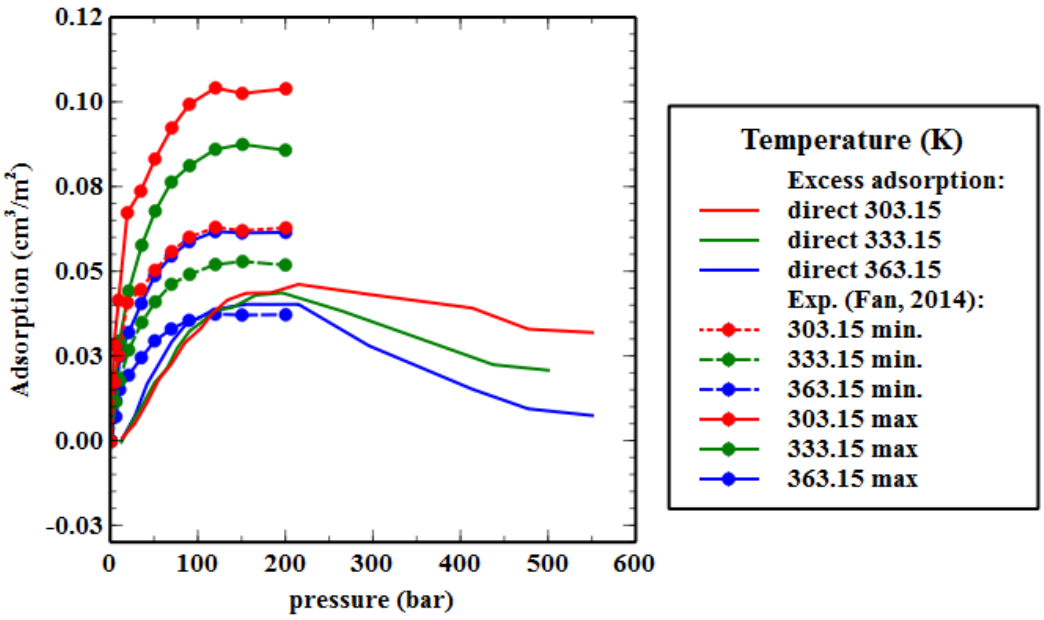

Figure 4.8: Direct computation of excess adsorption using virial pressure on methane molecules located outside the slit pore [15].

We have defined the benchmark calculations using the net and excess adsorption curves for the indirect approaches (PR EOS and NPT ensemble) as shown in Figs. 4.6 & 4.7. A direct approach can be utilized if the computational resources are limited by using the viral pressure. However, it is well known that there is error associated with the viral pressure (see Fig. 4.3 for density comparisons). This error in pressure can be seen in Fig. 4.4 at high pressures above 300 bar. There is error at lower pressures but they are not visible due to the size of the data markers.

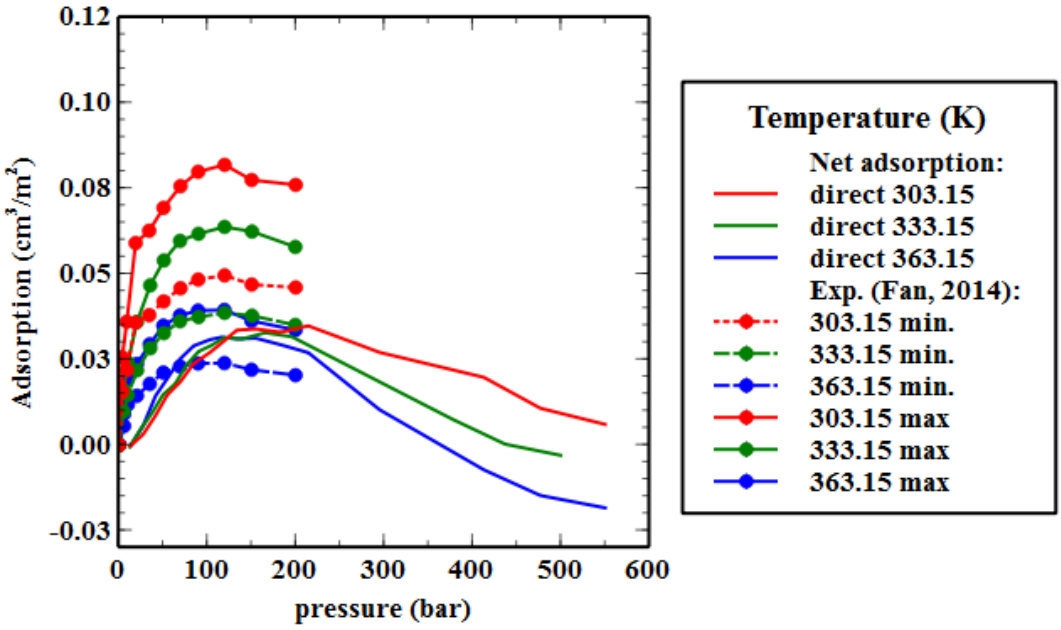

Figure 4.9: Direct computation of net adsorption using virial pressure on methane molecules located outside the slit pore [15].

The following can be determined from Figs. 4.8 & 4.9:

1) The direct estimation of the bulk pressure on the outside portion of the slit pore leads to comparable excess and net adsorption profile curves.
2) Net adsorption appears to provide a more reasonable comparison to experimental data in the minimum SSA and lower temperature region.
3) This method should only be employed if a direct measurement is desired. A more precise estimation is the report NPT net adsorption results found in Fig. 4.7.

4.5.4 Impact of pore free volume between methane and helium molecules

In this section, the impact of assessable pore volume methane and helium probe molecules is explored. The procedure for determining assessable pore volume is

presented in section 4.5.3. Since there is minimal impact of pore volume, we only present the benchmark NPT pressure method example thereby avoiding redundancy. Pore volume occupancy information at room temperature is given in Table 4.3 where the total volume of a unit cell of a 1.42 nm graphite nanochannel pore throat is 71.428 nm^3, methane at 66.31 nm^3, and helium at 66.42 nm^3. It is expected that helium pore volume is greater than methane due to the fact that helium is smaller than methane. Another example of the difference in accessible pore volume can be seen in Table 1 of Chen et al. [2] which in their case leads to a noticeable difference in adsorption due to their choice of framework namely Na-Montmorillonite.

Table 4.3: Volume of pore space occupied by molecules

Pore Size (nm)	Probing Molecule	Volume (nm^3)
1.42	**Methane**	**66.31**
1.42	**Helium**	**66.42**
	Total Volume	**71.428**

The difference between helium and methane probing molecules is observed in Fig. 4.10. Since there is minimal difference between the two molecules on excess adsorption, we recommend using helium as the probing molecule since it is standard practice for experimentalist [14].

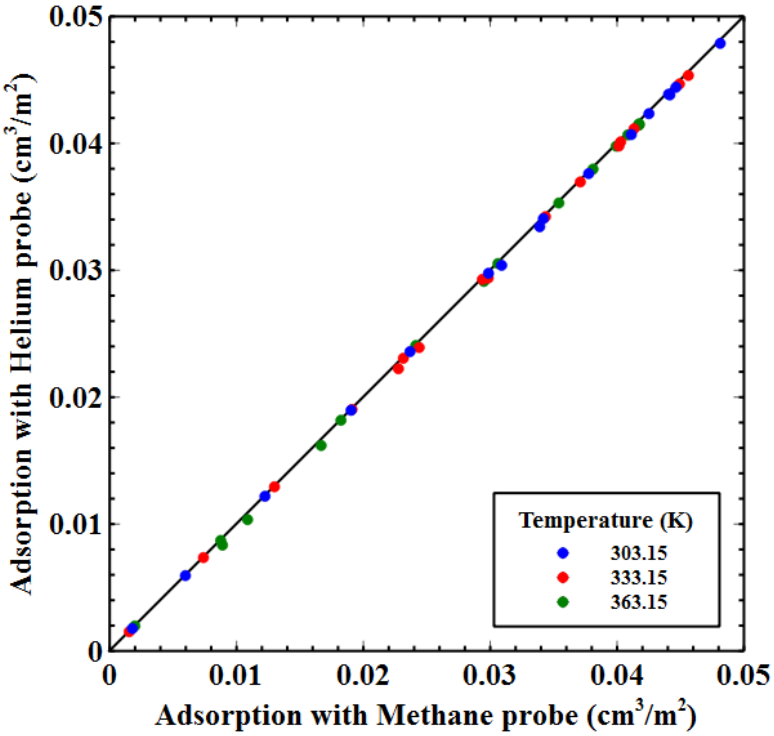

Figure 4.10: Effect of computed accessible methane and helium volume on NVT adsorption

4.6 Conclusion

In this work, we demonstrated the direct and indirect approaches that connect simulation to experimental results. Despite debate in the adsorption community between the usefulness between excess and net adsorption, the following should be considered when comparing simulation to experimental results in the Canonical ensemble:

- Direct measurement of the bulk densities can be estimated using the virial pressure on molecules located on the outside of the slit pore. This area

represents a pseudo-bulk pressure that is verified by comparing to the NPT ensemble.

- Indirect estimation of the bulk densities can be obtained using the NPT ensemble or PR EOS. NPT simulations must be performed in tandem and could be computationally prohibitive for larger molecules or more complicated framework interactions. The PR EOS overcomes the computational cost at an expensive of providing over-predictions of densities for methane at high pressure. If used a high pressures, careful selection and verification of bulk fluid parameters are warranted.
- There is a noticeable difference between excess and net adsorption results when only considering the volume of the simulation unit cell and experimental sample as seen in Fig. 4.5.
- A surface area technique by Chen et al. [2] manages to normalize data thereby leading to comparisons between simulation and experimental data which are noticeably better. However, shale field conditions exhibit a range of SSA sizes that should be taken into consideration. Figs. 4.6 – 4.9 demonstrate the impact of a range in SSA sizes.
- In this case, a slit pore model, there is little difference between assessable pore volume determined by helium and methane probe moles. Fig. 4.10 demonstrates that the pore volume differences by probing molecules have minimal impact on excess and net adsorption results. This does not imply that adsorbate should not be used for the reference for porous media because in certain cases the selection of probing molecules must be considered (see the

Na-montmorillonite methane uptake case considered in Chen et al. [2]. For a different framework, the impact of utilizing the adsorbate for the probing molecule should be investigated prior to converting to excess or net adsorption.

4.7 Acknowledgement

This research did not receive any specific grant from funding agencies in the public, commercial, or not-for-profit sectors.

4.8 References

[1] S. Gumma and O. Talu, “Net adsorption: A thermodynamic framework for supercritical gas adsorption and storage in porous solids,” Langmuir, vol. 26, no. 22, pp. 17013–17023, 2010.

[2] G. Chen et al., “Keys to linking GCMC simulations and shale gas adsorption experiments,” Fuel, vol. 199, pp. 14–21, 2017.

[3] F. Aloulou and V. Zaretskaya, “Shale gas production drives world natural gas production growth,” U.S. Energy Information Administration, 2016. .

[4] D. Murali and F. Aloulou, “Future U.S. tight oil and shale gas production depends on resources, technology, markets - Today in Energy - U.S. Energy Information Administration (EIA),” U.S. Energy Information Administration, 2016. [Online]. Available: https://www.eia.gov/todayinenergy/detail.php?id=27612. [Accessed: 16-Jun-2017].

[5] L. Ji, T. Zhang, K. L. Milliken, J. Qu, and X. Zhang, “Experimental investigation of main controls to methane adsorption in clay-rich rocks,” Appl. Geochemistry, vol. 27, no. 12, pp. 2533–2545, 2012.

[6] A. Orangi, N. R. Nagarajan, M. M. Honarpour, and J. J. Rosenzweig, “Unconventional Shale Oil and Gas-Condensate Reservoir Production, Impact of Rock, Fluid, and Hydraulic Fractures,” SPE Hydraul. Fract. Technol. Conf., pp. 1–15, Apr. 2013.

[7] D. Nicholson and N. Quirke, Adsorption and Transport at the Nanoscale. New York: Taylor & Francis, 2005.

[8] L. MacGillivrary and N. . Hoboken, Metal-organic frameworks : design and application. Hoboken, N.J.: Wiley, 2010.

[9] D. Dubbeldam, S. Calero, D. E. Ellis, and R. Q. Snurr, “RASPA: molecular simulation software for adsorption and diffusion in flexible nanoporous materials,” Mol. Simul., vol. 42, no. 2, pp. 81–101, 2016.

[10] P. Kowalczyk, H. Tanaka, K. Kaneko, A. P. Terzyk, and D. D. Do, “Grand

canonical Monte Carlo simulation study of methane adsorption at an open graphite surface and in slitlike carbon pores at 273 K," Langmuir, vol. 21, no. 12, pp. 5639–5646, 2005.

[11] A. Poursaeidesfahani, A. Torres-Knoop, M. Rigutto, N. Nair, D. Dubbeldam, and T. J. H. Vlugt, "Computation of the Heat and Entropy of Adsorption in Proximity of Inflection Points," J. Phys. Chem. C, vol. 120, no. 3, pp. 1727–1738, 2016.

[12] E. Thomas and A. Lucia, "Multi-scale equation of state computations for confined fluids," Comput. Chem. Eng., pp. 1–10, 2017.

[13] D.-Y. Peng and D. B. Robinson, "A New Two-Constant Equation of State," Ind. Eng. Chem. Fundam., vol. 15, no. 1, pp. 59–64, 1976.

[14] A. L. Myers and P. A. Monson, "Adsorption As the Basis for Thermodynamic Analysis," Adsorption, vol. 20.4, pp. 591–622, 2014.

[15] E. Fan, S. Tang, C. Zhang, Q. Guo, and C. Sun, "Methane sorption capacity of organics and clays in high-over matured shale-gas systems," Energy, Explor. Exploit., vol. 32, no. 6, pp. 927–942, 2014.

[16] T. Cao, Z. Song, S. Wang, and J. Xia, "A comparative study of the specific surface area and pore structure of different shales and their kerogens," Sci. China Earth Sci., vol. 58, no. 4, pp. 510–522, 2015.

[17] U. Setzmann and W. Wagner, A New Equation of State and Tables of Thermodynamic Properties for Methane Covering the Range from the Melting Line to 625 K at Pressures up to 1000 MPa. J. Phys. Chem. Ref. Data, 1991.

[18] D. Dubbeldam, R. Krishna, S. Calero, and A. Ö. Yazaydın, "Computer-Assisted Screening of Ordered Crystalline Nanoporous Adsorbents for Separation of Alkane Isomers," Angew. Chemie - Int. Ed., vol. 51, no. 47, pp. 11867–11871, 2012.

[19] M. G. Martin, "MCCCS Towhee: a tool for Monte Carlo molecular simulation," Mol. Simulat, vol. 39, pp. 1212–1222, 2013.

[20] Z. Bolboli Nojini, A. Abbas Rafati, S. Majid Hashemianzadeh, and S. Samiee, "Predicting helium and neon adsorption and separation on carbon nanotubes by Monte Carlo simulation," J. Mol. Model., vol. 17, no. 4, pp. 785–794, 2011.

[21] D. Dubbeldam, "RASPA 1 . 9 . 15 : Molecular Software Package for Adsorption and Diffusion in (Flexible) Nanoporous Materials," pp. 1–145, 2014.

[22] K. E. Gubbins, Y. Long, and M. Śliwinska-Bartkowiak, "Thermodynamics of confined nano-phases," J. Chem. Thermodyn., vol. 74, pp. 169–183, Jul. 2014.

[23] M. P. Allen and D. J. Tildesley, Computer simulation of liquids. Oxford university press, 1989.

[24] D. Dubbeldam, A. Torres-Knoop, and K. S. Walton, “On the inner workings of Monte Carlo codes,” Molecular Simulation, vol. 39, no. 14–15. Taylor & Francis, pp. 1253–1292, 2013.

[25] A. Lucia, “A MultiScale Gibbs-Helmholtz Constrained Cubic Equation of State,” J. Thermodyn., vol. 2010, pp. 1–10, 2010.

[26] M. L. Connolly, “The molecular surface package,” J. Mol. Graph., vol. 11, no. 2, pp. 139–141, 1993.

[27] A. Wongkoblap, S. Junpirom, and D. D. Do, “Adsorption of Lennard-Jones Fluids in Carbon Slit Pores of a Finite Length. A Computer Simulation Study,” Adsorpt. Sci. Technol., vol. 23, no. 1, pp. 1–18, 2009.

[28] J. Zhang, M. B. Clennell, K. Liu, M. Pervukhina, G. Chen, and D. N. Dewhurst, “Methane and Carbon Dioxide Adsorption on Illite,” Energy & Fuels, vol. 30, no. 12, pp. 10643–10652, 2016.

[29] H. Tian, L. Pan, X. Xiao, R. W. T. Wilkins, Z. Meng, and B. Huang, “A preliminary study on the pore characterization of Lower Silurian black shales in the Chuandong Thrust Fold Belt, southwestern China using low pressure N2 adsorption and FE-SEM methods,” Mar. Pet. Geol., vol. 48, pp. 8–19, 2013.

4.9 Nomenclature

A	represents intermolecular attraction forces
b	molecular co-volume
k	boltzmann constant
M	mass
n	pure component adsorbate isotherm
N	number of particles

N_{ab}	Avogadro's Number
P	pressure
R	universal gas constant
T	temperature
U	internal energy
v	molar mass
V	volume
Z	compressibility factor

Greek

α	scaling factor
κ	characteristic constant
ϕ	interactions between adsorbate and surface
ρ	bulk fluid density
w	acentric factor

Subscripts/Superscripts

A	attraction

ab	denotes an adsorption function
c	critical
ex	excess adsorption
g	denotes gas phase
i	i^{th} component
net	net adsorption
p	pore
R	repulsion
r	reduced property
s	surface of the framework

5 CONCLUSION

Understanding thermodynamic behavior of nanoporous materials using a slit pore representation at shale gas reservoir conditions provides meaningful insight for the scientific community. While there are limited models in the literature, there are many simulations techniques that can be utilized to explore shale gas systems. In this dissertation, a hybrid approach that employs a combination of simulation and modeling proves to be effective at defining high pressure adsorption behavior.

Pure component information is investigated and then mixed using a simple linear mixing rule yielding a computationally tractable framework for the prediction of mixture phenomena. The proposed methodology consists of validating the linear mixing rule with pure component and mixture simulations. Although the linear mixing rule has some inherent error when validated, a sensitivity analysis shows a minimal impact upon being up-scaled to the bulk scale.

Since the linear mixing rule held, the adsorption phenomena over typical reservoir temperature and pressure ranges were investigated. Internal energies of departure and adsorption isotherms for n-alkanes were shown to exhibit dependence on an increase of carbon-chain length. To extend the pure component library to mixtures, Ideal Adsorption Solution Theory was shown effective at the prediction of mixed-gas adsorption. Establishing a benchmark for comparison, a ternary mixture prediction was compared to similar simulation results.

Key links were investigated between simulation and experimental data through a rigorous means. The experimental and simulation data must be converted using a combination of simulation and experimental techniques. Once converted, surface area data of the nanoporous material is used to normalize the data with exceptional results. The estimation of void pockets of the porous material was shown to have a minimal dependence on the specific probing molecule used in this work.

A framework for bridging molecular information to the bulk scale is provided through simulation and modeling. This work provides a template for further molecular study of slit pores as well as meaningful information for research that seeks to capture molecular information on the bulk scale.

6 APPENDICES

6.1 Appendix for Equation of State Computations for Confined Fluids

6.1.1 Pure Component Internal Energy of Departure for Confinement

All internal energies of departure in Appendices 6.1.1-6 are in units of cm^3bar/mol and the numbers in parentheses correspond to standard deviations.

Table 6.1: Force field, NVT Ensemble Average, and Reference Internal Energy

Species	**Force field**	**N**	**T(K)**	**p (bar)**	**+/- p (bar)**	$\langle U_i^D(T,V)\rangle$	$\langle U_i^\circ(T,V)\rangle$
methane	TraPPE-UA	64.34	300	200	3.40	-5.0715×10^3 (3.01×10^2)	n/a
methane	TraPPE-UA	61.74	300	100	2.16	-4.7641×10^3 (4.86×10^2)	n/a
n-octane	TraPPE-UA	26.46	300	200	28.28	-2.7448×10^5 (1.03×10^3)	2.4558×10^5
n-octane	TraPPE-UA	25.21	400	100	12.79	-3.6515×10^5 (5.12×10^3)	3.3990×10^5
water	TIP4P-Ew	43.10	290	60	2.95	-3.9442×10^4 (3.15×10^2)	n/a
n-hexane	TraPPE-UA	24.57	290	60	5.651	-1.7624×10^5 (2.61×10^3)	1.6012×10^5
n-hexane	TraPPE-UA	56.79	300	80	7.19	-1.6739×10^5) (3.17×10^3)	1.6459×10^5
propane	TraPPE-UA	49.59	300	100	2.58	-5.4332×10^4 (2.46×10^2)	3.9845×10^4
propane	TraPPE-UA	56.67	300	80	0.76	-5.6981×10^4 (3.37×10^1)	3.9845×10^4
CO_2	TraPPE	42.59	300	80	2.58	$-5.8\ 768\times10^3$ (4.15×10^2)	n/a

6.1.2 Pure Component Unconfined Internal Energy of Departure with and without Analytical Tail Cutoff Corrections

Table 6.2: Species, Force field, NPT Ensemble Average, and Reference Internal Energy

Species	**Force field**	**N**	**p**	**T**	$\langle U_i^D(T,P)\rangle^a$	$\langle U_i^D(T,P)\rangle^b$
methane	TraPPE-UA	64	200	300	-1.2209×10^4 (1.05×10^2)	-2.3005×10^4 (7.40×10^1)
octane	TraPPE-UA	64	200	300	-1.9125×10^5 (1.48×10^3)	-3.6957×10^5 (5.85×10^3)
water	TIP4P-Ew	64	60	290	-3.9816×10^5 (7.26×10^3)	-4.7103×10^5 (9.23×10^3)
hexane	TraPPE-UA	64	60	290	-1.2401×10^5 (2.08×10^3)	-2.7681×10^5 (2.61×10^3)
methane	TraPPE-UA	64	100	300	-6.5428×10^3 (6.63×10^1)	-1.1606×10^4 (2.53×10^2)
propane	TraPPE-UA	64	100	300	-3.7003×10^4 (1.16×10^3)	-1.3036×10^5 (1.97×10^3)
propane	TraPPE-UA	64	80	300	-3.7261×10^4 (1.58×10^3)	-1.3444×10^5 (8.29×10^2)
CO_2	TraPPE	64	80	300	-1.8499×10^4 (2.57×10^3)	-8.3063×10^4 (1.05×10^4)
hexane	TraPPE-UA	64	80	300	-1.4418×10^5 (4.98×10^3)	-2.7016×10^5 (1.34×10^3)

[a] no tail cutoff corrections included
[b] tail cutoff corrections included

6.1.3 Pure component fluid properties

Table 6.3 Pure Component Fluid Properties

Species	**T_c (K)**	**P_c (bar)**	**b (cm^3/mol)**
methane	190.58	45.92	29.61
octane	568.83	24.86	143.15
water	647.37	221.20	16.36
hexane	507.60	30.20	110.31
propane	369.82	42.47	60.40
CO_2	304.12	73.77	29.16

6.1.4 Comparison of U^D_M Using Linear Mixing Rule for Confined Mixtures without Analytical Tail Cutoff Corrections

Table 6.4: Comparison for Confined Mixtures of Methane/Octane[a]

x_{CH4}	$\langle U_M^D(T,V)\rangle$	$\sum_{i=1}^{c} x_i\langle U_i^D(T,V)\rangle$	**% Error**
0.20	-2.1488×10^5 (1.05×10^2)	-2.2037×10^5	2.49
0.50	-1.3177×10^5 (2.49×10^2)	-1.3920×10^5	5.34
0.70	-7.4690×10^4 (3.01×10^2)	-8.5092×10^4	12.22
		ADD	6.68

[a] N = 100, T= 300K, p =200 bar

Table 6.5: Comparison for Confined Mixtures of Water/Hexane[a]

x_{H2O}	$\langle U_M^D(T,V)\rangle$	$\sum_{i=1}^{c} x_i\langle U_i^D(T,V)\rangle$	% Error
0.25	-1.2962×10^5 (3.56×10^3)	-1.4204×10^5	8.75
0.50	-9.7049×10^4 (2.41×10^2)	-1.0784×10^5	10.01
0.75	-6.4299×10^4 (1.64×10^2)	-7.3643×10^4	12.69
		ADD	10.48

[a] N = 100, T= 290K, p =60 bar

Table 6.6: Comparison for Confined Mixtures of Methane/Propane[a]

x_{CH4}	$\langle U_M^D(T,V)\rangle$	$\sum_{i=1}^{c} x_i\langle U_i^D(T,V)\rangle$	% Error
0.25	-3.6458×10^4 (1.62×10^2)	-4.1940×10^4	13.07
0.50	-2.9548×10^4 (3.91×10^1)	-2.8854×10^4	2.35
0.75	-1.7156×10^4 (7.33×10^1)	-1.6332×10^4	4.80
		ADD	6.74

[a] N = 100, T= 300K, p =100 bar

Table 6.7: Comparison for Confined Mixtures of CO_2/Hexane[a]

x_{CO2}	$\langle U_M^D(T,V)\rangle$	$\sum_{i=1}^{c} x_i\langle U_i^D(T,V)\rangle$	% Error
0.25	-1.33724×10^5 (1.95×10^2)	-1.27016×10^5	5.28
0.50	-9.64554×10^4 (1.67×10^2)	-8.66361×10^4	11.33
0.75	-5.35288×10^4 (4.40×10^2)	-4.62565×10^4	15.72
		ADD	10.78

[a] N = 100, T= 300K, p =80 bar

Table 6.8: Comparison for Confined Mixtures of CO_2/Propane[a]

x_{CO2}	$\langle U_M^D(T,V)\rangle$	$\sum_{i=1}^{c} x_i\langle U_i^D(T,V)\rangle$	% Error
0.25	-4.04788×10^4 (1.52×10^2)	-4.42051×10^4	8.43
0.50	-2.97013×10^4 (2.23×10^2)	-3.14290×10^4	5.50
0.75	-1.91238×10^4 (4.59×10^2)	$-1.\ 86530\times10^4$	2.52
		ADD	5.48

[a] N = 100, T= 300K, p = 80 bar

6.1.5 Comparison of U^{D}_{M} Using Linear Mixing Rule with Direct Monte Carlo Simulation for Unconfined Mixtures without Analytical Tail Cutoff Corrections[a,b]

Table 6.9: Comparison for Unconfined Mixtures of Methane/Octane[a]

x_{CH4}	$\langle U_M^D(T,P)\rangle$	$\sum_{i=1}^{c} x_i\langle U_i^D(T,P)\rangle$	**% Error**
0.20	-1.4105×10^5 (4.06×10^3)	-1.3944×10^5	1.1543
0.50	-9.0564×10^4 (2.14×10^3)	-9.1730×10^4	1.2704
0.70	-6.0867×10^4 (6.68×10^2)	-5.9921×10^4	1.5782
		ADD	1.33

[a] N = 100, T= 300K, p =200 bar

Table 6.10: Comparison for Unconfined Mixtures of Water/Hexane[a]

x_{H2O}	$\langle U_M^D(T,P)\rangle$	$\sum_{i=1}^{c} x_i\langle U_i^D(T,P)\rangle$	**% Error**
0.25	-2.0156×10^5 (1.35×10^4)	-1.9255×10^5	4.6806
0.50	-2.6590×10^5 (8.71×10^3)	-2.6109×10^5	1.8441
0.75	-3.1690×10^5 (5.45×10^3)	-3.2962×10^5	3.8599
		ADD	3.46

[a]N = 100, T= 300K, p =60 bar

Table 6.11: Comparison for Unconfined Mixtures of Methane/Propane[a]

x_{CH4}	$\langle U_M^D(T,P)\rangle$	$\sum_{i=1}^{c} x_i\langle U_i^D(T,P)\rangle$	% Error
0.25	-2.8778×10^4 (1.02×10^3)	-2.7122×10^4	6.1048
0.50	-1.9644×10^4 (2.65×10^2)	-2.0262×10^4	3.0503
0.75	-1.3146×10^4 (3.26×10^2)	-1.3402×10^4	1.9124
		ADD	3.69

[a]N = 100, T= 300K, p =100 bar

Table 6.12: Comparison for Unconfined Mixtures of CO_2/Hexane[a]

x_{CO2}	$\langle U_M^D(T,P)\rangle$	$\sum_{i=1}^{c} x_i\langle U_i^D(T,V)\rangle$	% Error
0.25	-1.1632×10^5 (3.10×10^3)	-1.1276×10^5	3.1554
0.50	-8.3918×10^4 (4.56×10^3)	-8.1340×10^4	3.1696
0.75	-4.9039×10^4 (2.38×10^3)	-4.9920×10^4	1.7648
		ADD	2.70

[a]N = 100, T= 300K, p =80 bar

Table 6.13: Comparison for Unconfined Mixtures of CO_2/Propane[a]

x_{CO2}	$\langle U_M^D(T,P)\rangle$	$\sum_{i=1}^{c} x_i\langle U_i^D(T,V)\rangle$	% Error
0.25	-3.3422×10^4 (1.01×10^2)	-3.2571×10^4	2.6129
0.50	-2.8644×10^4 (1.09×10^2)	-2.7880×10^4	2.7377
0.75	-2.3816×10^4 (8.60×10^2)	-2.3190×10^4	2.7016
		ADD	2.68

[a]N = 100, T= 300K, p =80 bar

6.1.6 Comparison of U^{D}_{M} Using Linear Mixing Rule with Direct Monte Carlo Simulation for Unconfined Mixtures with Analytical Tail Cutoff Corrections

Table 6.14: Comparison for Unconfined Mixtures of Methane/Octane[a]

x_{CH4}	$\langle U_M^D(T,P)\rangle$	$\sum_{i=1}^{c} x_i\langle U_i^D(T,P)\rangle$	% Error
0.20	-3.1063×10^5 (3.8×10^3)	-3.0025×10^5	3.4571
0.50	-1.9879×10^5 (2.30×10^3)	-1.9628×10^5	1.2787
0.70	-1.2433×10^5 (8.90×10^2)	-1.2697×10^5	2.0792
		ADD	2.27

[a]N = 100, T= 300K, p =200 bar

Table 6.15: Comparison for Unconfined Mixtures of Water/Hexane[a]

x_{H2O}	$\langle U_M^D(T,P)\rangle$	$\sum_{i=1}^{c} x_i\langle U_i^D(T,P)\rangle$	% Error
0.25	-3.3114×10^5 (4.54×10^3)	-3.2537×10^5	1.7740
0.50	-3.9171×10^5 (1.01×10^4)	-3.7392×10^5	4.7573
0.75	-4.3132×10^5 (9.27×10^3)	-4.2248×10^5	2.0926
		ADD	2.87

[a]N = 100, T= 290K, p =60 bar

Table 6.16: Comparison for Unconfined Mixtures of Methane/Propane[a]

x_{CH4}	$\langle U_M^D(T,P)\rangle$	$\sum_{i=1}^{c} x_i\langle U_i^D(T,P)\rangle$	% Error
0.25	-9.4983×10^4 (1.77×10^3)	-1.0067×10^5	5.6478
0.50	-7.2099×10^4 (2.78×10^3)	-7.0981×10^4	1.5758
0.75	-4.0500×10^4 (1.27×10^3)	-4.1294×10^4	1.9220
		ADD	3.05

[a]N = 100, T= 300K, p =100 bar

Table 6.17: Comparison for Unconfined Mixtures of CO_2/Hexane[a]

x_{CO2}	$\langle U_M^D(T,P)\rangle$	$\sum_{i=1}^{c} x_i\langle U_i^D(T,V)\rangle$	% Error
0.25	-2.3198×10^5 (2.21×10^3)	-2.2338×10^5	3.8479
0.50	-1.8587×10^5 (2.16×10^3)	-1.7661×10^5	5.2444
0.75	-1.3350×10^5 (3.98×10^3)	-1.2984×10^5	2.8184
		ADD	3.97

[a]N = 100, T= 300K, p =80 bar

Table 6.18: Comparison for Unconfined Mixtures of CO_2/Propane[a]

x_{CO2}	$\langle U_M^D(T,P)\rangle$	$\sum_{i=1}^{c} x_i\langle U_i^D(T,V)\rangle$	% Error
0.25	-1.2762×105 (1.35×102)	-1.2160×105	4.9508
0.50	-1.1629×105 (1.36×103)	-1.0875×105	6.9325
0.75	-9.6263×104 (5.16×102)	-9.5908×104	0.3706
		ADD	4.08

[a]N = 100, T= 300K, p =80 bar

6.2 Langmuir Parameters for Various Hydrocarbons

Table 6.19: Methane Langmuir Parameters

T (K)	Pore Size	K (10^3)	M	RMSE
300	14.2	3.188	15.102	0.0798
450	14.2	1.831	15.805	0.0483
550	14.2	1.387	16.220	0.0303
300	17.04	1.609	28.782	0.0389
450	17.04	1.134	27.010	0.0363
550	17.04	1.035	24.533	0.0440
300	19.88	2.083	25.983	0.00994
450	19.88	1.126	31.524	0.004693
550	19.88	0.894	32.225	0.0166

*RMSE: Root-mean-square deviation

Table 6.20: Ethane Langmuir Parameters

T (K)	Pore Size	K (10^3)	M	RMSE
300	14.2	10.883	9.063	0.409
450	14.2	4.513	9.545	0.151
550	14.2	2.581	10.845	0.0270
300	17.04	2.881	18.623	0.144
450	17.04	2.025	17.142	0.0502
550	17.04	1.593	16.995	0.0752
300	19.88	2.628	20.622	0.113
450	19.88	1.846	20.478	0.0568
550	19.88	1.424	21.390	0.0724

*RMSE: Root-mean-square deviation

Table 6.21: Propane Langmuir Parameters

T (K)	Pore Size	K (10^3)	M	RMSE
300	14.2	26.954	7.145	1.183
350	14.2	15.576	7.330	0.650
450	14.2	6.593	7.955	0.297
550	14.2	4.34	7.808	0.183
300	17.04	5.068	12.237	0.147
350	17.04	4.317	11.956	0.0625
450	17.04	3.442	11.222	0.0193
550	17.04	2.863	10.989	0.0718
300	19.88	3.831	15.825	0.152
350	19.88	3.192	16.126	0.107
450	19.88	2.637	15.580	0.0666
550	19.88	2.217	14.856	0.0603

*RMSE: Root-mean-square deviation

Table 6.22: Butane Langmuir Parameters

T (K)	Pore Size	K (10^3)	M	RMSE
300	14.2	17.494	6.071	0.109
450	14.2	15.374	5.484	0.113
550	14.2	6.816	6.079	0.188
300	17.04	8.888	8.930	0.184
450	17.04	6.086	8.185	0.0469
550	17.04	5.117	7.688	0.0377
300	19.88	4.809	12.877	0.196
450	19.88	3.637	11.829	0.0731
550	19.88	2.986	11.600	0.0771

*RMSE: Root-mean-square deviation

Table 6.23: Octane Langmuir Parameters

T (K)	Pore Size	K (10^3)	M	RMSE
300	14.2	110.452	3.078	0.0436
450	14.2	28.054	3.191	0.0324
550	14.2	31.197	3.085	0.0145
300	17.04	15.868	5.154	0.266
450	17.04	11.932	4.618	0.0949
550	17.04	9.856	4.472	0.0887
300	19.88	5.341	7.331	0.121
450	19.88	8.252	5.984	0.0496
550	19.88	8.454	5.592	0.0268

*RMSE: Root-mean-square deviation

Table 6.24: Hexadecane Langmuir Parameters

T (K)	Pore Size	K (10^3)	M	RMSE
300	14.2	110.452	1.358	0.0871
450	14.2	28.054	1.356	0.0579
550	14.2	31.197	1.294	0.0540
300	17.04	15.868	1.774	0.0640
450	17.04	11.932	1.731	0.0517
550	17.04	9.856	1.469	0.142
300	19.88	5.341	3.941	0.155
450	19.88	8.252	2.480	0.0491
550	19.88	8.454	2.397	0.0936

*RMSE: Root-mean-square deviation